INVESTIGATIONS ON IRON REMOVAL PROCESS BY OXYGEN LEACHING IN A MECHANICALLY AGITATED CONTACTOR

THESIS
SUBMITTED TO THE UNIVERSITY OF KERALA
IN PARTIAL FULFILMENT OF THE REQUIREMENTS
FOR THE DEGREE OF
DOCTOR OF PHILOSOPHY
IN CHEMICAL ENGINEERING

BY

K. S. GEETHA

REGIONAL RESEARCH LABORATORY
(Council of Scientific and Industrial Research)
THIRUVANANTHAPURAM-695 019
INDIA

MAY 1997

INVESTIGATIONS ON IRON REMOVAL PROCESS BY OXYGEN LEACHING IN A MECHANICALLY AGITATED CONTACTOR

THESIS
SUBMITTED TO THE UNIVERSITY OF KERALA
IN PARTIAL FULFILMENT OF THE REQUIREMENTS
FOR THE DEGREE OF
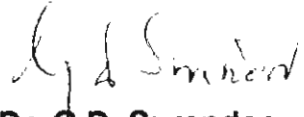## DOCTOR OF PHILOSOPHY
IN CHEMICAL ENGINEERING

BY

K. S. GEETHA

Dr. G.D. SURENDER
Head, Mineral Process Engineering Division

CERTIFICATE

Certified that the work embodied in this thesis entitled "**Investigations on Iron Removal Process by Oxygen Leaching in a Mechanically Agitated Contactor**" has been carried out by **Mrs. K.S. Geetha** under my supervision in partial fulfilment of the requirements for the degree of **Doctor of Philosophy in Chemical Engineering** of the University of Kerala and the same has not been submitted elsewhere for a degree.

Dr. G.D. Surender
Supervising Guide

DECLARATION

I hereby declare that the matter embodied in this thesis is the result of the investigations carried out by me in the Process Engineering Department of Regional Research Laboratory, Trivandrum, under the guidance of Dr. G.D. Surender and the same has not been submitted elsewhere for a degree or diploma.

(Geetha K.S.)

ACKNOWLEDGEMENT

Trivandrum

May 1997

GEETHA K.S.

CONTENTS

ABSTRACT

Hydrometallurgical routes to eliminate the iron constituent from the mineral ilmenite ($FeTiO_3$) is a crucial step in the manufacture of high value inorganic chemicals such as Titanium dioxide. In contrast to the acid mediated leaching processes, the Becher process has found world wide acceptance due to its environmental advantages since a disposable form of iron oxide and a liquid effluent at near neutral pH are generated. In the Becher process, the metallic iron component in reduced ilmenite is converted to iron oxide by means of an electrochemical reaction with dissolved oxygen followed by oxidation of ferrous to ferric iron, hydrolysis and precipitation. Reduced ilmenite (average particle size 200 mm) and precipitated iron oxide particles (average particle size 1.06 mm) suspended in the aqueous electrolyte constitute a unique multi-solid slurry system, whose influence on mass transport of oxygen has not been studied so far. Mechanically agitated, air sparged reactors are normally employed to satisfy the simultaneous requirement of solids suspension and gas dispersion.

Notwithstanding its environmental advantages, the Becher process is extremely sluggish and needs significant improvements in its productivity to compete with other processes. The absence of an adequate engineering model has prevented the identification of controlling steps and a systematic effort towards process intensification. This thesis aims to accomplish this objective through the development of an experimentally validated process model based on the rate

determining steps, derived from an analysis of the kinetics of sub-processes, namely, mass transfer between coarse active particles (reduced ilmenite) and dissolved oxygen, oxygen mass transfer between gas bubbles and aqueous electrolyte and the homogeneous oxidation of ferrous to ferric iron in the aqueous phase. In view of the unique complexity of the process, each of the rate determining steps were experimentally investigated and interpreted with a view to obtain quantitative expressions which then served as inputs to the overall process model. In order to simulate the process as closely as possible to industrial conditions, the particle sizes, solid loading and the reactor configuration have been chosen accordingly. The effect of high solid loading on mass transfer rates, which has not been adequately studied in the literature, also forms an important subject for study. The objective of process intensification has been accomplished through the addition of ferrous chloride to the reacting solution, which leads to an enhancement of gas-liquid mass transfer rate by shifting the ferrous oxidation reaction from a slow reaction regime to fast reaction regime.

Chapter I gives a brief introduction to the subject of investigation, its relevance and scope in the light of the recent trends in the removal and control of iron in mineral to material conversion processes. A critical review of state of art both with respect to the Becher process as well as the rate determining sub-processes serves to identify the knowledge gaps in the literature. Chapter II also gives an up-to-date trend in the modelling of iron removal processes with respect to other mineral leaching systems.

Chapter III describes the experimental investigations on attenuation of solid-liquid mass transfer due to inert micro-particles and its semi-theoretical interpretation in terms of mass transfer fouling. A range of micro-particles with sizes ranging from 0.3 to 13 mm and density from 2600 to 5400 kg/m^3 were investigated. Characterisation of the colloidal and rheological properties of the micro-particle systems were carried out to aid in the interpretation of the mass transfer attenuation phenomena as being controlled essentially by the hydrodynamics of the system. Chapter IV describes the experimental investigations and quantitative interpretation of gas-liquid mass transfer attenuation due to inert micro-particles.

Chapter V and VI describe the development and experimental validation of the models to describe the conversion versus time behaviour of the metallic iron removal process for non-porous (iron particles) and porous (reduced ilmenite) particles respectively. Besides predicting the isothermal and non-isothermal behaviour, the models are able to describe the trends in the variation of pH and oxidation reduction potential during the course of the reaction. Furthermore, the model is also able to predict the conditions under which incipient passivation of iron could occur at higher oxygen partial pressures (greater than 2.03×10^4 Pa). The significant reduction in iron removal rates beyond a conversion of 0.4 has been explained as being due to hindered diffusion of oxygen in pores filled with micro-particles.

Experimental investigation and interpretation of process intensification by enhancement of gas-liquid mass transfer rates is described in Chapter VII. The enhancement factors have been computed based on the oxidation kinetics of ferrous iron determined in Chapter V, and are found to closely agree with the experimentally observed values, the maximum enhancement factor being 1.7. Thus a sound theoretical basis and a validated engineering model has been established for improving the productivity of the Becher process over a wide range of process parameters with relevance to industrial application.

LIST OF TABLES

(viii)

LIST OF FIGURES

(x i i)

NOMENCLATURE

a_S - Specific surface area of active particles, m^{-1}

a_{Si} - Active specific surface area at any time, m^{-1}

C_{Ai} - Equilibrium concentration of solute A in the liquid, $kmol/m^3$

C_b - Concentration of oxygen in the bulk phase, $kmol/m^3$

C_{Bo} - Concentration of reactant B in the bulk liquid, $kmol/m^3$

$C_{b,p}$ - Particulate concentration in the bulk liquid, $kmol/m^3$

C_D - Drag coefficient

$C_{Fe^{2+}}$ - Concentration of Fe^{2+} ions in the bulk liquid, $kmol/m^3$

C_{Fe} - Concentration of metallic ion in the slurry, $kmol/m^3$

$C_{Fe_2O_3}$ - Concentration of iron oxide in the slurry, $kmol/m^3$

C_g - concentration of oxygen in the gas phase, $kmol/m^3$

C_{H^+} - Concentration of H^+ ions in the bulk liquid, $kmol/m^3$

C_i - Concentration of oxygen at the gas-liquid interface, $kmol/m^3$

C_{in} - Concentration of solute in the inlet stream, $kmol/m^3$

C_o - Initial concentration of solute in the bulk solution, $kmol/m^3$

C_{OH^-} - Concentration of OH^- ions in the bulk liquid phase, $kmol/m^3$

$(C_p)_{il}$ - Specific heat of ilmenite, $kcal/kg.°K$

$(C_p)_w$ - Specific heat of water, $kcal/kg °K$

C_s - Concentration of oxygen at the surface of solid, $kmol/m^3$

$C_{S,P}$ - Surface concentration of micro-particles, $kmol/m^3$

C_{st} - Steady state concentration of solute in the reactor, $kmol/m^3$

C_f - Final concentration of solute in the bulk solution, $kmol/m^3$

D_a	-	Diameter of the agitator, m
D_B	-	Diffusivity of solute B in the liquid
D_{es}	-	Effective diffusivity of oxygen in the pores, m^2/S
d_h	-	diameter of gas bubble, m
d_{mp}	-	Diameter of micro-particle, μm
d_p	-	diameter of active particle, μm
E	-	Enhancement factor
E_i	-	Enhancement factor for instantaneous reaction
F_s	-	Drag force, N/m^2
g	-	acceleration due to gravity, m/S^2
Ha	-	Hatta number given by Eq.7.1.
λ_{H2O}	-	Rate of formation of H_2O from H^+ and OH^- ions, $kmol/m^3.S$.
H	-	Henry's law constant
Hp	-	Enthalpy, kcal/kg
k	-	Rate constant for homogeneous phase reaction, $(kmol/m^3)^{-1}S^{-1}$
$k_{gl}a_g$		Volumetric gas-liquid mass transfer coefficient, S^{-1}
$(k_{gl}a_g)_s$	-	Volumetric gas-liquid mass transfer coefficient in the presence of inert solids, S^{-1}
k_{sl}	-	solid-liquid mass transfer coefficient, m/S
P_{O_2}	-	Partial pressure of oxygen, Pa
N_c	-	Critical agitator speed for solid suspension, S^{-1}
q_g	-	gas flow rate, m^3/S
R	-	Radius of reduced ilmenite particle, m

(xv)

R_{eb} - Bubble Reynold's number $(v_b d_b \varrho)/\mu$

R_{Fe} - Rate of dissolution of iron, kmol/m³S

$R_{Fe^{2+}}$ - Rate of reaction of Fe^{2+} ions through the homogeneous phase reaction, kmol/m³ S

R_i - Radius of the shrinking core, m

$\dot{R}_{gl}$ - Rate of gas-liquid mass transfer, kmol/m³.S

R_{O_2} - Total rate of consumption of oxygen by electrochemical and ferrous oxidation reaction, kmol/m³S

$\dot{R}_{O_{2,h}}$ - Rate of reaction of oxygen through the homogeneous phase reaction, kmol/m³ S

$R_{O_{2,s}}$ - Rate of consumption of oxygen by the electrochemical reaction, kmol/m³ S

Sh   - Sherwood number, $\dfrac{k_{sl}d_p}{D}$

Sk   - Stokes number

T   - Temperature, K

t   - Time, S

V   - Volume of liquid in the reactor, m³

v_b - Velocity of gas bubble, m/S

v_d - rms of velocity, m/S

v_e - Eddy fluctuation velocity, m/S

V_{sl} - Volume of slurry in the reactor, m³

W   - 100 x weight of solid/weight of slurry

x   - Conversion

z   - Number of moles B reacting with one mole of A

(x v i)

Greek letters

α - Relative mass transfer factor (ratio of solid-liquid mass transfer coefficients in the absence and presence of inert micro-particles

β - mass transfer attenuation factor

$\Delta\rho$ - $\rho p - \rho$, kg/m^3

ΔH - Heat of reaction for the formation of Fe_2O_3 from Fe, kcal/kmol

ε - Power dissipation, W/m^3

ϕ - Volume fraction of solids

ϕ^* - Threshold volume fraction

ϕ_{mp} - Volume fraction of micro-particles

μ - Viscosity of liquid, kg/m S

μ_{sl} - Viscosity of liquid, m^3/S

ν - Kinematic viscosity of liquid, m^3/S

ν_{sl} - Kinematic viscosity of slurry, m^3/S

ρ - Density of liquid, kg/m^3

ρ_{mp} - Density of micro-particle

ρ_p - Density of particle, kg/m^3

ρ_{sl} - Density of slurry, kg/m^3

Abbreviations

R.I.   Reduced Ilmenite

CHAPTER 1

INTRODUCTION

An efficient and environmentally acceptable iron removal step is still a distant goal in mineral conversion processes due to the widespread occurrence of iron as an impurity in almost all minerals. A number of alternative approaches have been suggested ranging from conversion to iron oxides or its derivative by hydrometallurgical routes or to the manufacture of metallic (pig) iron through pyrometallurgical smelting. The importance of iron control over the years has assumed tremendous recognition due to the stricter environmental regulations as well as the need to realise the economic potential in iron fraction which in some cases may account for as much as 30% of the weight of mineral. The two international conferences held in 1986 and 1996 on iron control in mineral processing serve to highlight its current importance and highlight the state of art (Dutrizac and Monhemius, 1986). In brief, the current approach to iron control in mineral processing aims at efficient separation of the iron component as value-added products so as to overcome solid disposal problems.

Iron removal and control constitutes a crucial step in the upgradation of ilmenite ore to high value products such as synthetic rutile and titanium dioxide. Its relevance to Indian economy could be judged by the fact that 15% of the world's premier high grade ilmenite resources of approximately 700 million tonnes occur in

1

the beach sands on the coast line stretching from Maharashtra to Kerala in the West Coast and from Tamil Nadu to Orissa in the East Coast. The ilmenite ore (40-60% TiO_2) is upgraded in two stages, namely, conversion to synthetic rutile (92-95% TiO_2) followed by conversion to titanium dioxide (>99% TiO_2). Thus, the major proportion of iron removal (as much as 90%) is accomplished during the ilmenite to synthetic rutile conversion stage.

The iron removal strategy is the distinguishing feature among competing processes for the manufacture of synthetic rutile. Benilite, Murso, Isihara, Becher and Summit processes are the five different processes developed for the manufacture of synthetic rutile. All these processes involve firstly, partial or complete reduction of the iron oxidation state in the ilmenite crystal lattice by roasting with coal, followed by selective leaching of the iron with HCl, H_2SO_4, $FeCl_3$ or aerated NH_4Cl solution. However, over the years, only the Benilite and Becher processes employing the hydrometallurgical route have proved to be commercially successful. A comparison of the iron removal strategies followed in two processes is given Fig.1. The Becher process has found world wide acceptance due to its environmental advantages as well as the reduced capital and operating costs since the conversion of metallic iron to iron oxides is carried out in a single step at near ambient conditions.

Notwithstanding its advantages the iron removal step in the Becher process is extremely sluggish (industrial batch reaction time of 14 hrs) and needs significant

2

Ilmenite
(typical composition: FeTiO$_3$ 60%
TiO$_2$ 35%, Fe$_2$O$_3$, FeO 5% inerts)

Benilite   Becher

Partial reduction with coal   Metallisation by reduction with coal
at 1073 - 1173°K   at 1273 - 1373°K
(Fe$_2$O$_3$ + C $\rightarrow$ 2FeO + CO)   (FeTiO$_3$ + C $\rightarrow$ Fe(M) + TiO$_2$ + CO)

Acid leaching with 30% HCl   Ammoniacal oxygen leaching in
at 403 K and 3 atm   ambient conditions
FeO + 2HCl $\rightarrow$ FeCl$_2$ + H$_2$O   4Fe + 3O$_2$ + 2x.H$_2$O $\rightarrow$ 2Fe$_2$O$_3$.xH$_2$O

Pyrolytic acid regeneration at 1273 K   Separated iron oxides
4FeCl$_2$ + 4H$_2$O + O$_2$ $\rightarrow$ 2Fe$_2$O$_3$ + 8HCl   pH around 6.0

Separated iron oxides
chloride contaminated Fe$_2$O$_3$
pH around 1.0

Fig.1. Schematic description of two competing techniques for
iron removal from ilmenite

mprovements in its productivity. The absence of an adequate engineering model has

>resented the identification of rate controlling steps and a systematic effort towards

>rocess intensification. This thesis aims to accomplish this objective through a

:ombination of experimental investigations and development of a process model,

'ollowed by its experimental validations.

STATE OF ART

Since the development of the Becher's process in Australia during 1965, several investigations (Becher *et al.*, 1965) have been reported on the process chemistry aspects aimed at understanding the role of electrochemistry of metallic iron dissolution, the role of NH_4Cl in preventing 'in situ rusting' and the mechanistic pathway for the preparation of various types of iron oxides. However, there has not been any attempt in the literature aimed at the development of a quantitative process model to identify the rate determining steps and to form a basis for design of reactors. This chapter, therefore, present a review of the process chemistry aspects followed by the state of art in the mechanistic description of the various sub-processes constituting the Becher process. The objective of this chapter is to identify the gaps in the knowledge-base which need to be fulfilled prior to the development of a quantitative process model of the Becher's process and its validation.

2.1. Description of the Becher Process

In this process, the iron(II) and Iron(III) content of the ilmenite is first reduced to metallic iron in a rotary kiln at about 1150°C using a suitable coal as both reductant and fuel in a rotary kiln. The overall reaction is:

$$FeO.TiO_2 \ (S) + C(S) \ \rightarrow \ Fe \ (S) + TiO_2 \ (S) + CO \ (g) \qquad (2.1)$$
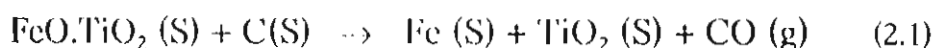
The material resulting from this step, known as **reduced ilmenite**, consists of a matrix of rutile covered on the surface with metallic iron. In the second step, the metallic iron is removed from the reduced ilmenite by an accelerated corrosion reaction using oxygen dissolved in ammonium chloride solution. The product is termed as synthetic rutile, which is used as a feedstock in the chloride route for the production of TiO_2 pigment. This process is now operated commercially in Western Australia.

The second step of the Becher process, namely, the ammoniacal oxygen leaching process, forms the subject for the present study. When this process is carried out industrially on a batch mode, air is forced through a pulp consisting of 50% by weight reduced ilmenite in 0.1 M NH_4Cl in a stirred slurry reactor. Heat released in the exothermic corrosion reaction results in the temperature of the system rising to about 65-75°C. The oxidation of the iron metal in the reduced ilmenite is usually completed in 14-16 hours (Bracanin *et al.* 1980). A variety of hydrated iron(III) oxides are formed as a by-product of the reaction and are removed by means of cyclones. The overall leaching reaction can be expressed as

$$4Fe + 3O_2 \text{ (aq)} + x.H_2O \rightarrow 2Fe_2O_3.xH_2O \qquad (2.2)$$
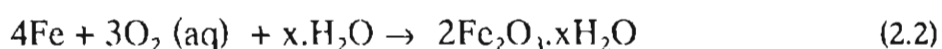
2.2. Reported Investigations on the Oxygen Leaching Process

Process Chemistry

The mechanism of iron leaching in Becher process is essentially the electrochemical corrosion of iron by dissolved oxygen (Becher *et al.*, 1965; Farrow

6

et al., 1987) followed by oxidation of the ferrous iron species to ferric iron and its subsequent hydrolysis and precipitation as hydrous iron oxides.

Anodic reaction

$$Fe^{\circ} \rightarrow Fe^{2+} + 2e^{-} \qquad (2.3)$$

Depending on the solution pH, the anodic reaction can proceed through any of the following two mechanisms:

$$O_2 + 4H^+ + 4e^- \rightarrow 2H_2O \qquad (2.4)$$

$$O_2 + 2H_2O + 4e^- \rightarrow 4OH^- \qquad (2.5)$$
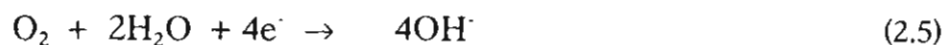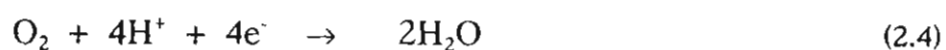
Investigations on the kinetics of electrochemical dissolution of metallic iron from reduced ilmenite in oxygenated 0.1 M NH_4Cl solution were carried out by Farrow *et al.* (1987) by polarisation and mixed potential measurements. Electrodes of both pure iron and reduced imenite-mujol oil paste were employed. Information about the reaction mechanism was obtained by constructing Evans diagram in which the polarisation curves for the two half-reactions (the oxidation of iron and the reduction of oxygen) were plotted on the same current-potential plot. It was noted that the oxygen reduction curve reached a limiting current which was rotation speed dependent, and that the two polarisation curves attained the same current magnitude in the region in which the oxygen reduction current was near the limiting current. From this, the authors concluded that the electrochemical dissolution of iron was controlled by oxygen diffusion to the iron surface. This fact was further confirmed by measuring the potential of an iron disc electrode reacting

7

with oxygen in 0.1 M NH_4Cl as a function of the disc rotation speed, in which it was noted that the mixed or corrosion potential increases with increasing rotation *speed.*

The role of NH_4Cl: Prevention of 'in situ' rusting

The role of NH_4Cl was identified by Farrow *et al.* (1987) as a buffering and complexing agent, thus helping in prevention of 'in situ rusting'. The buffering and complexing action of NH_4Cl was explained as follows:

The hydroxyl ions responsible for high surface pH values originate during the cathodic reduction of oxygen according to Eq.(2.5). Unless these hydroxyl ions are removed from the surface by some mechanism, they will react with the Fe^{2+} ions produced during the anodic half reaction given by Eq.2.1 to produce a precipitate of ferrous hydroxide in the pores or near the surface of the reduced ilmenite. This solid material is readily oxidised further. The ammonium ion is thought to prevent high surface pH values and the subsequent precipitation of oxide by the reaction

$$NH_4^+ \text{ (aq)} + OH^- \text{ (aq)} \rightarrow NH_3 \text{ (aq)} + H_2O \qquad (2.6)$$
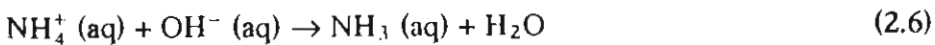
Complex ions of the type $[Fe(NH_3)_x (H_2O)_{6-x}]^{2+}$ may be then formed by reaction with the free ammonia

$$Fe(H_2O)_6]^{2+} + xNH_3 \rightarrow \left[Fe(NH_3)_x (H_2O)_{6-x} \right]^{2+} xH_2O \qquad (2.7)$$

8
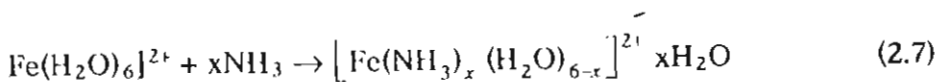
which would stabilize the Fe^{2+} iron and allow it to move away from the metal surface without being precipitated. Precipitation would subsequently take place in the bulk solution where the pH is much lower causing reactions 2.6 and 2.7 to be reversed. Ammonia would be converted back to ammonium ion and then Fe^{2+} - ammonia complex would break up, liberating Fe^{2+} ions.

Influence of process conditions on the transformations of iron oxide

Farrow *et al.* (1987) during their investigations noted that the air saturated 0.1 M NH_4Cl solution at 70°C had an initial pH of about 5.4 which rose rapidly to about 7.5 upon addition of the reduced ilmenite sample. As the reaction proceeded, the pH of the solution decreased from about 7.5 to 4.5 in the first hour, and then moved sowly to a final pH of about 3.6. However, when NaCl was used as the electrolyte, the pH remained in the alkaline range itself. The by-product iron oxides were identified as a mixture of hematite (α - Fe_2O_3) and lepidocrocite (γ - FeOOH) from NH_4Cl leaching and a mixture of magnetite (Fe_3O_4) and goethite (α - FeOOH) from NaCl leaching. Hence they concluded that the pH of the bulk solution is controlled by the type of oxide formed during the aeration reaction.

Ward *et al.* (1989) conducted a programme of tests on site at the Westralion sands Ltd.Synthetic Rutile plant at Capel to monitor the pH, Eh, Fe^{2+} concentration, temperature and percent iron reacted at hourly intervals over the duration of a typical plant aeration operation. The results are reproduced in Fig.2.1. To account for the pH changes observed, the competition between the following

9
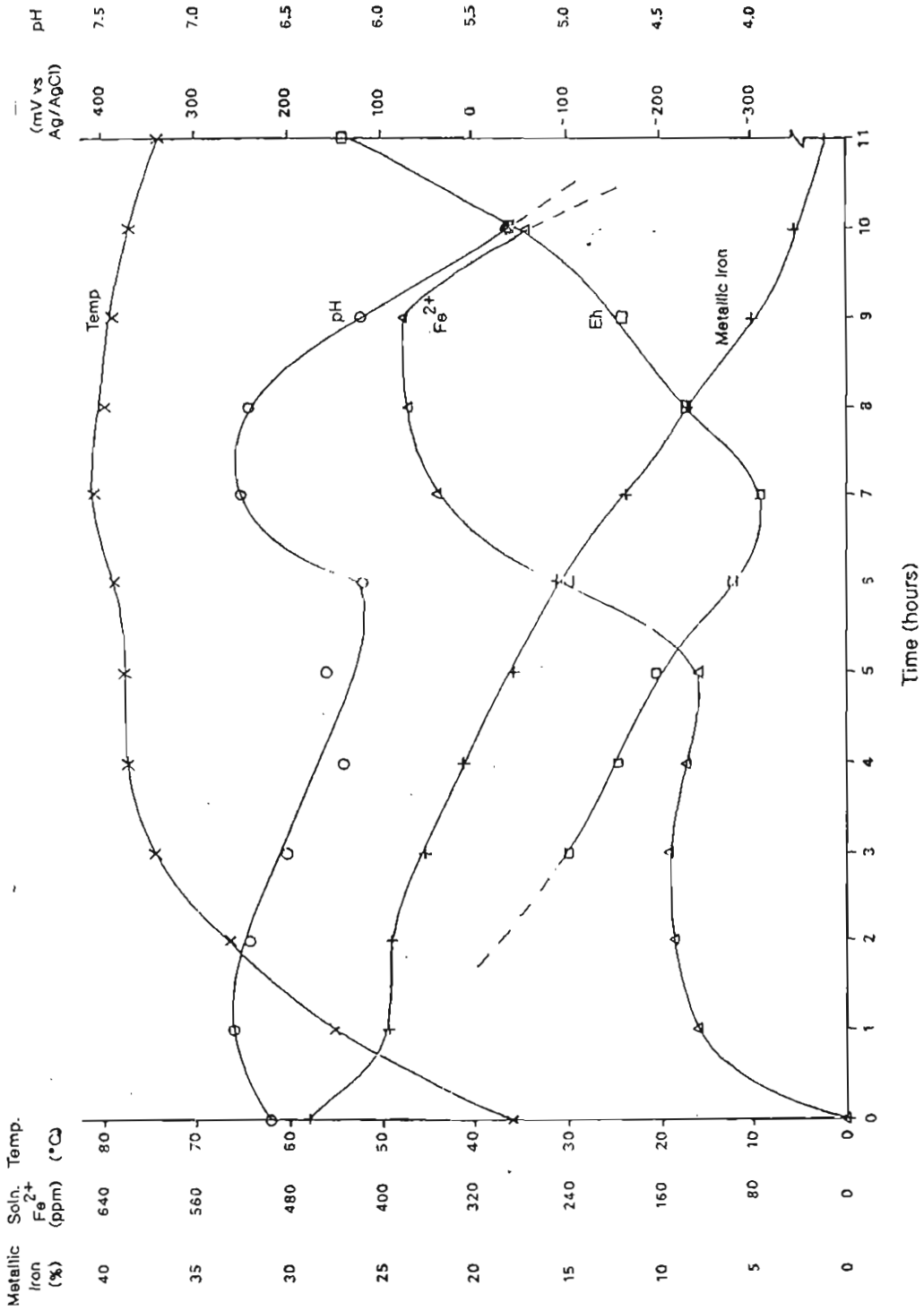
Fig. 2.1. Profile of solution conditions during a typical plant scale batch operation of reduced ilmenite

acid consuming corrosion reaction and acid generating reaction of hydrolysis of the solubilised iron was proposed.

$$Fe + O_2 + 4H^+ \rightarrow 2Fe^{2+} + 2H_2O \tag{2.8a}$$

$$Fe^{2+} + \tfrac{1}{2}O_2 + 3H_2O \rightarrow 2FeOOH + 4H^+ \tag{2.8b}$$
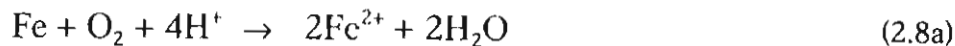
The observed variations in Eh and Fe^{2+} ion concentrations during the process as shown in Fig.2.1 were also explained by Ward *et al.* (1989) as the result of competition between the above two reactions.

Table 2.1 Reported Literature conditions for the production of synthetic iron oxides (Reproduced from Ward *et al.*, 1989)

Phase	Colour	Formula	Anion	Temp. °C	pH
Hydrated oxides	green	variable	any	25-100	< 7
Magnetite	black	Fe_3O_4	SO_4^{2-}	95-100	< 7
Hematite	red	$\alpha\text{-}Fe_2O_3$	SO_4^{2-}	50-100	3-4.5
Maghemite	brown	$\alpha\text{-}Fe_2O_3$	SO_4^{2-}, Cr	95-100	> 7
Geothite	yellow	$\alpha\text{-FeOOH}$	SO_4^{2-}, Cr	80	2-3.5
Akageneite	brown	$\beta\text{-FeOOH}$	Cr	80	2-3.5
Lepidocrocite	gold	$\alpha\text{-FeOOH}$	SO_4^{2-}, Cr	70	6-7

The rise in temperature is due to the exothermic nature of the rusting reaction.

Ward *et al.* (1989) found that the iron oxide products from the particular plant run varied with time, and confirmed that lepidocrosite initially precipitated and later transformed to hematite and magnetite. Table 2.1 summarises the conditions reported in the literature for the formation of pure iron oxides. From
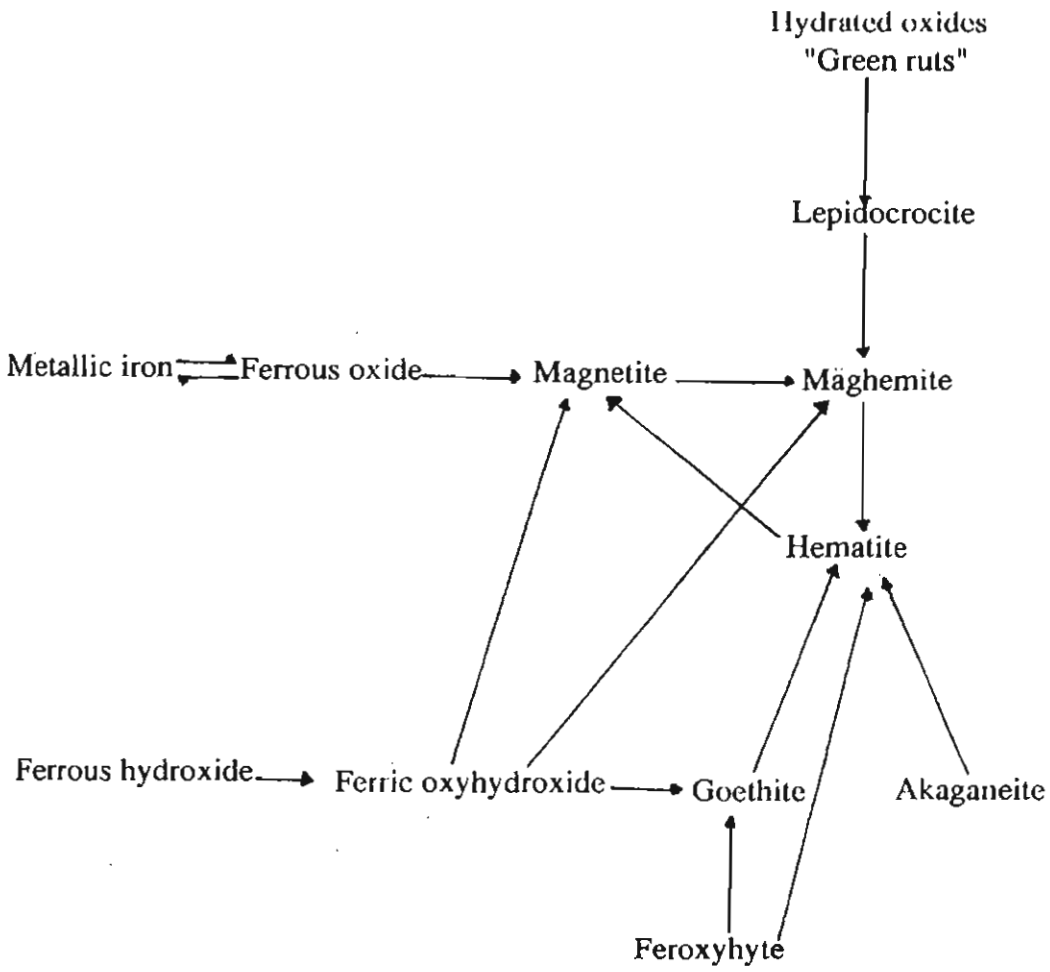
Fig.2.2. The system of iron oxide transformation
(Reproduced from Ward *et al.*, 1989)

this table it is clear that 'greenrusts' or hydrated oxides and lepidocrosite are formed at lower temperatures in near neutral pH conditions. It is reported that these unstable oxides are transformed into different stable oxides depending on the solution condition of pH, temperature and Fe^{2+} concentration. Fig.2.2 shows the pathways of a number of transformation to the more stable oxides. From these information on iron oxide transformation and studies on variation of solution properties during the 'rusting' process (Ward et al. 1989) confirmed that lepidocrosite is initially formed at cooler temperatures and is transformed to more stable iron oxides depending on pH, Eh, Fe^{2+} concentration and temperature of the solution to give a range of coloured products.

Oxygen leaching of reduced ilmenite at elevated temperatures and pressures

Recently Jayasekera et al. (1994) carried out studies on pressure leaching of reduced ilmenite in NH_4Cl solution at various temperatures. Initially, they studied the electrochemical aspects of iron dissolution by oxygen reduction in NH_4Cl solution using rotating disc electrode technique over the temperature range 30-150°C and at a total pressure upto 780 kPa. Corrosion current densities were determined by the Evan's diagram and linear polarization method and showed that the corrosion rate increases with increasing temperatures and oxygen partial pressures. It was shown that at higher partial pressures of oxygen (3×10^5 Pa) the corrosion rate increases about four or five times as the temperature rises from 30 to 150°C. This is explained by the authors as being due to the increased diffusivity of oxygen at higher temperature. However, in the air and oxygenated solutions, the

corrosion rate remained relatively unchanged between 30 and 80°C indicating that the increased oxygen *diffusivity balances the decrease in oxygen solubility.*

Jayasekhera *et al.* (1995) also carried out investigations on leachig of reduced ilmenite in agitated vessels over a range of oxygen partial pressures at temperatures of 75 and 150°C. The results were in agreement with electrochemical studies showing increase in iron removal rate with temperature and oxygen partial pressure. Leaching of reduced ilmenite with air at 75°C took about 7 hours to reduce the residual Fe(metal) content to a value around 1.7%, whereas the same result was achieved within one hour when pure oxygen was used at a temperature of 130°C. By contrast, the total residual iron levels were substantially (about two times) higher than that results from conventiaonl leaching conditions, representing a significant problem of increased 'in situ rusting'.

2.3. Mechanistic and kinetic aspects of sub-processes

Based on the process chemistry and from the gas-liquid-solid reactor engineering aspects (Shaw, 1979; Fogler, 1986), the following rate steps or sub-processes are identified to constitute the overall oxygen leaching step of the Becher process carried out in a mechanically agitated reactor:

1. Oxygen mass transfer from the gas phase to the bulk liquid phase (gas-liquid mass transfer).

2. oxygen mass transfer from the bulk liquid phase to the solid-surface (solid-liquid mass transfer).

14

3. Diffusion of oxygen through the pores to the reacting surface (porous diffusion)

4. Electrochemical corrosion of iron by dissolved oxygen (surface reaction).

5. Oxidation of Fe^{2+} to Fe^{3+} in the bulk liquid phase.

6. Hydrolysis of Fe^{3+} (aq) and subsequent precipitation.

A schematic representation of the oxygen leaching process depicting all the constituent steps are illustrated in Fig.2.3. It is important to note that the sub-processes outlined above take place in slurries containing high solid contents (typically 20-30% by weight) comprising of both macro (150-300 μm) and micro (< 10 μm) particles.

The rate of the overall process is determined by the rate of the slowest step, which is known as the controlling step. If series-parallel steps are also involved, there can be more than one controlling step. For the development of a process model, the kinetics of all sub-processes are to be known and the controlling steps are to be identified. Hence, in the following sections, state of art on the various sub-processes with emphasis on the kinetics of individual steps appropriate to the conditions typical of the Becher process listed are reviewed.
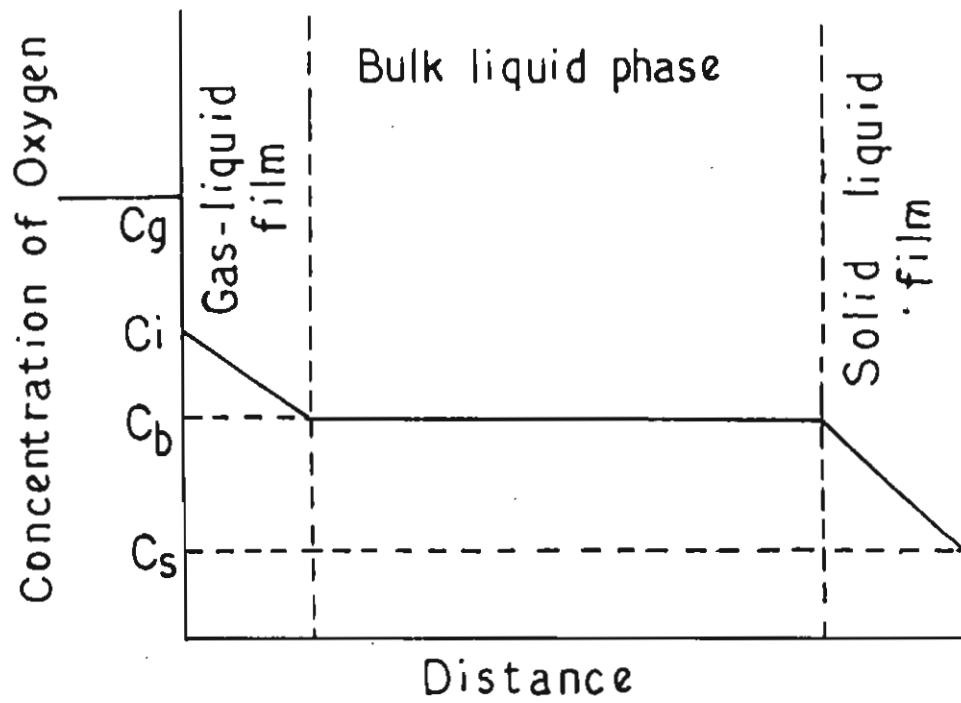
Fig.2.3. Schematic representation of oxygen leaching step in Becher process

Gas-liquid mass transfer in the presence of suspended inert particles

Excellent review articles (Beenackers and Van Swaaij, 1993) highlight the current understanding of the subject available. The typical correlations for predicting volumetric gas-liquid mass transfer coefficients based on energy dissipation rate is listed in Table 2.2. However, direct relevance to the present work are of those investigations dealing with:

a) influence of high solid loading on volumetric gas-liquid mass transfer coefficient

b) influence of temperature, concentration of ions in the liquid and pH on the volumetric gas-liquid mass transfer coefficient. The state of art in the above are critically reviewed below.

Investigations on the influence of suspended inert particles on gas-liquid mass transfer in mechanically agitated reactions (Joosten et al. 1977; Oguz et al. 1987; Kojima et al., 1987; Lee et al., 1982) reveals that both microparticles (dp < 10 μm) and macroparticles (dp > 10 μm) induce gas-liquid mass transfer attenuation. Oguz et al. (1987) studied the influence of various inert microparticles and correlated the reduced volumetric gas-liquid mass transfer coefficient in terms of slurry viscosity (Table 2.2). From the investigations employing inert macroparticles (150 μm to 4 mm), Kojima et al. obtained the following relationship:

$$\frac{(k_{gl}a_g)_s}{k_{gl}a_g} = 1 - \phi_s \qquad (2.9a)$$

where $(k_{gl}a_g)_s$ is the reduced volumetric gas-liquid mass transfer coefficient in the presence of solids and ϕ_s is the volume fraction of solids. Then the gas-liquid mass transfer rate can be computed from the relationship.

$$R_{gl} = (k_{gl}a_g)_S (C_i - C_b) \tag{2.9b}$$

Table 2.2. Gas-liquid mass transfer correlations in terms of energy dissipation rate

Reference	System	Correlation
Linek et al. (1987)	Clear water	$k_{gl}a_g = 4.95 \times 10^{-3} (\varepsilon \times 10^3)^{0.593} Vs^{0.4}$
Neale and Pinches (1994)	Slurry	$k_{gl}a_g = 0.0069 (P/V)^{0.52} Vs^{0.24}$
Schlutter and Deckwer (1992)	Biological system	$k_{gl}a_g (v/g^2)^{1/3} = 7.94 \times 10^{-4} \{(P/V)/[\varrho(vg^4)]^{1/3}\}^{0.62}$ $\{(q_g/V)(v/g^2)^{1/3}\}^{0.23}$
Oguz et al. (1987)	Slurry in water	$k_{gl}a_g [V_{sl}/(q_g \times 3600)] = 2.173 \times 10^3 \{[P/(q_g \times 3600)]/ [\varrho_{sl}(v_{sl}g)^{2/3}]\}^{0.607}$
Oguz et al. (1987)	Slurry in water	$k_{gl}a_g = 6.6 \times 10^{-4} (\mu_{sl}/\mu)^{-0.39} (P/V_{sl})^{0.75} (q_g/60)^{0.5}$

From the investigations on a range of particle sizes (7 to 109 μm), Lee et al (1982) have introduced the following quantitative concepts for the adverse effect of inert solid particles on gas-liquid mass transfer rate.

- particles much smaller than the film thickness around the bubble are supposed to modify the diffusion path, similarly to heat conduction in porous media.

- particles of a size comparable to the film thickness may have a blocking effect and reduce the surface area that is really active in mass transfer

- larger particles may cause deformation or even penetrations of the bubble

Inflence of process conditions and solution conditions on gas-liquid mass transfer

Variation in temperature, pressure, ionic concentration, pH etc. induce changes in gas solubility and diffusivity, which in turn, result in variation in gas-liquid mass transfer rate. Influence of the above parameters on gas solubility and diffusivity has been well studied (Charpentier, 1981; Rehm and Reed, 1985; Harvey, 1996).

Enhancement in gas-liquid mass transfer rate due to suspended particles

Enhancement in gas-liquid mass transfer rate due to suspended particles which are not inert, has been reported (Beenackers and Van Swaaiji, 1993) in the following cases:

a) Particles in the mass transfer zone adsorb the transferred gas phase component only physically (also known as the shuttle mechanism or grazing particles).

b) Particles in the mass transfer zone catalyze a chemical reaction involving the transferred gas phase component

c) Particles in the mass transfer zone react with the transferred gas phase component

d) Particles in the mass transfer zone dissolve and the dissolved reactant reacts with the transferred gas phase component

Anurag Mehra (1994) has given a quantitative description of the enhancement in rate of gas absorption into reactive slurries constituted by fine particles of a sparingly soluble reactant when the particle size is smaller than the characteristic diffusional length of the reactive species. The use of fine particles with high adsorption capability induced enhancement in gas-liquid mass transfer rate during catalytic hydrogenation of adiponitrile over Raney nickel particles (Vuillamin et al, 1996). This has been explained as the result of solid particles acting as hydrogen carriers and a 'shuttle mechanism'.

Solid-liquid mass transfer

The rate of transfer of a solute from the bulk liquid phase to the surface of suspended solids is given by

$$R_{sl} = k_{sl}a_s (C_b - C_s) \tag{2.10}$$

where k_{sl} is the solid-liquid mass transfer coefficient and C_b and C_s are the concentrations of the solute in the bulk liquid phase and at the surface of the particle, respectively. The mass transfer coefficient is related to the hydrodynamics and fluid properties through the relationship,

$$Sh = 2 + ARe^m Sc^n \tag{2.11}$$

where A, m and n are constants.

Pangarker et al. (1991) have summarised various solid-liquid mass transfer correlations along with various systems and techniques employed for the determination of solid-liquid mass transfer coefficient in mechanically agitated

reactors. There are three approaches put forward in the literature for developing *solid-liquid mass-transfer correlations in mechanically agitated reactors.* The first approach is based on developing Reynolds number in Eq.2.11 in terms of the reactor dimensions and agitater speed (Boon-Long *et al.*, 1978). These correlations are specific to geometry and scale of the concerned reactors and hence do not find general applicability. The second approach is based on the slip velocity theory which states that the slip velocity of suspended particles can be taken as the terminal settling velocity of a particle in a still fluid (Calderbank and Jones, 1961). The particle Reynolds number is calculated in terms of this slip velocity.

The mechanically agitated system being characterised by turbulence, the most reliable and widely used approaches for solid-liquid mass transfer correlations is based on Kolmogoroff's theory of isotropic turbulence, a brief outline of which is given by Sano *et al.* (1974) and Armanate *et al.* (1989). Kolmogoroff postulated that the characters of the smallest eddies in which the maximum energy dissipation occur were dependent only on the rate of energy dissipation per unit mass of fluid and kinematic viscosity. He deduced the following equations from dimensional reasoning

$$\eta = (\nu/\varepsilon)^{1/4} \tag{2.12}$$

$$v_e = (\nu/\varepsilon)^{1/4} \tag{2.13}$$

where η is the size of eddy in which the maximum energy dissipation occurs, ε is

the power dissipated per unit mass of fluid and v_e is the eddy fluctuation velocity.

Kolmogoroff gave the following expression for the rms of velocity difference, v_d between two points at a distance, d:

$$\eta << d << L, \qquad v_d = (\varepsilon d)^{1/3} \qquad\qquad (2.14)$$

$$d << \eta, \qquad\qquad v_d = (\varepsilon/v)^{1/2} \qquad\qquad (2.15)$$

where L is the scale of turbulence.

Reynolds number calculated in terms of v_d from Eq.2.12 can be substituted into Eq.2.9 to obtain correlations in terms of specific power group $\varepsilon^{1/3}d_p^{4/3}/v$. Correlations in terms of this specific power group, suggested by various investigators, are listed in Table 2.3.

Table 2.3. Solid-liquid mass transfer correlations employing the specific power group

Reference	Particle diameter (mm)	Schmidt number (Sc)	Solid-liquid mass transfer correlation
Levins and Glastonbury (1972)	0.06-1.96	27-3.5x104	$Sh = 2 + 0.5\left(\dfrac{\varepsilon^{1/3}d_p^{4/3}}{v}\right)^{0.62} Sc^{1/3}$
Sano et al. (1974)	0.107-2.85	217-1410	$Sh = \left[2 + 0.4\left(\dfrac{\varepsilon d_p^4}{v^3}\right)^{1/4} Sc^{1/3}\right]\phi_c$ ϕ_c is the shape factor
Asai et al.	0.02-0.96	269-11270	(1986) $Sh = \left\{2^{5.8} + \left[0.61\left(\dfrac{\varepsilon^{1/3}d_p^{4/3}}{v}\right)^{5.8}\right]Sc^{1/3}\right\}^{1/5.8}$
Armanate and Kirwan (1989)	0.006-0.424	420-1.3x105	$Sh = 2 + 5.2\left(\dfrac{\varepsilon^{1/3}d_p^{4/3}}{v}\right)^{0.52} Sc^{1/3}$
Levins (1969)		267-35000	$Sh = 2 + 0.47\left(\dfrac{d_p^{4/3}\varepsilon^{1/3}\varrho}{v}\right)^{0.62} Sc^{0.36}$

Effect of sparged gas on solid-liquid mass transfer

Solid-liquid mass transfer in the presence of sparged gas has been shown to be given by correlations in terms of specific power group such that the energy dissipation rate ϵ is the sum of the contributions of the sparged gas and the stirrer (Asai *et al.*, 1989).

Kinetics of metallic iron dissolution

The mechanism and kinetics of the electro-chemical dissolution of iron has been well investigated, especially at neutral pH conditions typical of Becher process (Javancicevic and Bockris, 1986; Power and Ritchie, 1981). Eqs.2.3 to 2.5 describe the mechanism of electro-chemical corrosion of iron in neutral solutions. The concept of mixed potential may be employed to determine the kinetics (West, 1965; Shreir, 1994). The expression for cathodic potential E_c and anodic potential E_a are:

$$E_c = E_c^o + (RT/\alpha_c n_c F) \ln C_s + (RT/\alpha_c n_c F) \ln i_c^o - (RT/\alpha_c n_o F) \ln i_c$$

(2.16)

$$E_a = E_a^o - [RT / (1 - \alpha_a) n_a F] \ln i_a^o + RT / [RT / (1 - \alpha_a) n_a F] \ln i_a$$

(2.17)

where

E_c^o, E_a^o -   Standard electrode potentials for chathodic and anodic reactions,

i_c^o, i_a^o -   *Exchange current densities for cathodic and anodic reactions, respectively.*

i_c, i_a -   Cathodic current, anodic current

α_c, α_a -   Cathodic transfer coefficient, anodic transfer coefficient

n_c, n_a -   Number of electrons involved in the cathodic and anodic reactions, respectively

The kinetics of electrochemical corrosion is usually determined by measuring the potentials and currents of the two half reactions separately using suitable electrodes. Then the potentials and currents are plotted on the same current potential plot known as Evans diagram. The two polarisation curves will attain the same current magnitude at the point corresponding to the corrosion current. Then the corrosion rate can be computed from the corrosion current.

Ferrous oxidation reaction

Kinetics of ferrous oxidation by dissolved oxygen in acidic solutions has been well studied with relevance to treatment of waste liquors (Iwai *et al.* 1979; Iwai *et al.* 1982), zinc pressure-leach process (Dreisinger and Peters, 1989) etc. The rate equation is of the form

$$R_{Fe^{2+}} = kC_{Fe^{2+}}^{m}\, C_{H}^{n}\cdot P_{O_2} \tag{2.18}$$

In sulphate solutions m = 2 whereas in chloride solutions m = 1. n varies from -0.25 to -1 The rate is also reported to be dependent on sulphate concentration (Dreisinger and Peters, 1989). Activation energy for the reactions is in the range 50 to 80 KJ/mol.

Ferrous oxidation in alkaline solutions has been studied during the preparation
of magnetite particles by the oxidation of aqueous ferrous hydroxide suspensions
(Sada *et al.* 1990). The reaction rate is zero order with respect to Fe^{2+}
concentrations and first order with respect to the concentrations of dissolved
oxygen. In alkaline solutions the reaction is in fast reaction regime.

Hydrolysis and Precipitation

During the oxygen leaching process, the metallic iron content of the reduced
ilmenite dissolves as Fe^{2+} iron by the electrochemical rection, followed by the
oxidation of Fe^{2+} into Fe^{3+}. The formation of oxides of irons as a fine solid phase
is the result of hydrolysis of Fe^{3+} in to soluble polymers and its subsequent
precipitation (Blessa and Matijevic, 1989).

Hydrolysis

The two important mechanisms for the formation of $Fe_2O_3.H_2O$ from
$Fe(H_2O)_6^{3+}$ is olation and oxolation (Blesa and Matijevic, 1989).

Olation

The evaluation of $Fe_2O_3.xH_2O$ from $Fe(H_2O)_6^{3+}$ by the olation mechanism
can be visualised as a polymerisation reaction upon deprotonation. The chain
reaction leading to hydroxo-bridged oligomers or polymers can be represented as

$$[Fe_n(OH)_m (H_2O)_x]^{(3n-m)+} \leftrightarrow [Fe_n(OH)_{m-1} (H_2O)_{x-1}]^{(3n-m-1)} + H^+$$

$$(2.19)$$
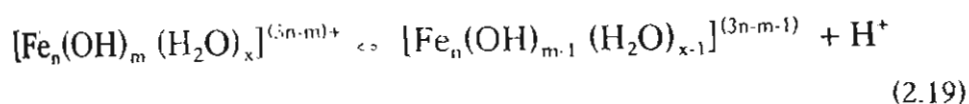
Olation processes are reversible and depolymerisation may be easily achieved by acidifying the solutions.

Oxolation

The second type of polymerisation involved in the formation of hydrous $Fe_2O_3.xH_2O$ is oxolation. In this case, oxo-bridges are formed from two hydroxide ligands through depolymerisation.

$$- Fe - OH + HO - Fe- \rightarrow Fe - O - Fe - + H_2O \qquad (2.20)$$
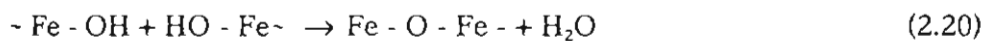
The reactants are polymers of veriable size. Oxolation reaction is irreversible.

Precipitation

Solids can form directly from monomors or small oligomers as well as by the intervention of larger polymers. Stable oxides are formed by the process of dissolution-recrystallisation of amorphous hydrous oxides, initially formed.

$$Fe^{3+} (aq) \rightarrow Fe_2O_3.xH_2O (am) \rightarrow \alpha - FeOOH \rightarrow \alpha - Fe_2O_3 \qquad (2.21)$$
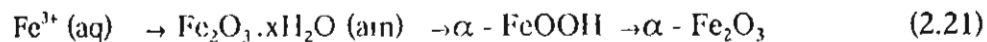
Table 2.1 summarises various forms of iron oxides which can be precipitated depending on the solutions conditions like temperature, pH, anions etc (Ward *et al.*, 1989).

2.4. Analysis of Three phase Hydrometallurgical Oxygen Leaching Models

Accelerated corrosive leaching process for iron removal is essentially a three phase (gas-liquid-solid) reaction system. General models for three phase slurry leaching processes in hydrometallurgy have been proposed by Papangelakis and Demopoules (1992), and Dixon and Hendrix (1993). Pressure leaching processes for zinc, copper, etc are typical examples, and a number of models for them are available (Papangelakis *et al.*, 1986; Baldwin *et al.*, 1995).

In general, a gas-liquid-solid leaching process in hydrometallurgy involves the following reactions;

$$A \text{ (gas)} \rightarrow A \text{ (aq)} \tag{2.22}$$

$$A \text{ (aq)} + bB \text{ (S)} \rightarrow cC \text{ (aq)} + dD \text{ (aq)} \tag{2.23}$$
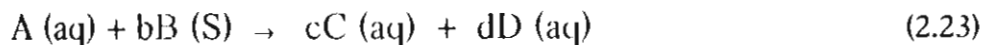
The main types of rate processes taking place during leaching are:

(1) mass transfer of the reacting gas (usually oxygen) from the gas to aqueous phase.

(2) mass transfer of the reacting gas from the aqueous phase to the solid surface.

(3) Reaction at the solid surface

(4) Oxidation of the dissolved metal in the aqueous phase

(5) Precipitation of the oxidised species.

In the case of porous solids, one more step is involved viz. prous diffusion.

27

Pressure leaching processes for the ores of zinc, gold and copper etc involve the same rate processes as encountered in the ammoniacal oxygen leaching process for iron removal. In all these processes the reacting gas is oxygen and involve iron dissolution, aqueous phase oxidation and precipitation. Pressure oxidation of arsenopyrite is a typical exampale and involves the following iron dissolution, aqueous phase oxidation and precipitation reactions:

$$4FeAsS \text{ (s)} + 13O_2 \text{ (g)} + 6H_2O \rightarrow 4H_3AsO_4 \text{ (aq)} + 4Fe^{2+} \text{ (aq)} + 4SO_4^2$$

$$(2.24)$$

$$2Fe^{2+} \text{ (aq)} + \tfrac{1}{2}O_2 \text{ (g)} + 2H^+ \text{ (aq)} \rightarrow 2Fe^{3+} \text{ (aq)} + H_2O \qquad (2.5)$$

$$Fe^{2+} \text{ (aq)} + H_3AsO_4 \text{ (aq)} \rightarrow FeAsO_4 \text{ (s)} + 3H^+ \text{ (aq)} \qquad (2.26)$$
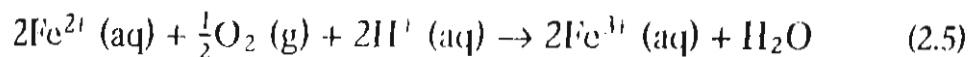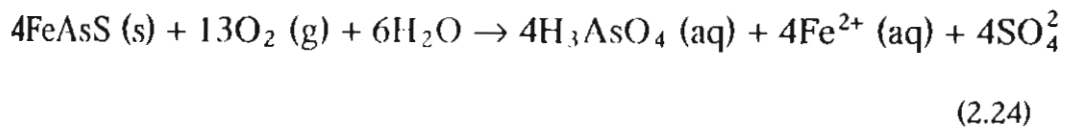
Another closely related system is pyrite oxidation in alkali solution which also involves iron dissolution, aqueous phase oxidation and precipitation (Ciminelli and Osseo-Assare, 1995).

Analysis and Comparison of various models

An analysis and comparison of various models for the above systems can be done as given in Table 2.4.

General Deficiencies of the model

The models of Papangelakis *et al.* (1986); Lin and Sohn (1986); and Ciminelli and Osseo-Asare (1995) do not take into account mass transfer steps or controlling steps. The rate of mass transfer during a process is dependent on reactor

28

Table 2.4. Comparison of three phase hydrometallurgical oxygen leaching models

Reference	System studied	Steps considered	Controlling step	Model
1. Papangelakis and Demopoulos (1992)	General three phase leaching system	Gas-liquid mass transfer, solid-liquid mass transfer and surface reaction	Case A: gas-liquid mass transfer control. Case B: surface reaction control	Case A: liquid phase concentration of oxygen is zero and hence rate is given by $k_g a_g C_i$. Cas B: liquid phase is saturated with oxygen and rate is given by surface reaction control-shrinking core model
2. Papangelakis et al (1996)	Pressure oxidation of arsenopyrite	Surface reaction, homogeneous phase ferrous oxidation and precipitation	Controlling step is not considered	Both isothermal and adiabatic operations are considered. Rate of surface reaction is given by shrinking core model in terms of partial pressure of oxygen. Rate of Fe^{2+} oxidation reaction is given in terms of Fe^{2+} concentration and partial pressure of oxygen. These rate equations are solved along with mass balance equations for various species in the liquid phase
3. H.K. Lin and H.Y. Sohn (1986)	Pressure leaching of copper from primary chalcopyrite ore	External mass transfer to the solid, pore diffusion and surface reaction	Porous diffusion and reaction	Isothermal condition, grain model, numerical solution of equations for porous diffusion and reaction control

Author (Year)	Process	Mechanism	Controlling step	Remarks
4. Susan A. Baldwin et al. (1995)	Oxidative pressure leaching of zinc sulfide concentrate	Gas-liquid mass transfer, dissolution of mineral sulfides, homogenous phase ferrous conditions and precipitation of javosite or iron oxides	Controlling step is not considered	Non-isothermal condition. Heat balance is carried out. Iron dissolution rate and Fe^{2+} oxidation rate is expressed in terms of liquid phase composition of different species. These rate equations are solved along with gas phase and liquid phase material balance equations for different components
5. V.S.T. Ciminelli and K. Osseo-Assane (1995)	Oxidation of pyrite in sodium carbonate solution	Surface reaction	Controlling step is not considered	Rate is expressed as a function of oxygen partial pressure and solution pH. A stochastic model is developed for the conversion
6. V.S.T. Ciminelli and K. Osseo-Assane (1995)	Oxidation of pyrite in sodium hydroxide solution	Surface reaction	Controlling step is not considered	"

characteristics, operating conditions and parameters. A model which does not take into account these aspects is not of general applicability. Papangelakis and Demopoulos (1992) take into account all the constituent steps including the mass transfer steps but consider the extreme cases of $C_b=C_i$ and $C_b=0$. The model of Baldwin et al. (1995) is reliable in this respect. However, the iron dissolution rate is expressed in terms of solution concentrations without assuming any model for heterogeneous phase reactions involving particles. Even though the systems involve the formation of an additional solid phase by precipitation during the process, none of the models take into account the effect of this additional solid phase on mass transfer rates and reaction kinetics.

It is evident from the analysis of the models that they are specific to the system concerned and do not find general applicability. Hence it is proposed to develop a model for the oxygen leaching process in a mechanically agitated contactor which take into account all the constituent steps as well as controlling *steps and predicts the rate, conversion and solution condition as a function of* various operating variables like air flow rate, power input, solid loading, particle size, oxygen partial pressure etc. The proposed model also takes into account the influence of the additional solid phase formed during the process on the mass transfer rates and reaction kinetics.

2.5. Modelling of Oxygen Leaching in the Becher Process: Gap in knowledge base

From the reported investigations on the oxygen leaching step of the Becher process, it is clear that there has not been any effort towards understanding the

process from an engineering point of view. Analysis of the process from this point of view showed that the literature data on the various sub-processes is not adequate for the development of a process model. The following additional aspects are to be studied.

(1) Solid-liquid mass transfer to coarse active particles (reduced ilmenite particles) in the presence of inert micro-particles (iron oxide particles).

(2) Gas-liquid mass transfer in the presence of two solid phases: coarse (reduced ilmenite) and fine (iron oxide) solid phases.

(3) Gas-liquid mass transfer in the presence of coarse active particles (reduced ilmenite).

(4) Kinetics of the ferrous oxidation reaction in the near neutral pH range.

(5) Overall kinetics of the process

SOLID-LIQUID MASS TRANSFER IN THE PRESENCE OF INERT MICRO-PARTICLES*

The work reported in this Chapter has the following objective, namely, to develop a quantitative expression for predicting the mass transfer rates between a dissolved component in liquid and a solid in the presence of inert micro-particles. Since this problem has an intrinsic and widespread merit not yet addressed to by other investigators, the scope of the work has been widened to investigate several micro-particles over a wide size and density range. As we shall see later, solid-liquid mass transfer attenuation due to the presence of inert micro-particles has been interpreted as "mass transfer fouling".

Viewed as a three phase leaching reaction, the presence of micro-particles (iron oxide precipitate) introduced additional complexity to the system under investigation. The micro-particles could be viewed either as a separate phase or its behaviour modelled through a pseudo fluid approach. The pseudo fluid approach has been found to be adequate for representing the hydrodynamic behaviour as in fluidised beds (Gibiloro and Rapagna, 1991) where the effective viscosity of the pseudo fluid is given by

---

$$\frac{\bar{\mu}}{\mu} = 1 + 5.5\ \phi_{mp} \left[\frac{4\phi_{mp}^{7/3} + 10 - (84/11)\phi_{mp}^{2/3}}{10\left(1 - \phi_{mp}^{10/3}\right) - 25\ \phi_{mp}\left(1 - \phi_{mp}^{4/3}\right)} \right] \qquad (3.1)$$

where $\bar{\mu}$ is the pseudo fluid viscosity and ϕ_{mp} is the volume fraction of the micro-particles.

In this chapter, the pseudo fluid concept and the development of micro-particle phase concept are explained with a view to describe the mass transfer of a dissolved component between coarse particles and liquid phase in the presence of inert micro-particles. It is shown that the pseudo fluid concept is not applicable and that presence of inert micro-particles must be treated as a separate phase.

Micro-particle in a turbulent system

In a turbulent system, micro-particles may be defined as particles having size less than the Kolmogoroff's length scale η (Armanate *et al.*, 1989), which is the size of the smallest eddies in which the maximum energy dissipation occurs and is given by Eq.2.12. For the turbulent system investigated in the present study, η was computed as 15 μm. Hence the coarse active particles of size above 200 μm and inert micro-particles of size less than 13 μm employed in this study are separated by the Kolmogoroff's length scale η .

34

3.1. Materials and Methods

The cementation reaction between iron and copper (Agarwal *et al.*, 1988; Lee *et al.*, 1978) viz.

$$Fe + CuSO_4 \rightarrow FeSO_4 + Cu \qquad (3.2)$$

was employed to determine the solid-liquid mass transfer coefficient under the following conditions:

(1) The pH was kept approximately constant at a value of 6.

(2) Inert atmosphere was maintained by nitrogen sparging.

(3) The reaction was carried out in the initial mass transfer controlled stage (t < 5 minutes).

(4) Concentration of copper deposit was less than 2 g/m^2 (as computed from total surface area of solids and time) to ensure that the reaction is not influenced by surface roughness (Majima *et al.*, 1992).

Both the cementation and iron oxidation reactions are electrochemical in nature controlled by the diffusion of cathodic reactant (diffusion of copper ion and dissolved oxygen respectively) and hence the cementation reaction is an ideal analogue to study the solid-liquid mass transfer without interference from gas phase as in the case of the iron oxidation reaction. Cast iron particles were used as the coarse active solid phase while kaolin, silicon carbide, iron oxide alumina and anatase were used as inert micro-particles. The inert particles belonged to two

35

Table 3.1. Characteristics of inert microparticles

Micro-particles	Dispersed condition*				Cementation reaction conditions				Density (kg/m³)
	Mean particle size (μm)	Specific surface area (m²/cm²)	Average diameter from specific surface area d_{mp}# (μm)	d_{50} (μm)	Mean particle size (μm)	Specific surface area (μm)	Average diameter from specific surface area (μm)	d_{50} (μm)	
Anatase	0.36	18.18	0.33	0.36	3.59	4.99	1.20	3.70	3900
Kaolin	2.82	5.31	1.13	2.70	3.80	2.87	2.09	3.50	2600
Ion oxide	2.29	5.65	1.06	2.50	3.31	3.39	1.72	3.60	5240
SiC (A)	4.44	3.19	1.88	3.50	3.85	4.71	1.27	3.50	3200
SiC (B)	16.85	1.05	5.70	17.00	15.32	1.94	3.09	10.00	3200
SiC (C)	28.41	0.49	12.32	28.00	30.01	0.41	14.67	28.00	3200

*The micro-particles were dispersed in 3% sodium tetra pyrophosphate solution (pH 10-11)

#d_{mp} was used as therepresentative particle size in correlations

size ranges: micron and sub-micron ranges. Kaolin, silicon carbide and iron oxide were in the micron size range $(dp > 1\mu m)$ whereas alumina and anatase were in the sub-micron range $(d_p < 1 \mu m)$. The properties of the micro-particles are given in Table 3.1 and 3.2. Particle size distribution and surface area were obtained in a Malvern particle size analyser (Malvern 5000). The size range of coarse active particles (cast iron) used in the study have been so chosen that they correspond to the size of ilmenite employed in industrial reactors.

Table 3.2. Characteristics of micro-particles in the sub-micron range

Substance	Density kg/m³	Mean particle size μm	Specific surface area m²/gm
Anatase	3,900	0.33	4.82
Zirconia	5,800	0.41	14.71
Alumina 10	3,600	0.70	8.56
Alumina 20	3600	0.50	11.90
Alumina 50	3600	0.42	14.41

The experiments were carried out in a mechanically agitated contactor provided with a standard six - bladed Rushton turbine (Nagata.1975) and four equally spaced baffles. A sketch of the reactor with all dimensions are shown in Fig.3.1. The contactor was used either in the batch or continuous mode depending on the volume hold-up of coarse active particles. Fig.3.2 depicts the experimental set-up. Power drawn by the agitator was measured by a power meter (Larson and

37
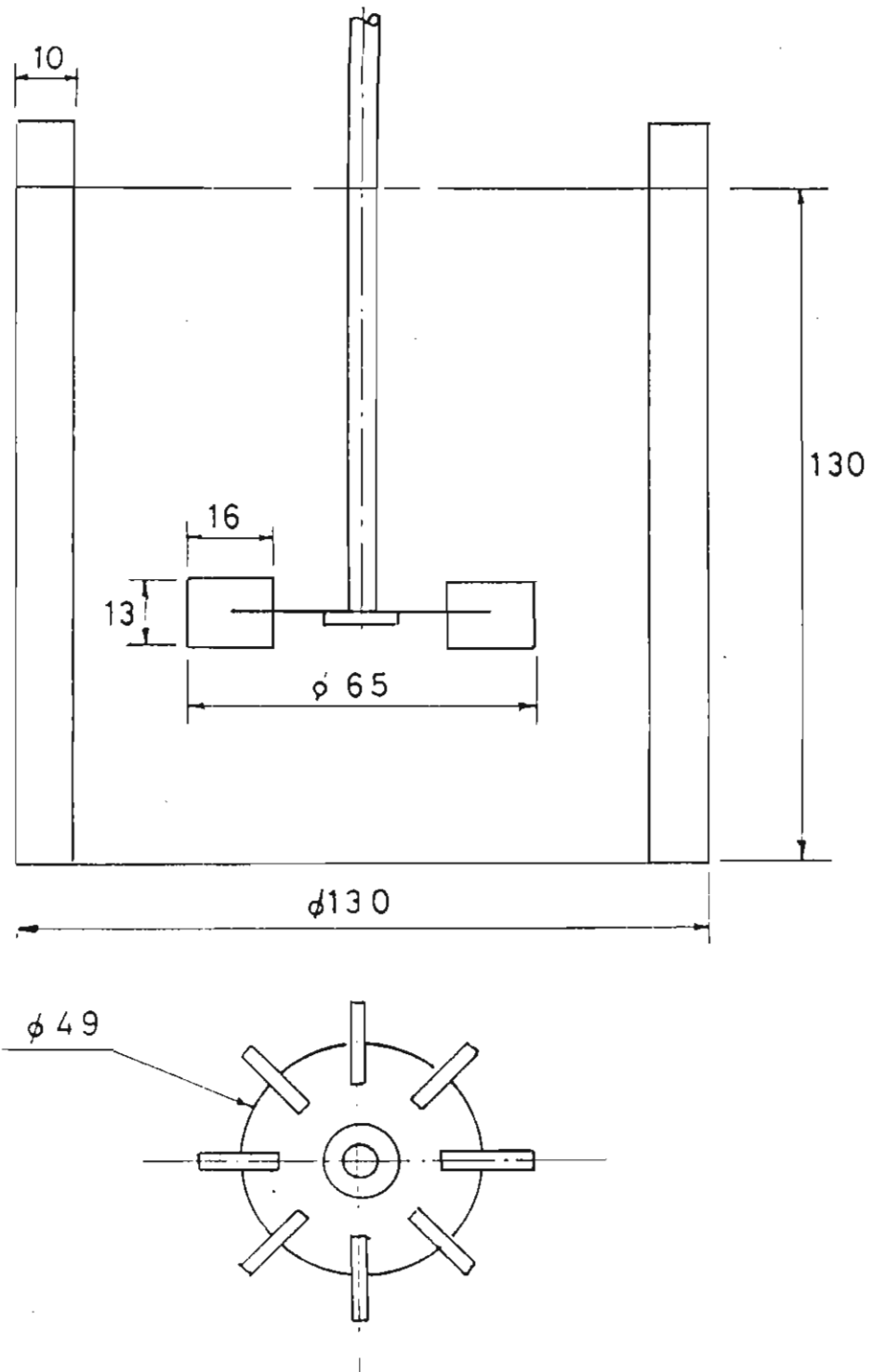
All dimensions are in mm

Fig.3.1. Details of the mechanically agitated contactor

38
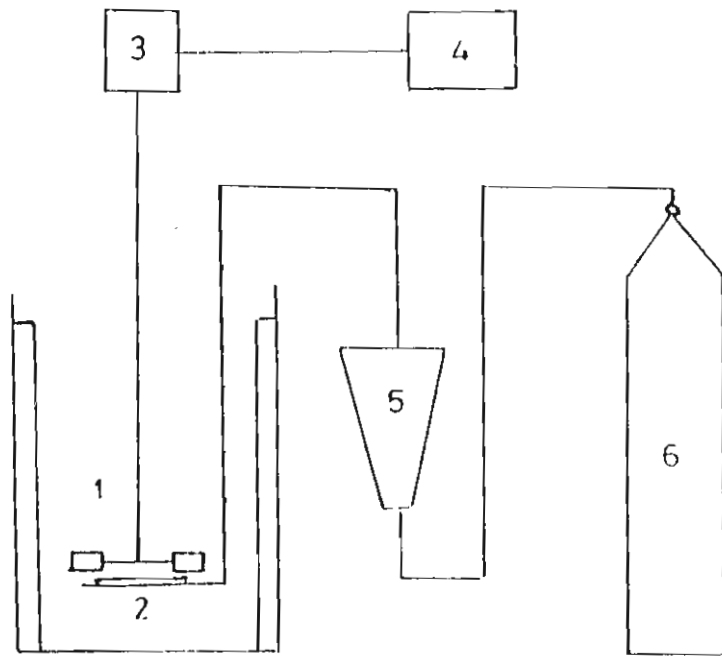
1 Reactor

2 Gas sparger

3 Motor

4 A.C.Power meter

5 Rotameter

6 Nitrogen Cylinder

Fig.3.2. Schematic diagram showing the experimental set up

Toubro) while the impeller speed was measured by a tachometer. The range of process parameters is given in Table 3.3.

Table 3.3. Range of process variables

Parameter	Unit	Range
Speed of rotation of agitator	s^{-1}	3 - 20
Size of cast iron particles	μm	200, 300 and 450
Volume percentage of inert micro-particles	-	0.25 - 6.0
Volume percentage of cast iron particles	-	1, 1.8, 3.3, 6, 9 and 12.8

The kinetics of the cementation reaction was determined at a temperature of $32\pm1^\circ C$. The variation in pH during the reaction was negligible. The concentration of cupric ions was determined by means of titration against sodium thiosulphate solution (Ychya, 1988). During continuous reactor experiments, samples were drawn after the reactor had reached steady state and the analysis of copper was carried out by atomic absorption spectroscopy (Electronic Corporation of India Limited). Prior to mass transfer investigations the micro-particles were kept in copper sulphate solution so as to ensure that the surfaces of the micro-particles were saturated with the diffusing ions.

Calculation of Mass Transfer Coefficient

The solid-liquid mass transfer coefficient, k_{sl}, in an agitated reactor operating in batch mode is obtained through a differential mass balance of the solute over the reactor volume,

40

$$-VdC_b/dt = Vk_{sl}a_s (C_b - C_s) \tag{3.3}$$

where C_b and C_s are the concentrations of solute in the bulk solution and at the solid surface respectively. In the case of electrochemical reactions C_s is always zero. Hence integrating equation (5), we obtain:

$$-\ln (C_f/C_o) = k_{sl}a_s t \tag{3.4}$$

where C_o and C_f are the initial and final concentrations respectively of solute in the bulk solution.

For the continuous stirred reactor operating at steady state, the mass balance for the solute over the reactor volume is

$$F (C_{in} - C_{st}) = Vk_{sl}a_s c_{st} \tag{3.5}$$

where F is the flow rate of $CuSO_4$ solution, C_{in} is the inlet concentration of Cu^{2+} ions and C_{st} is the steady state concentration of Cu^{2+} ions in the reactor.

3.2. Results and Discussion

The suitability of the cementation reaction to predict solid-liquid mass transfer coefficient in a mechanically agitated contactor was verified by two independent criteria.

(i) The identification of critical velocity for solids suspension.

41

(ii)   Applicability of well established mass transfer correlations reported in the
literature.

Figures 3.3 and 3.4 depict these independent verifications. From Figure 3.3,
the critical speeds for suspension lie between 9.5 and 10 s^{-1}. The critical speeds for
suspension were computed as 9.60, 9.72 and 9.88 s^{-1} using the Zwietering
correlation (Zwietering, 1958).

$$N_c D_a^{0.85} = S v^{0.1} d_p^{0.2} g (\Delta\varrho/\varrho)^{0.45} B^{0.13} \tag{3.6}$$

where N_c is the critical speed, D_a the agitator diameter, v the kinematic viscosity,
d_p the average particle size, g the gravitational acceleration, $\Delta\varrho$ the density
difference, ϱ the fluid density, $B = 10$ x weight of solid/liquid, and S is a constant
representing the type of agitator.   The close agreement between these values is
satisfactory.   Similarly, Fig.3.4 shows that the experimentally obtained mass
transfer coefficients in this work agree well with the prediction of Sano's
correlation (Sano *et al.*, 1974).

**Solid-liquid mass transfer in the presence of inert particles in the micron
range ($d_{mp} > 1$ μm)**

The introduction of inert micro-particles decreases the mass transfer
coefficient to a significant extent. This important behaviour is shown in Fig.3.5 as
a plot of relative mass transfer factor α (ratio of mass transfer coefficients with
and without the presence of micro-particles) versus the volume fraction of

42
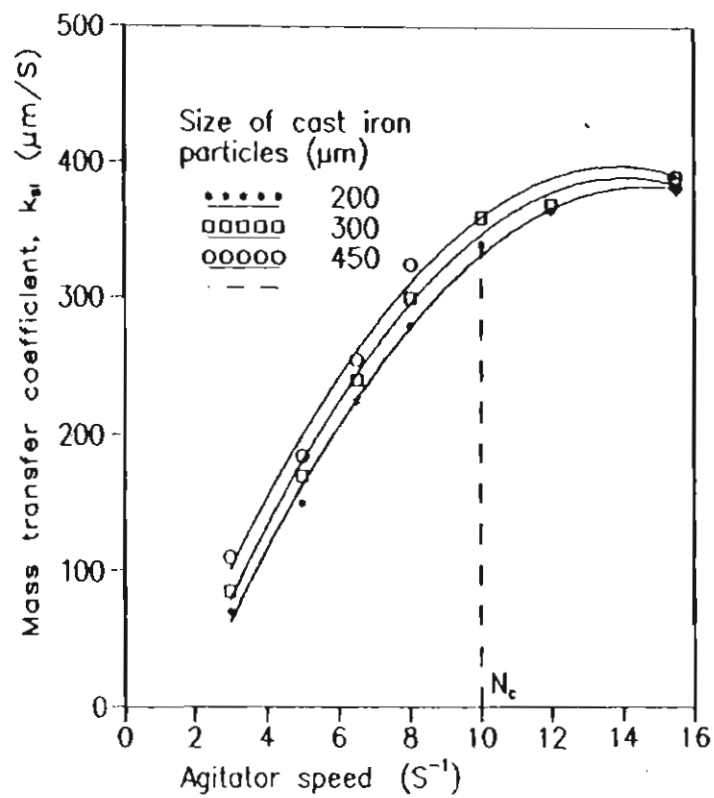
Fig.3.3. Variation of solid–liquid mass transfer coefficient, k_{sl}, with speed of agitator.
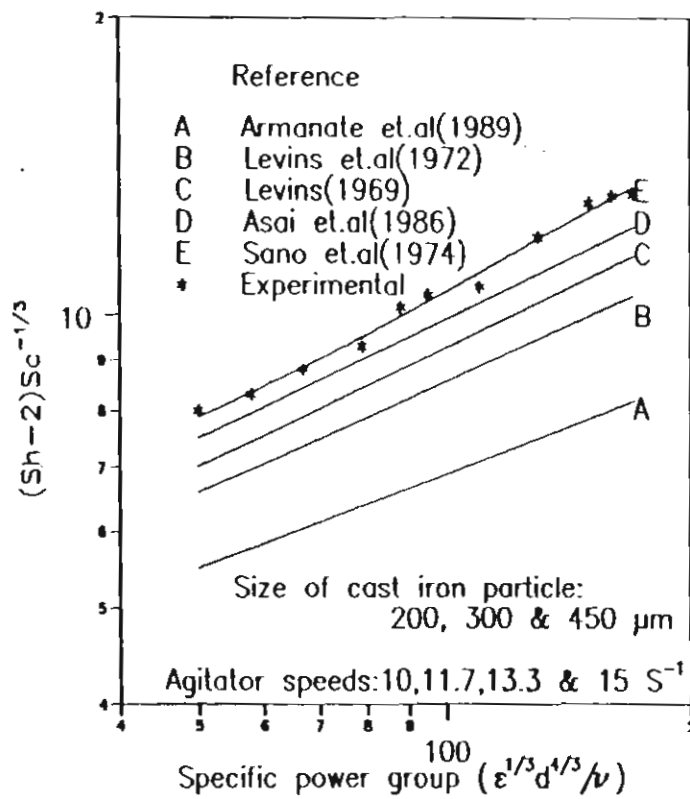
Fig.3.4. Comparison of experimental solid—liquid mass transfer data with various correlations in terms of specific power group.
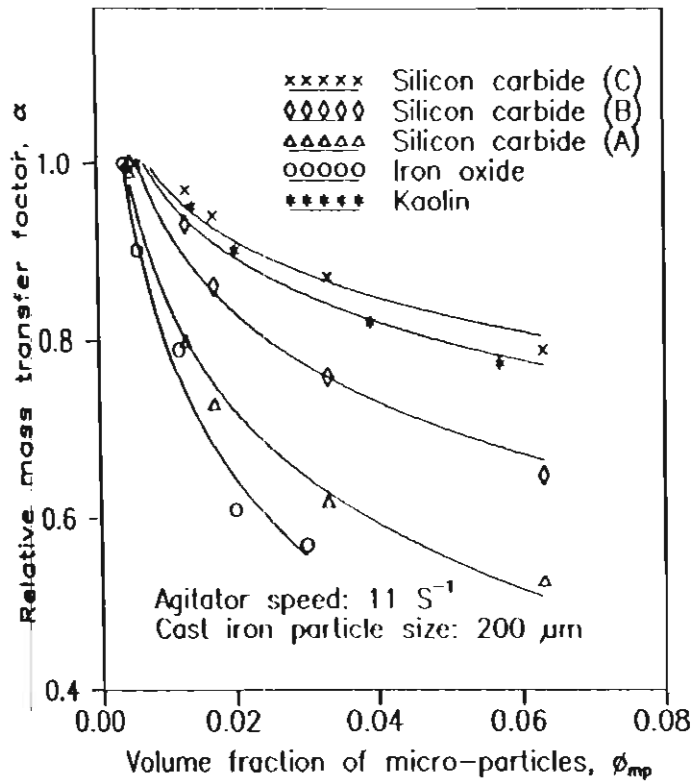
Fig. 3.5 Plot of relative mass transfer factor, α, versus
verses volume fraction of micro-particles, ϕ_{mp}

45

Fig. 3.6. Plot of relative mass transfer factor, α ,versus ϕ^*/ϕ_{mp}

Within the figure:

Relative mass transfer factor, α

ϕ^*/ϕ_{mp}

ooooo Kaolin (1.13 μm)
***** Iron oxide (1.06 μm)
◊◊◊◊◊ Silicon carbide
       (1.80 μm)
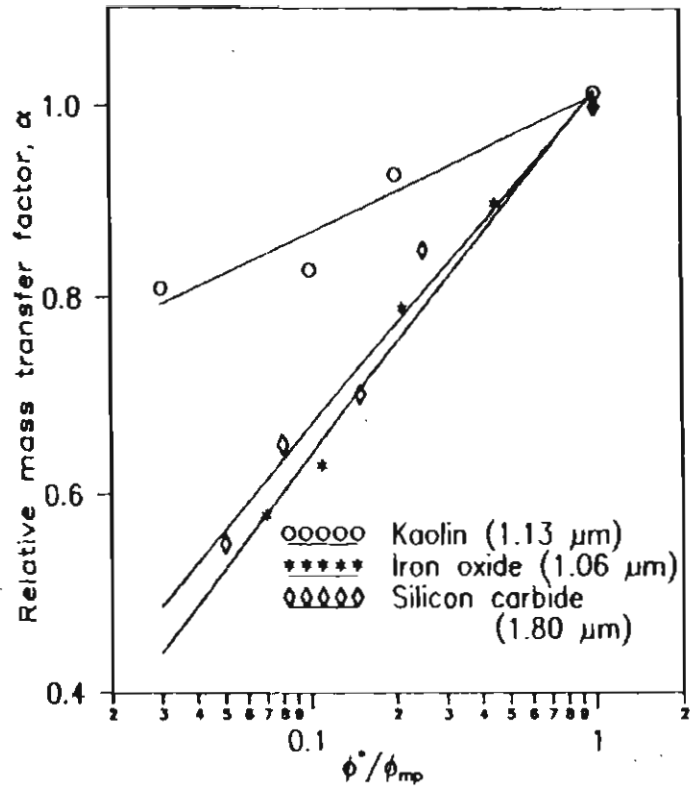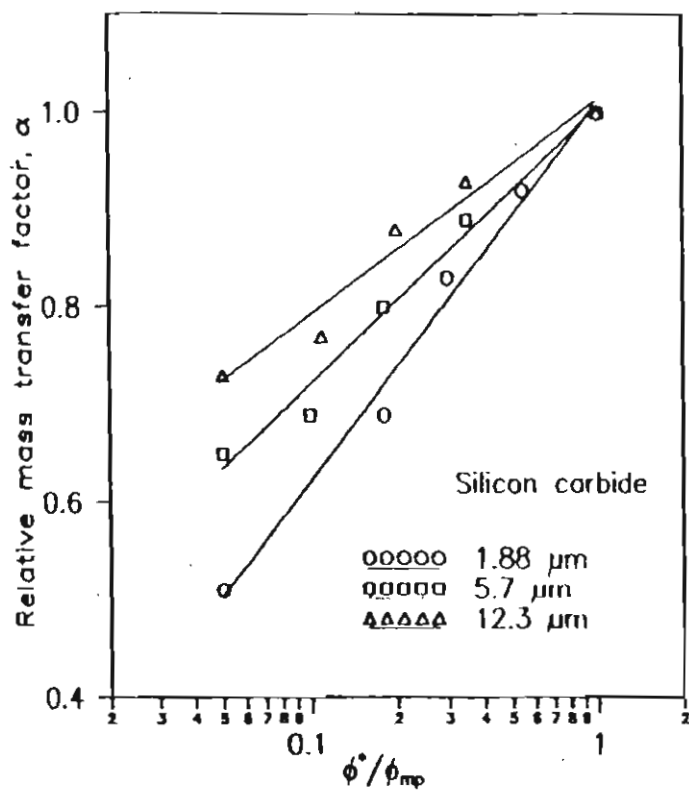
Fig. 3.7. Plot of relative mass transfer factor, α, versus ϕ^{*}/ϕ_{mp} for silicon carbide particles.

47

micro-particles (ϕ_{mp}). Again it is evident that the magnitude of change differs with the type of particles. A threshold value of volume fraction (ϕ^*) below which the mass transfer coefficient is not affected by the presence of micro-particles may also be present. The values are normalised and reploted in Figures 3.6 and 3.7, which could be represented by the expression:

$$\alpha = 1 + \beta \ln (\phi^* / \phi_{mp}) \tag{3.7}$$

The parameters β and ϕ^* are given in Table 3.4. Both β and ϕ^* could be expressed as functions of the density and average particle size of inert micro-particles as follows:

$$\beta = 4.33 \times 10^{-5} d_{mp}^{-0.3.2} \varrho_{mp}^{1.05} \tag{3.8}$$

$$\phi = 0.17 d_{mp}^{0.12} \varrho_{mp}^{-0.52} \tag{3.9}$$

Table 3.4. Values of mass transfer attenuation factor (β) and threshold volume factor (ϕ^*) of the inert micro-particle

Micro-particle	β	ϕ^*
Anatase	0.19	0.0020
Iron oxide	0.17	0.0027
Kaolin	0.09	0.0034
Silicon carbide 91.8 μm)	0.156	0.0028
Silicon carbide (5.7 μm)	0.131	0.0030
Silicon carbide (12.3 μm)	0.086	0.0035
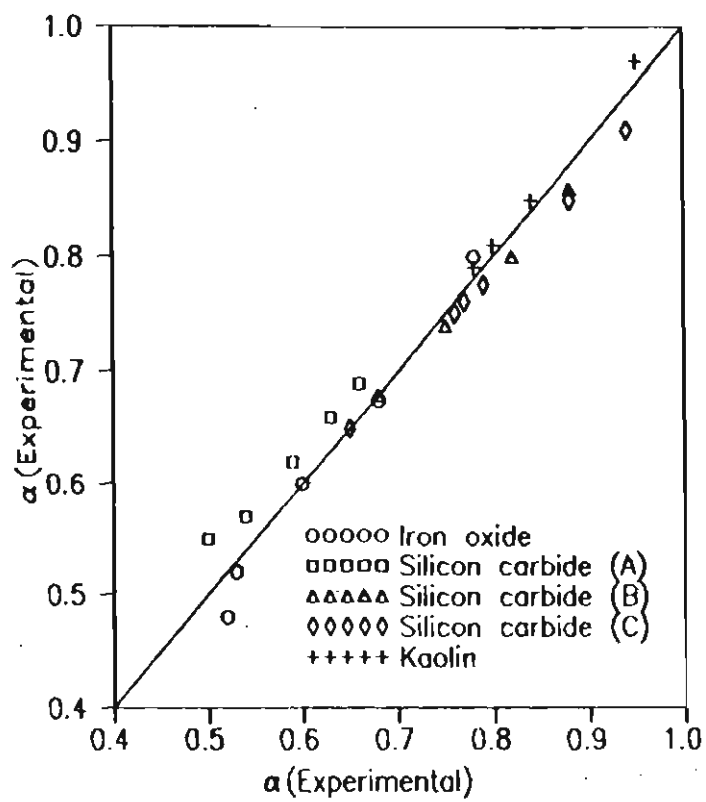
Fig. 3.8. Plot of α (experimental) versus α (calculated)

49

he following ranges are covered

$$1.0 < d_{mp} < 13 \ \mu m$$

$$2600 < \varrho_{mp} < 5300 \ kg/m^3$$

$$0 < \phi_{mp} < 0.06$$

Figure 3.8 shows the parity plot of experimental and calculated α values
om equation 3.7). The agreement is found to be satisfactory (standard deviation
3.6%).

**lid-liquid mass transfer in the presence of inert particles in the sub-micron
nge ($d_{mp} < 1 \ \mu m$)**

The magnitude of the attenuation in solid-liquid mass transfer coefficient k_{sl}
shown in Fig.3.9 as α versus ϕ_{mp} plots. Comparison of Figs. 3.5 and 3.9 clearly
ows that under the conditions of identical volume fractions, inert particles in the
b-micron range induce larger reduction in solid-liquid mass transfer rates than
ien they are in the micron size range.

reological and Colloidal Characterisation of Micro-Particle Laiden Slurry

Rheological characterisation of micro-particle laiden slurry were carried out
order to determine whether the increase in the effective fluid viscosity, making
e of the pseudo fluid concept, can be attributed to the solid-liquid mass transfer
tenuation. The measurement of rheology of the suspensions were carried out in a
Rheomat 30 viscometer at different volume fractions of the micro-particles and
were found to follow the Bingham plastic behaviour given by,
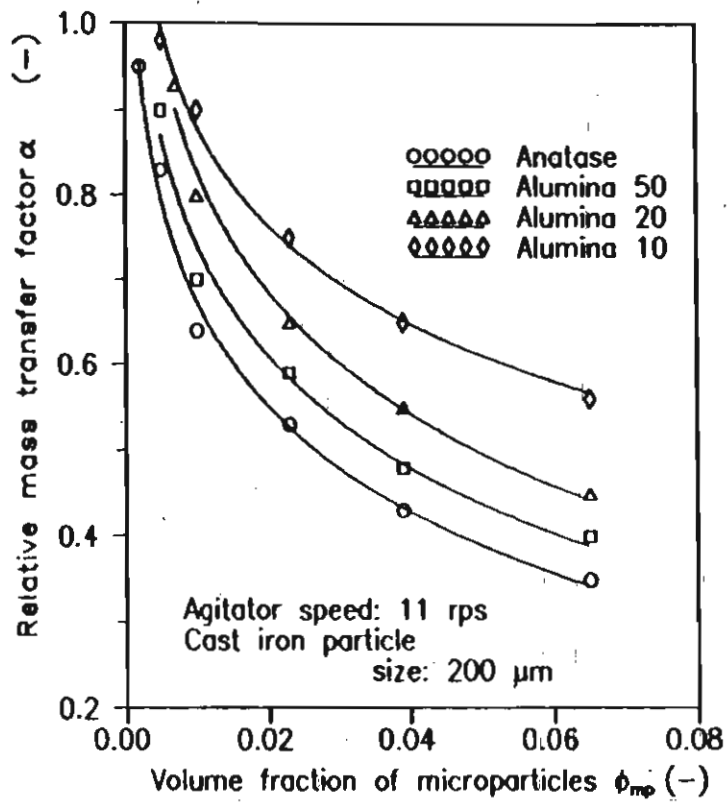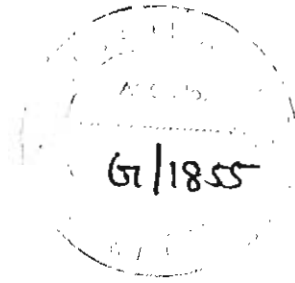
Fig. 3.9. Plot of vlume fraction of microparticles in the sub-micron size range versus relative mass transfer factor

51

$$T = T_o + \mu\gamma \tag{3.10}$$

where $T_o = ae^{b\phi_{mp}}$, $\qquad \mu = me^{n\phi_{mp}}$

The constants **a**, **b**, **m** and **n** were estimated by the regression analysis of the measured T_o and μ values and are listed in Table 3.5. The effective viscosity μ_{ef} of the suspensions under the experimental conditions were computed from the relationship,

$$\mu_{ef} = T/\gamma \tag{3.11}$$

where γ is the shear rate around the impeller, which has been expressed by Kargi and Moo-Young (1985) as

$$\gamma = 10 \times N$$

N is the agitator speed in s^{-1}. The computed μ_{ef} values of various micro-particle suspension at a volume fraction of 0.06 are listed in Table 3.6. Fig.3.10 is a plot of μ_{ef} versus relative mass transfer factor α for various micro-particles, which clearly shows that the change in the rheology of the of the fluid cannot be attributed to the mass transfer attenuation.

Table 3.5. Values of a, b, m and n in Eq.3.10 for various micro-particles

	a	b	m	n
Anatase	0.11	13.10	1.04×10^{-3}	18.5
Kaolin	4.78×10^{-2}	24.10	1.16×10^{-3}	27.85
Iron oxide	0	0	5.05×10^{-4}	22.52
Alumina 10	3.27×10^{-2}	24.9	2.5×10^{-3}	13.38
Alumina 20	1.85×10^{-2}	35.20	3.85×10^{-3}	13.66
Alumina 50	0.20	27.55	5.16×10^{-4}	28.38
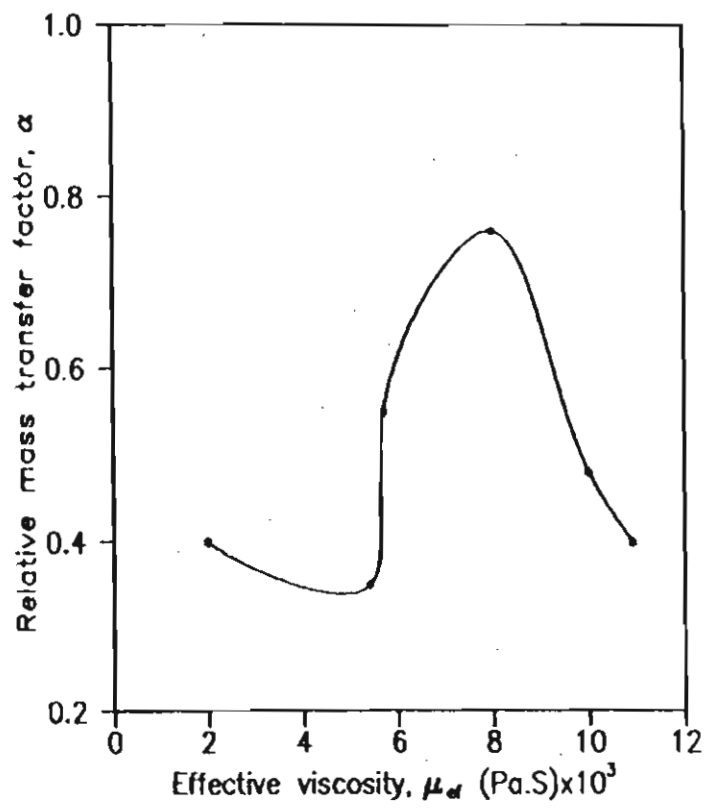
Fig.3.10. Plot of μ_d versus relative mass transfer factor, α

53

Table 3.6. Values of μ_{ef} at a volume fraction, $\phi_{mp} = 0.06$

	μ_{ef}, Pa. S
Anatase	5.3×10^{-3}
Kaolin	7.9×10^{-3}
Iron oxide	2.0×10^{-3}
Alumina 10	6.8×10^{-3}
Alumina 20	1.0×10^{-2}
Alumina 50	1.1×10^{-2}

The colloidal characterisation of the micro particle laiden slurry was carried out by measuring the Zeta potentials of the slurries under the experimental conditions (in 0.002 N $CuSO_4$ solution) in Zeta-Meter system 3.0 +. Zeta potential of alumina is positive whereas for all other micro-particles it is negative (Table 3.7). However, irrespective of the sign of the surface charge, all the micro-particles induce significant mass transfer attenuation. Thus, the mass transfer attenuation due to the presence of micro-particles cannot be attributed to its pseudo fluid behaviour or to its colloidal properties.

Table 3.7. Zeta potentials of micro-particles

	Zeta potential
Iron oxide	- 33.2
Kaolin	- 21.4
Anatase	- 22.0
Alumina	32.96
Zirconia	- 17.4

54

Mass Transfer Fouling due to inert micro-particles

In a mechanically agitated system, the coarse active particles can be considered to be pseudo-stationary compared to the inert micro-particles due to the large difference in their relaxation times. Relaxation times T_p (defined as the time it takes for a particle at rest to be accelerated within 63% of the fluid velocity) of inert micro-particles lie in the range 10^5 to 10^8 S, whereas those of the coarse active particles are of the order of 10^{-2} S. Mass transfer attenuation observed in this system can be explained by analogy with fouling of heat transfer surfaces. Fouling of heat transfer surfaces is the net result of particle transport towards the surface and its removal from the surface (Melo et al., 1988; Muller Steinhagen et al., 1988; Epstein et al., 1988).

Brownian diffusion and inertial impaction are considered to be the main mechanisms of particle transport towards the fouling surface (Muller Steinhagan et al., 1988). The type of mechanism that determines the transport rate has been associated with the dimensionless relaxation time (T_p^+) given by

$$T_p^+ = u^{*2} \varrho_p d_p^2 / 18\mu\gamma \qquad (3.13)$$

where $u^* = $ friction velocity $(u \sqrt{f/2})$

   $u = $ mean fluid velocity

Various authors have given different ranges of T_p^+ for the diffusion controlled regime and inertia controlled regime to be effective. In the inertia controlled regime, deposition velocity is a function of T_p^+ (Papavergos and Hedley, 1984).

For the micro-particle removal process, Rampal and Leighton (1994) have provided an interpretation of the removal or resuspension of sedimented particles from a surface in a turbulent system as the result of shear induced migration. Shear induced diffusivity is given by Leighton and Acrivos (1986) as,

$$D_s = \gamma \, a^2 / \hat{D} \tag{3.14}$$

where $\hat{D}$ is given by

$$\hat{D} = \tfrac{1}{3} \, \phi_{mp}^2 (1 + \tfrac{1}{2} \, e^{8.8\phi_{mp}}) \tag{3.15}$$

γ is the shear rate, a the radius of the particle and ϕ_{mp} the volume fraction of micro-particles.

When the inert particles are in the micron size range the dominant mechanism of particle transport towards the surface is inertial impaction, which is a function of T_p^+ (Muller Steinhagen et al., 1988). The micro-particle concentration $C_{s,p}$ developed at coarse active particle surface as a net result of particle transport towards the surface and shear induced removal from the surface will be a function of T_p^+ and shear induced diffusivity D_s. The surface concentration $C_{s,p}$ of

56

micro-particles causes added resistance to molecular diffusion and hence results in solid-liquid mass transfer fouling. The parallel plots (Fig.3.11) of α versus $\ln(T_p^+.Pe_s)^{-1}$ where P_{es} is the Peclet number in terms of shear induced diffusivity, is in accordance with the above interpretation of mass transfer fouling. The y-intercepts were estimated to be $\ln 23.3\phi_{mp}$ and the data were replotted as in Fig.3.12 leading to the final expression.

$$\alpha - \ln (23.3\phi_{mp}) = 0.33 \ln (St.P_{es})^{-1} + 0.27 \qquad (3.16)$$

where Pe_s is the Peclet number in terms of D_s

Sub-micron particles induced mass transfer fouling

When the particles are in the sub-micron range, the dominant mechanism of particle transport towards the fouling surface is Brownian diffusion (Muller-Steinhagen *et al.*, 1988). Brownian diffusion and shear induced diffusion generate opposing flux such that at pseudo steady state conditions, the particle flux due to Brownian diffusion is balanced by the particle flux due to shear induced diffusion at any point on the coarse active particle surface. In other words,

$$-D_s \frac{C_{b,p}}{dz} = D_B (C_{b,p} - C_{s,p}) \qquad (3.17)$$
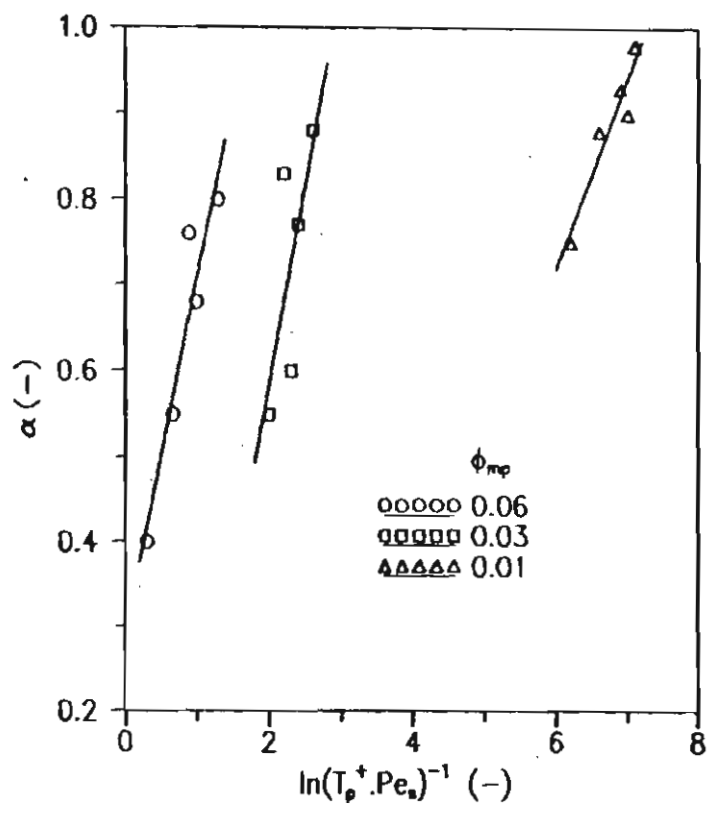
Fig. 3.11.Plot of $\ln(T_p^+ . Pe_s)^{-1}$ versus α for inert particles in the micron size range.
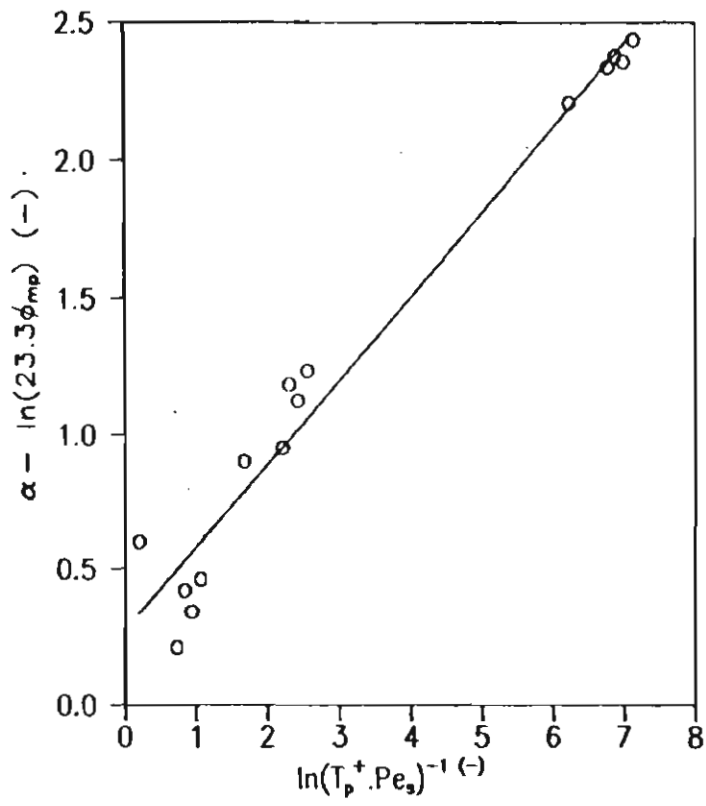
Fig. 3.12.Linear plot of $\ln(T_p^+.Pe_s)^{-1}$ versus $\alpha - \ln(23.3\phi_{mp})$ for inert particles in the micron range.

59

where $C_{b,p}$ and $C_{s,p}$ are the particulate concentration in the bulk liquid and at the coarse active particle surface, respectively, and z is the distance along the coarse active particle surface. Solution of Eq.3 is

$$C_{s,p} = C\, e^{(D_B/D_S)z} + C_{b,p} \qquad (3.18)$$

where C is a constant.

In a turbulent system, according to the surface renewal theory (Briens *et al.* 1993), the solid-liquid mass transfer coefficient k_{sl} is related to the molecular diffusivity D_M and the surface renewal rate s viz.

$$k_{sl}\ (D_M S)^{0.5} \qquad (3.19)$$

The presence of micro-particles has been found to decrease molecular diffusivity and surface renewal rate (Fortuin and Klijn, 1982). Hence, the inert particle concentration $C_{s,p}$ at the surface of the coarse active particle will reduce the solid-liquid mass transfer coefficient so that the reduced mass transfer coefficient $(k_{sl})_s$ and hence a will be a function of $C_{s,p}$, which in turn is a function of D_B/D_s and $C_{b,p}$.

The magnitudes of D_s of the inert sub-micron particles were computed from Eq.(3.14) and magnitudes of D_B were computed as follows using the well known expression reported in the literature (Sami Selim *et al.*, 1993)

60

$$D_{Bo} = k_B T / f_o \tag{3.20}$$

$$\frac{D_B}{D_{Bo}} = 1 + 1.45 \, \phi_{mp} \tag{3.21}$$

where k_B is the Boltzman constant, D_{Bo} is the Brownian diffusivity at infinitely small concentration and ϕ_{mp} is the volume fraction of micro-particle in the bulk liquid phase,

$$f_o = 6 \, \pi \, \mu_o \, a \tag{3.22}$$

where a is the radius of the micro-particle and μ_o is the clear liquid viscosity.

Shear induced diffusivity D_s was computed from the settling velocity of the particle in clear liquid.

Fig.3.13 depicts a plot of a versus $\ln(D_s/D_B)$ for various volume fractions. It is evident that the mechanistic interpretation proposed here is essentially correct since the slopes of the plots for various volume fractions are identical, the y-intercept being dependent on volume fraction of micro-particles. The data was normalised with respect to the bulk volume fraction ϕ_{mp} and is given in Fig.3.14. The factor is expressed as P_{eB}/P_{es} where P_{eB} and P_{es} are Peclet numbers containing D_B and D_s respectively. The final expression is given by,

$$\alpha - \ln (6.62 \, \phi_{mp}^{0.2}) = 0.11 \ln (P_{eB}/P_{es}) - 1.8 \tag{3.23}$$
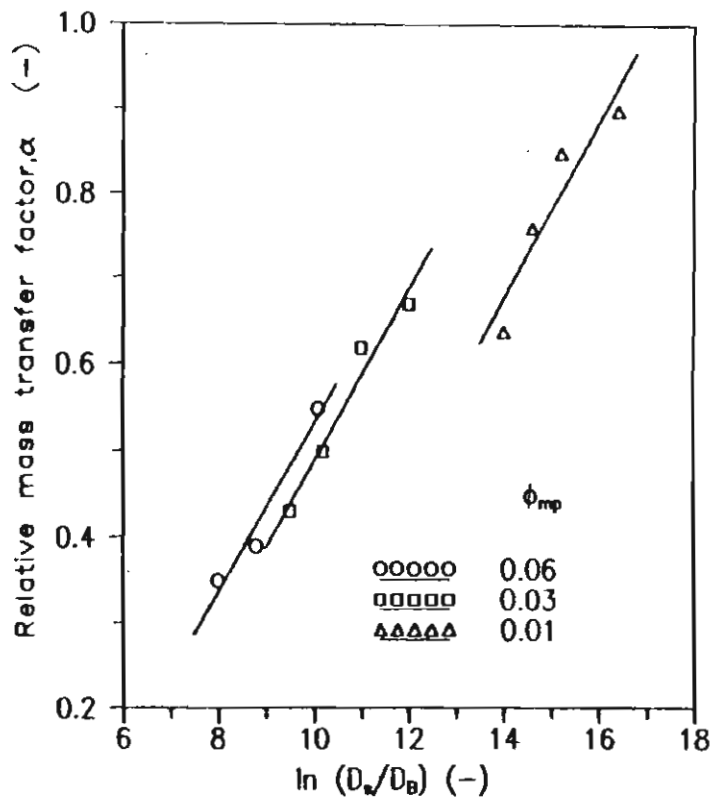
Fig. 3.13.Plot of relative masstransfer factor versus $\ln(D_a/D_B)$ for inert particles in the sub-micron range.

62
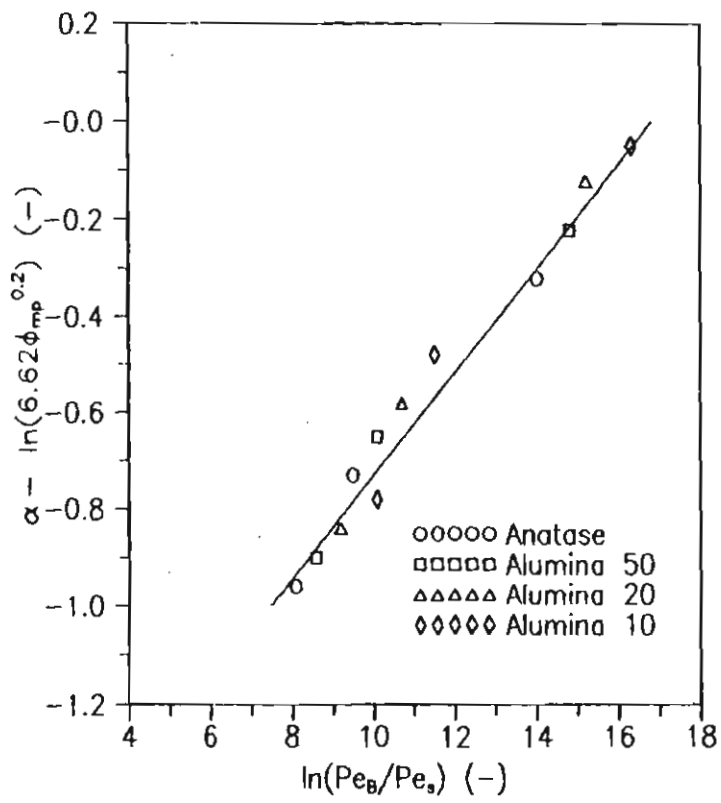
Fig. 3.14.Linear plot of $\ln\left(Pe_B/Pe_s\right)$ versus $\alpha - \ln\left(6.62\phi_{mp}^{0.2}\right)$ for sub-micron sized particles.

Solid-liquid mass transfer in the presence of inert micro-particles with high volume fraction on coarse active particles.

Mass transfer experiments were carried out with cast iron particles upto 40% by volume in the absence and presence of inert micro-particles in the continuous reactor. Solid-liquid mass transfer coefficients and relative mass transfer factors are given in Table 3.8, from which it can be seen that the mass transfer to active particles is influenced predominantly by the volumetric hold-up of inert micro-particles even at high volumetric hold-up of coarse active particles similar to those encountered in industrial processes (Bracanin *et al*, 1980). At comparable concentration, the inert micro-particles thus play the dominant role in reducing the solid-liquid mass transfer coefficient, the actual mechanism of which is still not clear and require further study. An agitator speed of 15 s^{-1} was used in the experiments to ensure suspension of active coarse particles.

Table 3.8. Solid-liquid mass transfer coefficient, k_{sl}, at various volume fractions of cast iron particles in the presence of inert micro-particles

Volume of cast iron particles (%)	k_{sl} ($\mu m/S$)			
	Volume of kaolin micro-particles		Volume of anatase micro-particles	
	3.8%	5.8%	2.6%	3.8%
0.7	390 (0.93)*	370 (0.88)	220 (0.52)	180 (0.43)
2.1	380 (0.90)	380 (0.90)	250 (0.60)	210 (0.50)
4.3	400 (0.95)	360 (0.86)	240 (0.57)	190 (0.45)

*Values of a are given in brackets, agitator speed - 15 S^{-1}

3.3. Conclusions

1) During the iron dissolution reaction in a mechanically agitated contactor, the presence of inert micro-particles significantly reduced the solid-liquid mass transfer coefficient, k_{sl}, by as much as 60%, depending on the volume fraction, size and density of micro-particles. Under the conditions of identical volume fractions, inert particles in the micro size range induce more reduction in k_{sl} than when they are in the sub-micron size range.

2) A new correlation was developed for the relative mass transfer factor, a, in terms of average particle size, density and volume fraction of the inert micro-particles. The mass transfer attenuation phenomena has been interpreted in analogy with heat transfer fouling and modified correlations were developed in terms of Peclet numbers and dimensionless relaxation time.

3) The reduction in the solid-liquid mass transfer coefficient was found to be independent of the volume fraction of the coarse active particles.

65

GAS-LIQUID MASS TRANSFER IN THE PRESENCE OF INERT SOLID PARTICLES

The work reported in this chapter seeks to determine the magnitude and manner of influence of the multi-solid phase containing both coarse and micro-particles as gas-liquid mass transfer rates by an experimental technique, namely, sulphite oxidation technique.

During the oxygen leaching process for iron removal, gas-liquid mass transfer takes place in the presence of two types of solids viz. coarse solid phase (ilmenite, $(d_p)_{av} = 200$ μm) and micro solid phase (iron oxide, $(d_p)_{av} = 1.06$ μm). There is extensive data on gas-liquid mass transfer in the presence of inert solids (Section 2.3) expressed in terms of slurry viscosity and volume fraction of solids-volumetric gas-liquid mass transfer coefficients in the presence of inert coarse particles have been correlated by various investigations (Beenackers et al. 1993) as,

$$(k_{gl}a_g)s = k_{gl}a_g (1 - b\phi) \qquad (4.1)$$

However, there is not any information on how b varies with the type and size of the solid particles. Also, there is not any information on gas-liquid mass transfer rate in the presence of two type of solids - coarse and fine particles.

Gas-liquid mass transfer rate measurements were carried out in the presence of ilmenite particles and synthetic iron oxide particles (with no simultaneous

solid-liquid mass transfer) separately and then in the presence of mixtures of these two solid phases in an agitated reactor in order to find out the role of these particles in modifying the gas-liquid mass transfer rate during the iron removal process.

4.1. Materials and Methods

Dynamic methods for gas-liquid mass transfer rate measurements were not found suitable for this study because of the fouling and damage to the measuring probes caused by the solid particles. Sodium sulphite oxidation under the conditions of slow reaction regime was selected as the measuring technique (Ruchi et al., 1985). The equation is

$$2Na_2SO_3 + O_2 \rightarrow 2Na_2SO_4 \tag{4.2}$$

In the slow reaction regime the rate of oxygen transfer through the gas-liquid boundary is equal to the rate of oxygen consumption through reaction in the bulk liquid and the concentration of oxygen in the bulk liquid is almost zero.

$$k_{gl}a_g (C_i - O) = r_{O_2} \tag{4.3}$$

where $k_{gl}a_g$ is the volumetric gas-liquid oxygen mass transfer coefficient, C_i is the concentration of oxygen at the gas-liquid interphase and r_{O_2} is the rate of reaction of oxygen. From Eq.(4.1)

$$r_{SO_3} = 2r_{O_2} \tag{4.4}$$

where r_{SO_3} is the rate of oxidation of sulphite. From Eqs.(4.2) and (4.3)

$$r_{SO_3} = 2k_{gl}a_gC_i \tag{4.5}$$

67

For batch operation,

$$\frac{dC_{SO_3}}{dt} = 2k_{gl}a_g C_i \qquad (4.6)$$

.

where C_{SO_3} is the concentration of sulphite in the reactor. Following the change in concentration of sulphite with time, the volumetric gas-liquid oxygen mass transfer coefficient can be determined. The following conditions were maintained to ensure the slow reaction regime (Ruchi *et al.* 1985).

Na_2SO_3	800 mol m^{-3} (initial concentration)
NaHCO$_3$	250 mol m^{-3}
Total ionic strength	250 ion m^{-3}
T	305±2"K
pH	8.2

The experimental set up is the same as in Fig.3.2. Measurements were made at a temperature of 305±1"K. Sulphite oxidation was carried out in a batch mode. Steady state conditions were realised after 30 minutes. Samples were withdrawn at intervals of 10 minutes. The sulphite concentration was determined iodimetrically. Values of $k_{gl}a_g$ were calculated using Eq.4.5. When the experiments were carried out in the presence of iron oxide particles and ilmenite particles, agitater speeds of 12 rps and 16 rps respectively were maintained in order to ensure the suspension of solids. The ranges of parameters used are given in Table 4.1.

Table 4.1. Range of process variables

Parameter	Unit	Range
Speed of rotation of agitator	rps	12,16
Size of ilmenite particles	μm	225
Size of iron oxide particles	μm	1.05
Gas flow rate	m³/S	3×10^{-5}
Volume percentage ilmenite	-	0-7.1
Volume percentage of iron oxide	-	0-3

4.2. Results

The volumetric gas-liquid mass transfer coefficient $k_{gl}a_g$ was calculated with reference to the liquid volume and not to the slurry volume

The experiments with the slurry of ilmenite particles were carried out in the absence of sun light in order to avoid the effect of photocatalytic oxidation caused by ilmenite particles. Gas-liquid mass transfer rate measurements were also carried out in slurries constituted by mixtures.

Upto a volume fraction of 0.001 of iron oxide there is negligible change in $k_{gl}a_g$. Beyond this volume fraction a linear decrease in $k_{gl}a_g$. The relative mass transfer factor $(k_{gl}a_g)_s/(k_{gl}a_g)$ versus volume fraction of iron oxide is plotted in Fig.4.1, leading to the following linear relationship.

$$\frac{(k_{gl}a_g)_s}{k_{gl}a_g} = 1 - \frac{\phi}{0.052} \qquad (4.7)$$

69
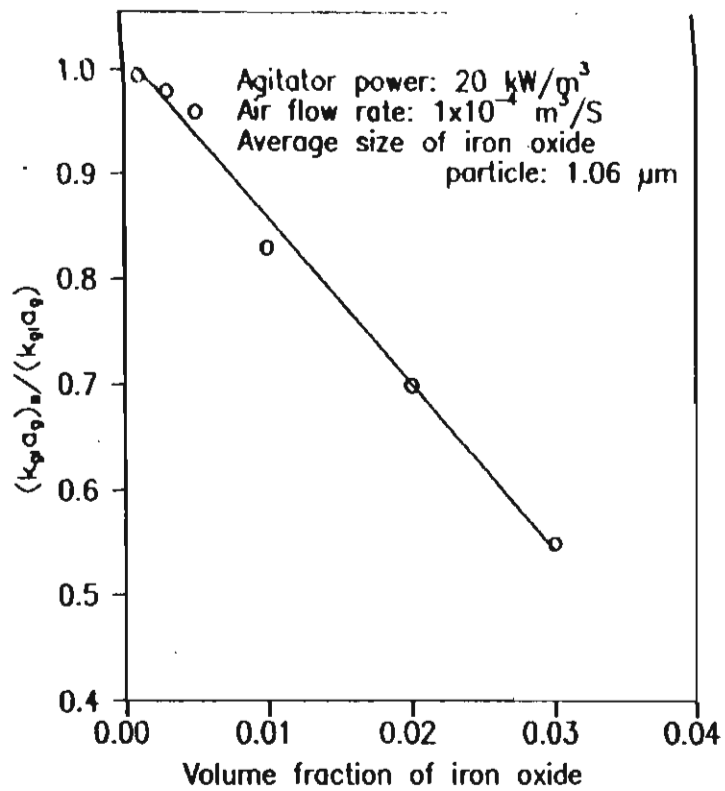
Fig. 4.1. Variation of relative gas-liquid mass transfer coefficient with volume fraction of iron oxide.

where $k_{gl}a_g$ is the volumetric gas-liquid mass transfer coefficient in the presence of iron oxide particles.

Reduction in gas-liquid mass transfer coefficient in the presence of ilmenite particles is depicted in Fig.4.2. An analysis of data leads to the expression

$$\frac{(k_{gl}a_g)_s}{k_{gl}a_g} = 1 - \frac{\phi}{0.45} \tag{4.8}$$

where b is a function of the size and type of solids.

The observed decrease in gas-liquid mass transfer coefficient due to the presence of inert solids is in accordance with the reported data (Section 2.3), showing a linear decrease with volume fraction, ϕ, of the solids, as given in Eq.4.1.

Gas-liquid mass transfer coefficients in the presence of both the solids (ilmenite and iron oxide) are listed in Table 4.2. It can be seen that the mass transfer rate is influenced predominantly by the volumetric hold up of micro-particles even at high volumetric hold up of coarse particles.

Table 4.2. Relative volumetric gas-liquid mass transfer coefficients in the presence of mixture of ilmenite and iron oxide particles - comparison with individual coefficients

$\phi_{iron\ oxide}$	$\phi_{ilmenite}$	$\dfrac{(k_{gl}a_g)_{iron\ oxide}}{k_{gl}a_g}$	$\dfrac{(k_{gl}a_g)_{ilmenite}}{k_{gl}a_g}$	$\dfrac{(k_{gl}a_g)_{mixture}}{k_{gl}a_g}$
0.013	0.083	0.183	0.180	0.361
0.026	0.066	0.361	0.146	0.507
0.039	0.052	0.539	0.115	0.654
0.052	0.033	0.717	0.073	0.790

71
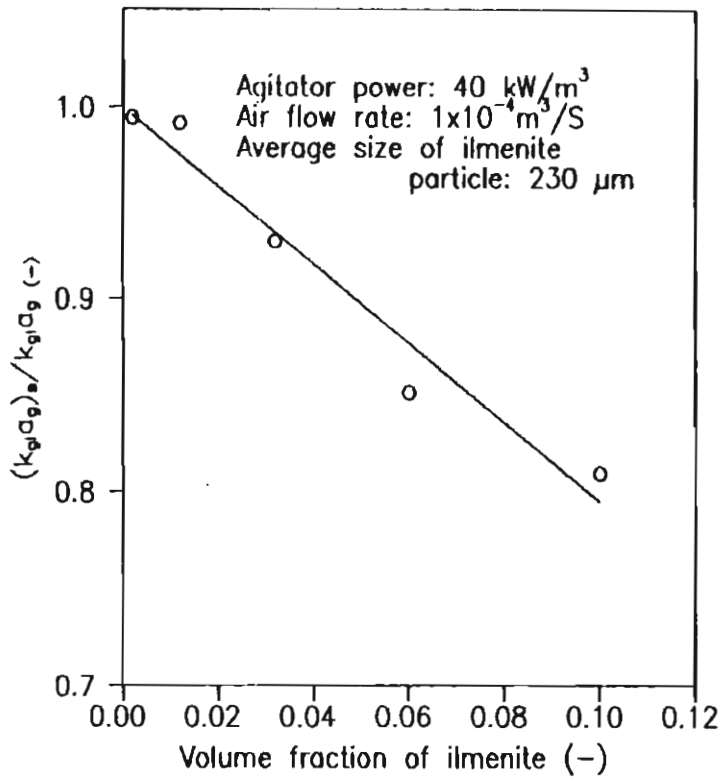
Fig. 4.2. Plot of relative gas–liquid mass transfer factor versus volume fraction of ilmenite.

72

4.3. Conclusions

1. . Reduced volumetric gas-liquid mass transfer coefficients in the presence of iron oxide (micro) and ilmenite micro-particles were correlated in terms of volume fractions of the particles.

2. Under comparable concentrations of micro and macro-particles, micro-particles induced significant reduction in gas-liquid mass transfer coefficient.

CHAPTER V

INVESTIGATIONS ON OXYGEN LEACHING PROCESS FOR IRON REMOVAL FROM NON-POROUS METALLIC IRON PARTICLES

The work reported in this chapter is aimed at developing a steady state process model for the ammoniacal oxygen leaching process for iron removal under isothermal conditions. As a non-porous solid, metallic iron particles of size ranges similar to ilmenite have been employed to experimentally measure the kinetics and validate the model. As an important spin off, the kinetic parameters of the ferrous has also been determined*.

The following reaction sequence is proposed for describing the iron removal process by oxygen leaching.

1. Reactions at the solid surface

(a) Anodic reaction

$$Fe^0 \rightarrow Fe^{2+} + 2e^- \qquad (5.1a)$$

(b) Cathodic reaction:

$$O_2 + 2H_2O + 4e^- \rightarrow 4OH^- \qquad (5.1b)$$

---

2. Reaction in the solid-liquid film

(a) Buffering action of NH_4^+ ions:

$$NH_4^+ + OH^- \rightarrow NH_3 + H_2O \qquad (5.2a)$$

(b) Complex formation:
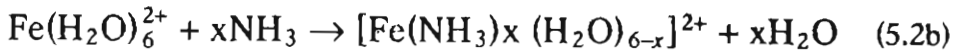
$$Fe(H_2O)_6^{2+} + xNH_3 \rightarrow [Fe(NH_3)x\,(H_2O)_{6-x}]^{2+} + xH_2O \quad (5.2b)$$

3. Reactions in the bulk liquid

(a)
$$[Fe(NH_3)x\,(H_2O)_{6-x}]^{2+} + H_2O \rightarrow Fe(H_2O)_5^{2+} + xNH_3 \qquad (5.3.a.1)$$

$$NH_3 + H_2O \rightarrow NH_4^+ + OH^- \qquad (5.3.a.2)$$

(b) Oxidation of ferrous ions

$$4Fe(H_2O)_6^{2+} + O_2 + 4H^+ \rightarrow 4Fe(H_2O)_6^{3+} + 2H_2O \qquad (5.3.b)$$

(c) Hydrolysis and precipitation

$$Fe(H_2O)_6^{3+} \xrightarrow[\text{precipitation}]{\text{Hydrolysis and}} Fe_2O_3.xH_2O \qquad (5.3c)$$
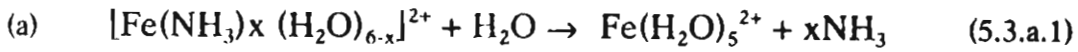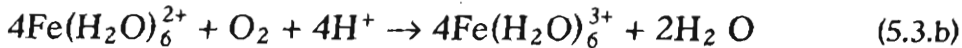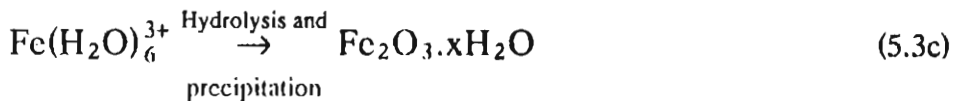
5.1. Development of the model

A pseudo-steady state model for the constant rate phase of the iron conversion process under isothermal conditions is proposed below, based on the following assumptions.

(a) liquid and gas phases are well mixed

(b) the rate of electrochemical dissolution of iron is controlled by the oxygen mass transfer rate

(c) the oxidation of ferrous ions is in the slow reaction regime

(d) the rate of hydrolysis of Fe^{3+} ions is controlled by the rate of oxidation of Fe^{2+} ions in the bulk liquid phase

(e) ferrous ions neither hydrolyse nor precipitate

These assumptions are based on a comparison of the time constants of the sub-processes described in chapter II and given in Table 5.1. Assumption (b), in particular, is based on the report (Farrow et al. 1987) that the rate of electrochemical dissolution of iron is given by the limiting current density of cathodic oxygen reduction reaction.

Table 5.1. Maximum values of time constants for various sub-processes under the operating conditions

Sub-process	Time constant (S)
Mixing	2.1
Gas-liquid mass transfer	9.3
Solid-liquid mass transfer	4.6
Fe^{2+} oxidation	9.7
Hydrolysis	10^{-2}

Taking an oxygen balance over the bulk liquid volume, V

$$V(dC_b/dt) = Vk_{gl}a_g(C_i - C_b) - Vk_{sl}a_s(C_b - C_s) - VR_{O_{2,h}} \quad (5.4)$$

where $R_{O_2,h}$ is the rate of reaction of oxygen through the homogeneous phase reaction (ferrous oxidation, Eq.5.3b)).

From Eq.(5.1a), Eq.(5.1b) and Eq.(5.3b)

$$R_{O_{2,h}} = \frac{1}{2}R_{O_{2,s}} \tag{5.5}$$

Where $R_{O_{2,s}}$ is the rate of oxygen consumption by the electrochemical reaction.

Since the electrochemical dissolution of iron is controlled by the rate of oxygen mass transfer to the surface of iron particles:

$$C_s = 0 \tag{5.6}$$

and

$$R_{O_{2,s}} = k_{sl}a_sC_b \tag{5.7}$$

From Eqs.(5.4)-(5.7)

$$(dC_b/dt) = k_{gl}a_g(C_i - C_b) - \frac{3}{2}k_{sl}a_sC_b \tag{5.8}$$

Assuming steady state

$$k_{gl}a_g(C_i - C_b) = \frac{3}{2}k_{sl}a_sC_b \tag{5.9}$$

The total rate of consumption of oxygen by electrochemical and ferrous oxidation reaction is given by

$$R_{O_2} = k_{gl}a_g(C_l - C_b) \tag{5.10}$$

77

From Eq.(5.9) and Eq.(5.10)

$$(C_1/R_{O_2}) = \frac{2}{3}[(1/k_{sl}a_s) + (1/k_{gl}a_g)]$$ (5.11)

From Eq.(5.1a), Eq.(5.1b) and Eq.(5.3b)

$$R_{Fe} = \frac{4}{3}R_{O_2}$$ (5.12)

where R_{Fe} is the rate of dissolution of iron

5.2. Experimental

The iron removal process by oxygen leaching was carried out in a mechanically agitated contactor. The dimensional details of the reactor are given in Table 5.2. The characteristics of the coarse active particles (iron particles) were

Mesh size	=	+210 - 250 μm
Purity	=	98%
Grade	=	Electrolytic

Table 5.2. Dimensional details of the reactor

Parameter	Value
Internal diameter of the reactor	0.250 m
Diameter of six-bladed disc turbine	0.100 m
Length of blades	0.025 m
Width of blades	0.020 m
Diameter of axial flow turbine	0.125 m
Distance between impeller and tank bottom	0.062 m
Number of baffles	4

The reactor was provided with an external jacket for temperature control by the circulation of water. A six-bladed disc turbine and a four-bladed axial flow turbine were used in the investigations. The experimental equipment is shown in Fig.5.1. The ranges of process parameters studied are given in Table 5.3.

Prior to experimentation on the kinetics of the process, the agitator speeds for the suspension of iron particles under various solid loadings and air flow rates were determined using the Zwietering's criterion (the particles remain at the tank bottom for less than 1 sec). Agitator speeds were kept above those required for suspension, as given in Table 5.4. Iron oxide slurry samples were drawn at regular intervals during the reaction, after ensuring that the mixing in the reactor was sufficient to maintain uniform suspension of iron oxide particles. The slurry samples were acidified with 5 M HCl, boiled for 15 min and were analysed for iron. The removal of iron from the metallic iron particles at various intervals of time was calculated from the estimated values of the iron content of the samples. Iron oxide slurry samples were also withdrawn for the determination of Fe^{2+} ion concentrations. The pH of the slurry samples was reduced to a value around 3 in order to prevent further oxidation of ferrous ions and their subsequent precipitation. The slurry was then filtered and Fe^{2+} ion concentration was determined by colorimetry (Vogel, 1989).

79

1 Reactor
2 Agitator
3 Gas sparger
4 Baffles
5 Jacket
6 DC Motor
7 Power meter
8 Rotameters
9 Dissolved Oxygen probe
10 Pump
11 Probes for pH temperature and oxidation reduction potential
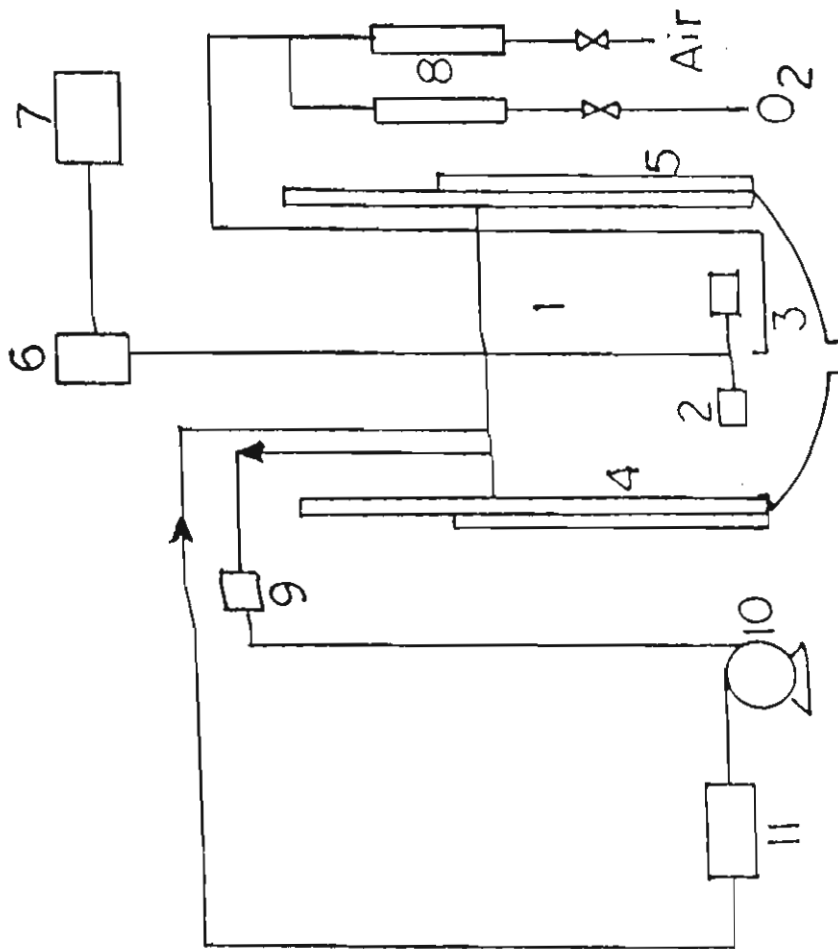
Fig. 5.1. Experimental equipment
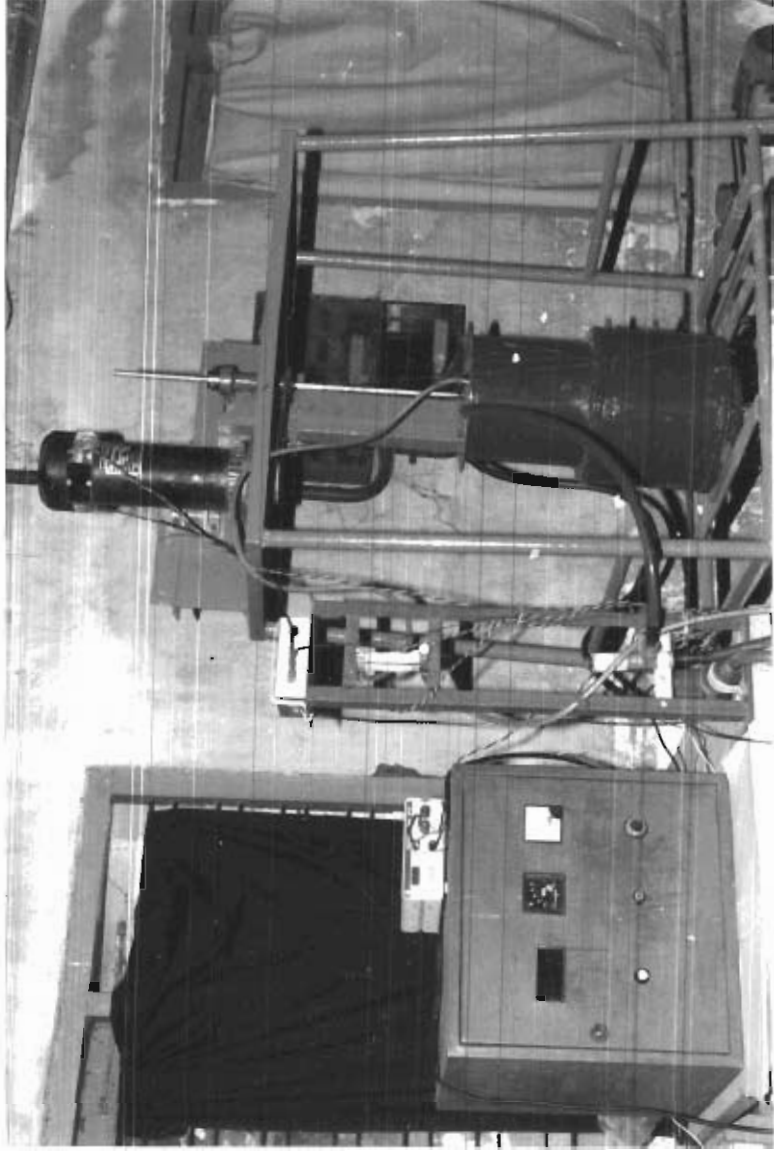
Phtograph of the experimental set up

Table 5.3. Range of process variables

Parameter	Unit	Range
Power dissipation, ε	kW/m^3	8-10
Gas flow rate, qs	m3/s	$8 \times 10^{-3} - 2 \times 10^{-4}$
Weight percentage of iron particles, W	-	5-40
Average size of iron particles, dp	μm	230
Partial pressure of oxygen, $^P\text{O}_2$	Pa	$1.22 \times 10^4 - 1.01 \times 10^5$
Temperature, T	K	305 ± 2

Table 5.4. Minimum agitator speeds for suspension of iron particles, N_c (s^{-1})

Weight percentage of iron particles	Air flow rate (m^3/s) Six-bladed disc tubrine			Downward pumping axial flow turbine		
	0	1×10^{-4}	2×10^{-4}	0	1×10^{-4}	2×10^{-4}
10	7.50	8.30	9.00	8.00	9.00	11.00
20	8.30	10.00	11.70	9.00	10.00	11.70
30	9.00	11.00	12.50	11.00	12.50	13.20
40	11.00	13.30	15.00	12.50	14.00	15.50

Iron oxide slurry was circulated with the help of a magnetic pump (seal-less magnet driven monobloc chemical pump model) for on-line measurement of pH, temperature and oxidation reduction potential (electrodes provided by Ion Exchange India). A silver/silver chloride reference electrode was used for the measurement of

oxidation reduction potential. On-line measurement of dissolved oxygen concentration was carried out by using a dissolved oxygen meter (Oximeter, OX 196). The power input to the system was measured using an AC power meter (Larson and Toubro).

5.3. Model validation

A linear relationship between iron conversion (dissolution) and time was observed for various process conditions investigated in this work at low partial pressures of oxygen ($<2.0 \times 10^4$ Pa). A typical plot is given in Fig.5.2.

The mass transfer coefficients required for the computation of iron conversion rates from the model equation; namely, the solid-liquid and gas-liquid mass transfer coefficients, were calculated using the correlations reported in the literature. The various correlations for volumetric gas-liquid mass transfer coefficient ($k_{gl}a_g$) used in the analysis are given in Table 2.3. The solid-liquid mass transfer coefficient (k_{sl}) was calculated using Sano's correlation [Sano et al., 1974], since it predicted the solid-liquid mass transfer rate in a similar system in a previous study [Geetha and Surender, 1994]. The saturation concentrations C_i, of oxygen in ammonium chloride solution under various partial pressures of oxygen were found to be the same as those in water (within experimental error). Iron conversion rates were computed from model equations and compared with experimentally obtained values. Close agreement between experimental and predicted values of rates

82
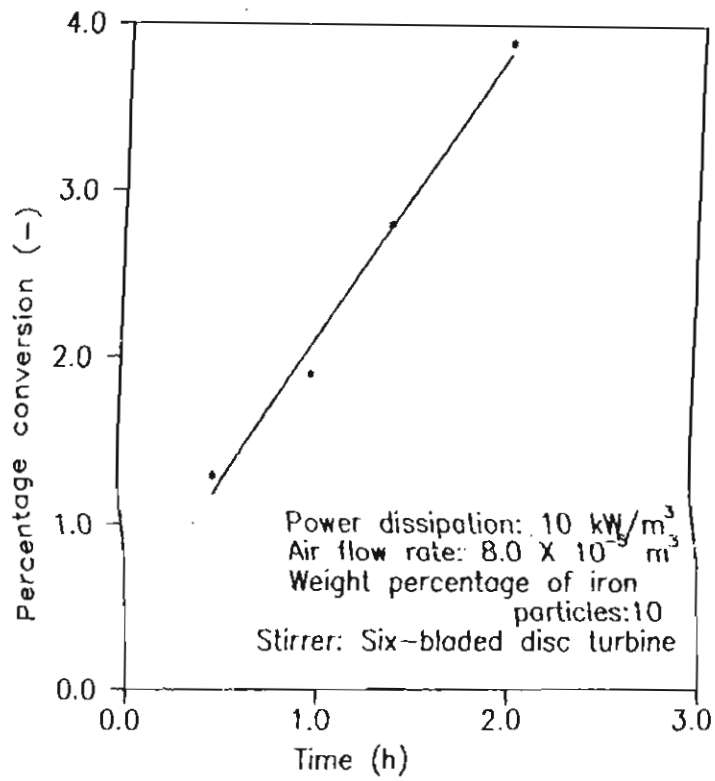
Fig.5.2. A typical plot of percentage conversion of iron versus time.

83

(Fig.5.3) was observed when the correlation proposed by Linck *et al* [1987] was employed for computing $k_{gl}a_g$.

Volumetric gas-liquid mass transfer coefficients in the presence of inert coarse particles have been correlated by various investigators (Beenackers and Swaji, 1993) as

$$(k_{gl}a_g)_s = k_{gl}a_g (1 - b\phi)$$ (5.13)

where $(k_{gl}a_s)_s$ is the volumetric gas-liquid mass transfer coefficient in the presence of solids and ϕ is the volume fraction of solids. Experimental and predicted values of iron conversion rates showed close agreement when b = 0, as shown in Fig.5.4. This surprising results can be due to the fact that the coarse solids in the present study are active to mass transfer, in contrast to the inert solids used by other investigators [Beenackers and Swaji, 1993]. This aspect is discussed in Section 5.5 by suggesting a mechanism.

Table 5.5 compares the predicted and experimentally observed values of dissolved oxygen concentrations in the bulk liquid phase. While at low solid loadings the experimental and predicted values are in agreement at higher solid loadings (greater than 20% by weight) the experimental values are lower than the predicted values. Although the experimentally observed dissolved oxygen concentrations approach zero when the solid loadings are above 25% by weight the iron removal rates are well predicted by the model equation. This important result is discussed further.
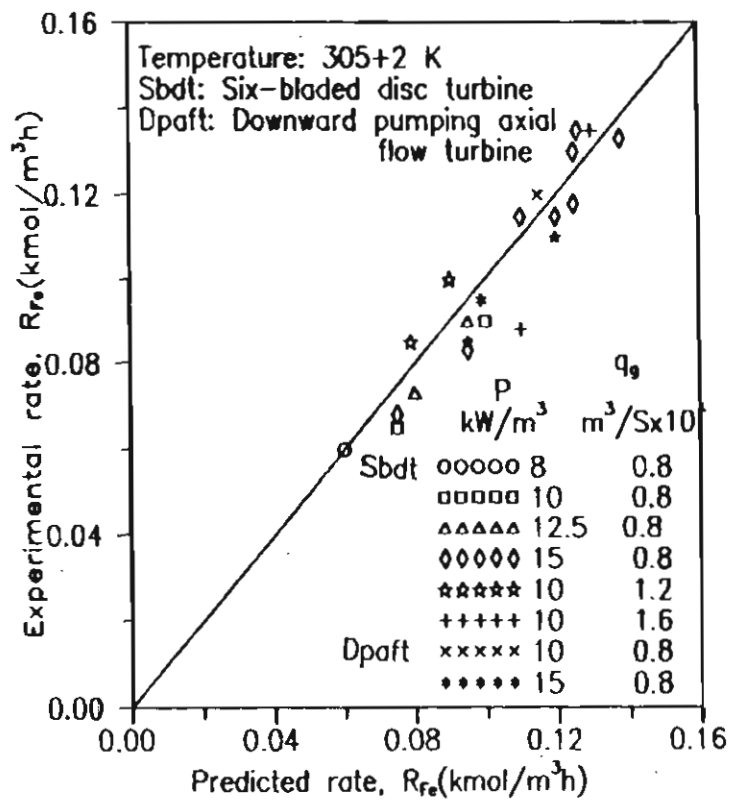
Fig. 5.3. Parity plot of experimental and predicted rates.

85
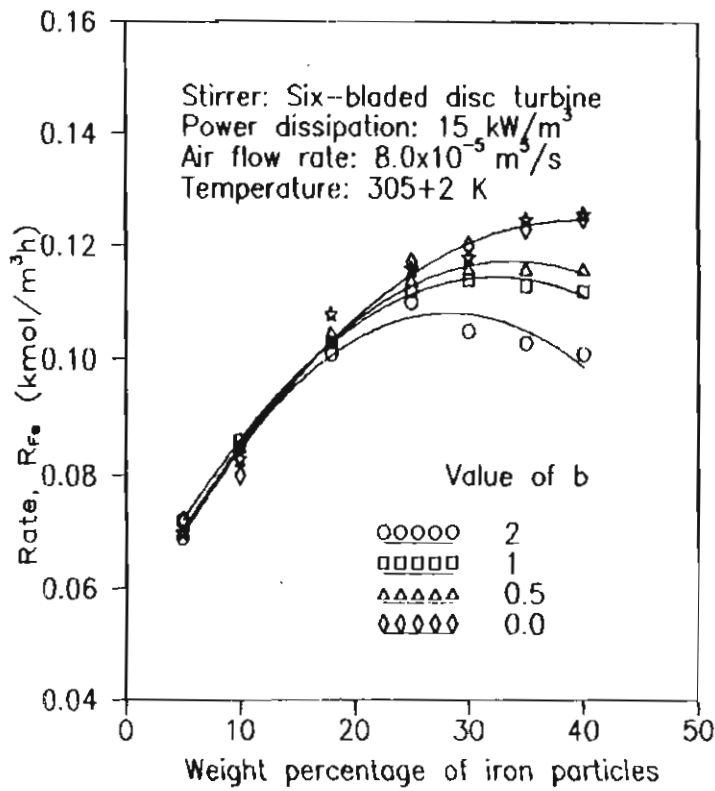
Fig.5.4. Comparison of experimentally obtained rates for various solid loadings and rates predicted by the model in which volumetric gas-liqid mass transfer coefficient is computed from the correlation $(k_{g}a_{g})_{s} = k_{g}a_{g}(1-b\phi)$.

5.4. Shift in the controlling mechanism with solid loading

Linear plots of C_1/R_{O_2}, versus a_s^{-1} are predicted by Eq.(5.11), derived from the model proposed in this work. A typical plot is shown in Fig.5.5. The y intercept y_0, represents the resistance to gas-liquid mass transfer $R_{gl} = 1/k_{gl}a_g$. At any point on this line $y - y_0$ gives the resistance to solid-liquid mass transfer $R_{sl} = 1/k_{sl}a_s$. For example, at a solid loading of 30% by weight ($a_s^{-1} = 5.5 \times 10^{-3}$ m), it is given by B' as 12.5 S. R_{gl} at both these points are given by A and B as 8 S. It is clear that, at high solid loading, R_{sl} is negligible compared to R_{gl}. This implies that, as the solid loading increases, the controlling step shifts progressively from solid-liquid mass transfer to gas-liquid mass transfer.

5.5. Discussion

Gas-liquid mass transfer at high solid loading

Interaction between solid particles and gas bubbles has been studied theoretically and experimentally by several investigators with relevance to flotation processes. The important factor characterising particle-bubble interaction is the Stokes number, given by,

$$Sk = \frac{1}{9} (\varrho_P/\varrho) (d_p/d_b)^2 Re_b. \qquad (5.14)$$

where ϱ_p and ϱ are densities of particle and liquid respectively, d_p and d_b diameters of particle and bubble, respectively, and Re_b is the bubble Reynold's number. For iron particles of 230 μm diameter, $Sk > 0.1$ and particle-bubble collision probability is high in this range (Finch and Dobby, 1990). Particle-bubble collision
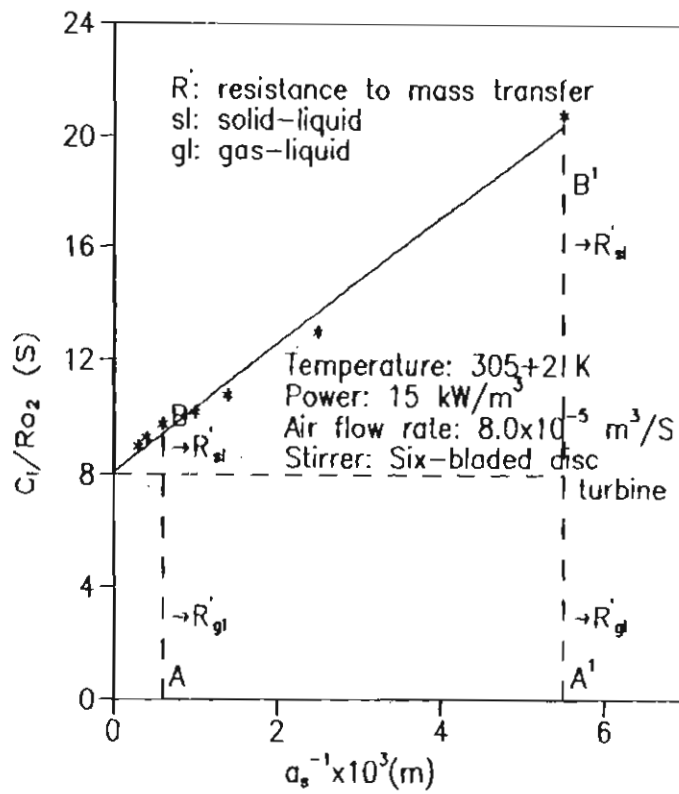
Fig.5.5. Plot of C_i/Ro_2 versus a_s^{-1}, showing the progressive shift in the controlling step from solid–liquid to gas–liquid mass transfer with solid loading.

is followed by a sliding motion of the particles over the bubble surface. Schulze (1994) have given a correlation for collision frequency in terms of energy dissipation rate and number of particles and bubbles.

In the present study, for an air flow rate of 8×10^5 m³/s and an energy dissipation rate of 10 kW/m³, average bubble diameter and the specific number of bubbles were computed from bubble diameter, gas hold-up and specific surface area of bubbles (Perry, 1984) as 3 mm and 1.6×10^7 m⁻³ respectively. For a particle loading of 20% by weight, the specific number of particles was computed as 6.73×10^9 m⁻³. Substituting these values in the correlation given by Schulze (1994), particle bubble collision frequency per bubble is obtained as 5.38×10^5 S⁻¹. This high frequency of collision indicates that liquid around the gas bubbles will be crowded with particles, as shown in Fig.5.6. This causes obstruction in the diffusion path and hinders the transfer of oxygen from gas-bubbles to the surrounding liquid. Negligible values of dissolved oxygen concentration in the bulk liquid phase at high active solid loading can be accounted for by this phenomenon. Since the particles are active, oxygen mass transfer takes place from the stagnant liquid surrounding bubbles to the surface of the particles. As a consequence, a very low dissolved oxygen concentration in the bulk liquid does not result in retardation in iron oxidation rates. A hypothetical concentration profile of oxygen for this condition is shown in Fig.5.6. Further investigations are required to understand fully this phenomenon of three-phase mass transfer under high active solid loadings.
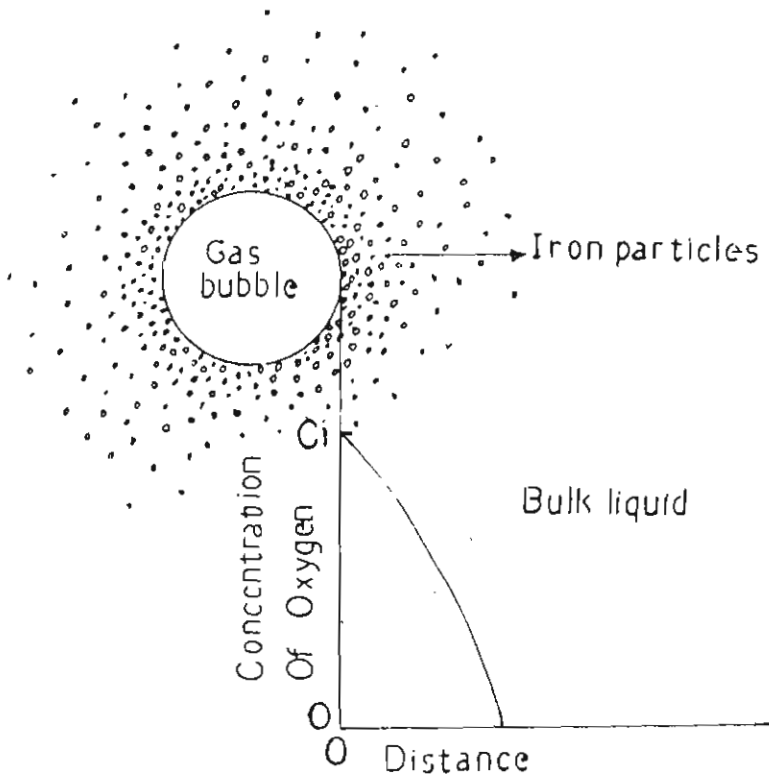
Fig.5.6. Concentration profile of oxygen at high active solid loading

Table 5.5. Comparison of experimental and predicted values of dissolved oxygen concentration in the bulk liquid phase

Iron particles (wt%)	power dissipation (kW/m³)	Air flow rate (m³/s×10³)	Experimental values of dissolved oxygen concentration, C_b (mg/l)	Predicted values of dissolved oxygen concentration, C_b (mg/l)
5	10	8	3.50	3.18
10	10	8	1.90	1.92
15	10	8	0.70	1.34
20	10	8	0.10	1.00
25	10	8	0.00	0.78
5	15	8	3.90	3.46
10	15	8	2.60	2.14
15	15	8	1.30	1.50
20	15	8	0.50	1.28
25	15	8	0.00	0.96

Variation in pH, oxidation reduction potential and ferrous ion concentration of the solution

Variation in pH, oxidation reduction potential and Fe^{2+} ion concentration with solid loading and partial pressure of oxygen during iron dissolution are given in Figs.5.7-5.11. The oxidation-reduction potential of a solution is given by the Nernst equation.

$$E = E_o + (2.3RT/nF) \log (Fe^{2+}/Fe^{3+}) \tag{5.15}$$

where E_o = the standard potential; F = Farady's constant; and n = the number of electrons transferred. The observed variations in oxidation-reduction potential and
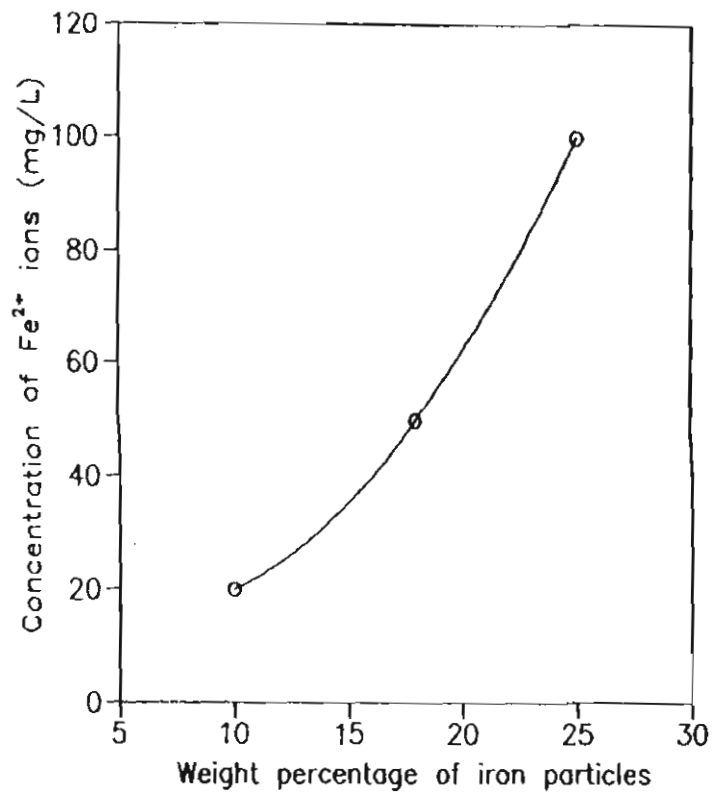
Fig.5.7. Variation in Fe^{2+} ion concentration with solid loading after 30 minutes of operation

92
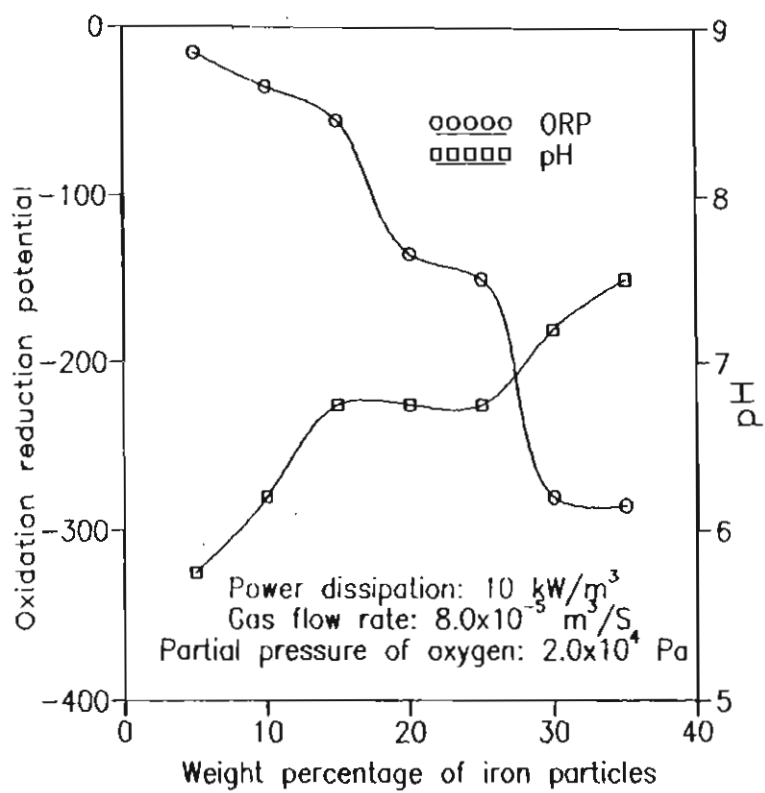
Fig.5.8. Variation in oxidation reduction potential and pH with solid loading after 30 minutes of operation.

93
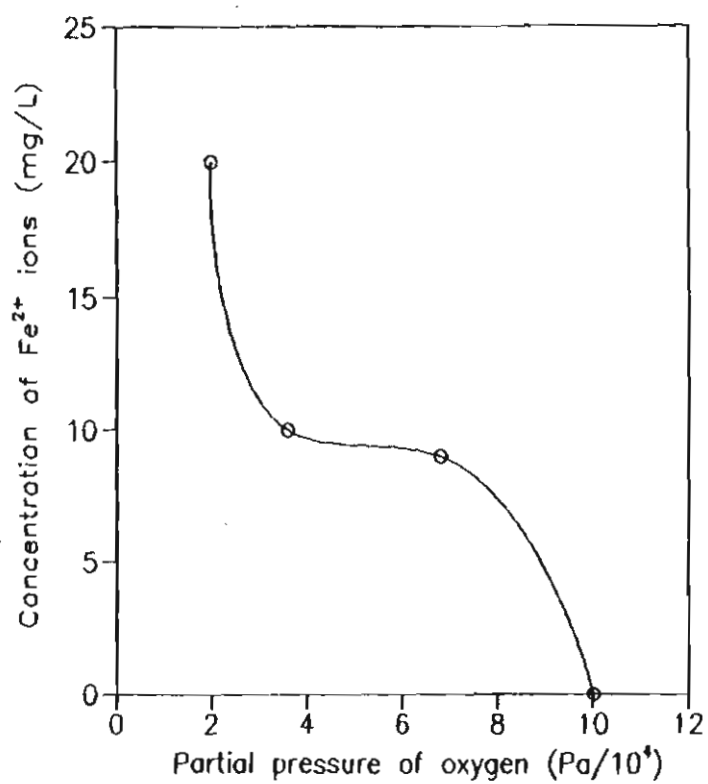
Fig. 5.9.   Variation in Fe^{2+} ion concentration with partial
pressure of oxygen after 30 minutes of operation.
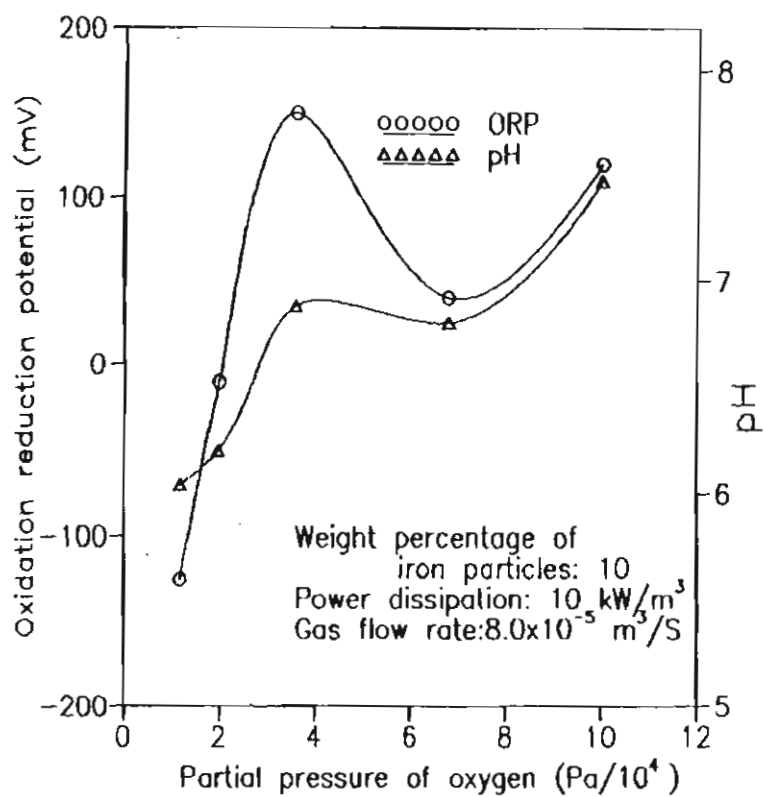
Fig. 5.10. Variation in oxidation reduction potential and pH with partial pressure of oxygen after 30 minutes of operation

95
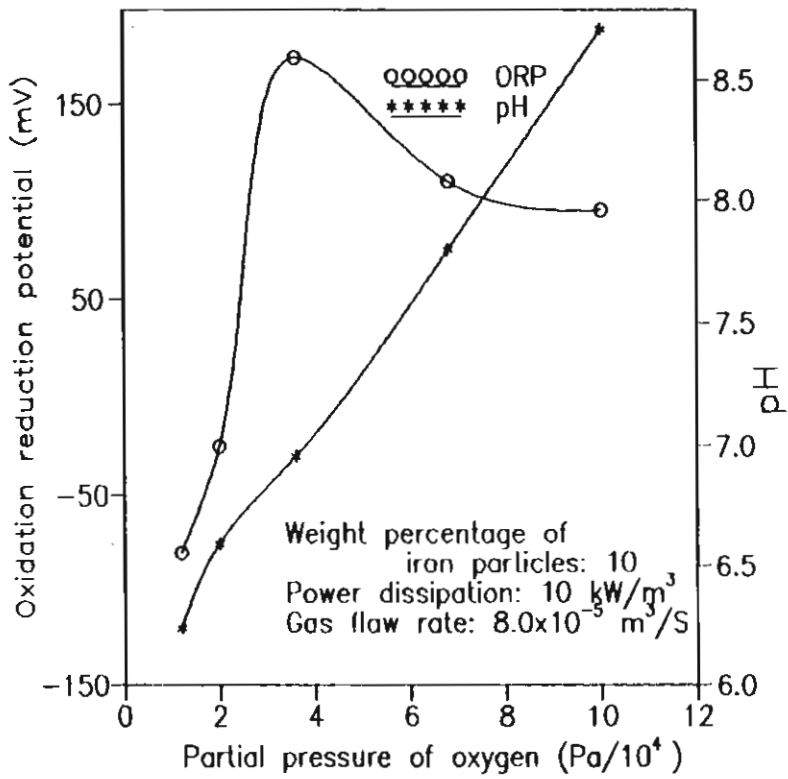
Fig.5.11. Variations oxidation reduction potential and pH with partial pressure of oxygen after 2 hours of operation.

Fe^{2+} ion concentration (Figs.5.7-5.10) are in accordance with the predictions of this equation.

It is observed that when solid loading varies, an increase in Fe^{2+} ion concentration (Fig.5.7) is followed by an increase in pH and a decrease in oxidation-reduction potential (Fig.5.8). When solid loading increases, the number of anodic sites present per unit volume of slurry increases and causes a higher concentration of Fe^{2+} ions in the solution resulting from anodic dissolution. Correspondingly, pH increases as a result of the higher concentration of OH^- ions generated, due to the cathodic reduction step given by Eq.(5.1b). However, when the partial pressure of oxygen increases, Fe^{2+} ion concentration becomes negligible (Fig.5.9) and an increase in pH is followed by an increase in oxidation-reduction potential (Fig.5.10). The various trends observed in the variation of pH with a variation in Fe^{2+} ion concentration and oxidation-reduction potential is due to the faster kinetics of homogeneous phase reaction at higher partial pressure of oxygen (greater than 2.03×10^4 Pa).

Effect of partial pressure of oxygen

The rate of oxidation of Fe^{2+} is proportional to the partial pressure of oxygen (Dreisinger and Peters, 1989). When the partial pressure of oxygen P_{O_2}, is greater than 2.03×10^4 Pa, the hydrolysis of Fe^{3+} ions is rapid (Blesa and Matijevic, 1989) (of the order of 10^2 S^{-1}) compared to Fe^{2+} oxidation, which becomes the controlling step. Under these conditions, the Fe^{3+} ion concentration will be negligible and the

97

oxidation-reduction potential assumes negative values. As the partial pressure of oxygen is increased, the oxidation-reduction potential becomes positive and Fe^{2+} ion concentration decreases (approaches zero at 1.0×10^5 Pa). As shown in Figs. 5.10 and 5.11, oxidation-reduction potential increases with partial pressure of oxygen upto about 3.65×10^4 Pa and then levels off. Under highly oxidising conditions (positive oxidation-reduction potential), the model is found not to be valid. The deviation of the observed iron removal rates from predicted values is shown in Fig.5.12. This can be attributed to passivation occurring at high oxidation potentials and high pH values (pH > 8).

5.6. Estimation of rate constant for ferrous oxidation reaction

In chloride solutions rate equation for ferrous oxidation reaction is of the form (Dreisinger and Peters, 1989).

$$R_{Fe2+} = k \, C_{Fe2+} \, C_b \, (C_{H+})^n \tag{5.16}$$

The value of n has been reported by various investigators as -0.25, -0.36 and -1. When the iron removal process is operated under steady state conditions, the rate of iron removal is equal to the rate of ferrous oxidation reaction. Hence, the rate of ferrous oxidation reaction was computed from the measured rate of iron removal under various conditions in this study. $C_{Fe2+}C_b C_{H+}^n$ was also computed from the measured values of C_{Fe2+}, C_b and pH. Plots of R_{Fe2+} versus $C_{Fe2+}C_b(C_H+)^n$ were drawn for the three values of n. The best linear plot (Fig.5.13) was obtained when n = -0.36 and k was estimated to be 2.16 $(mol/L)^{-1}S^{-1}$.
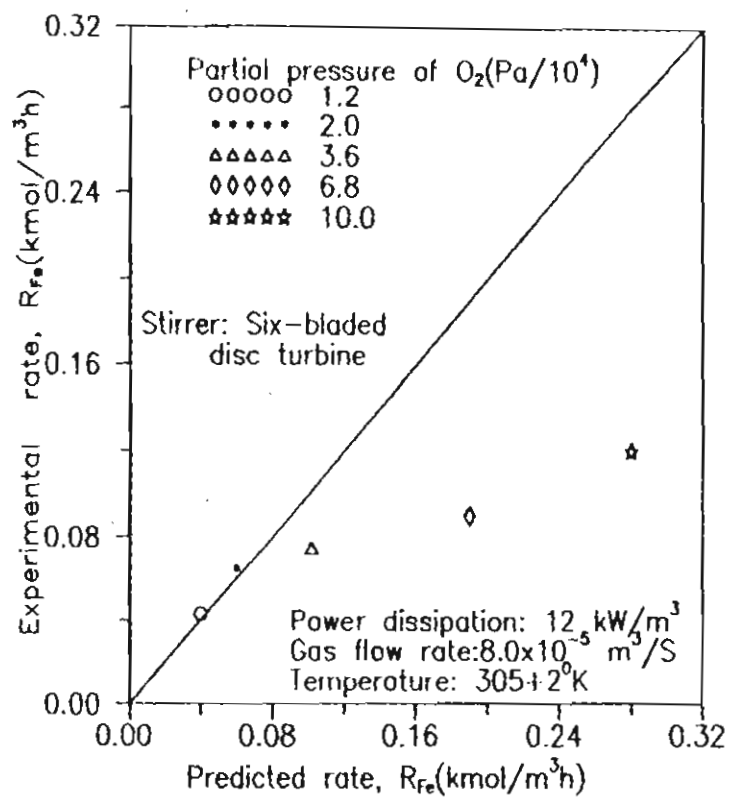
Fig. 5.12. Comparison of experimentally obtained rates with rates predicted by the model for various partial pressures of oxygen.

99
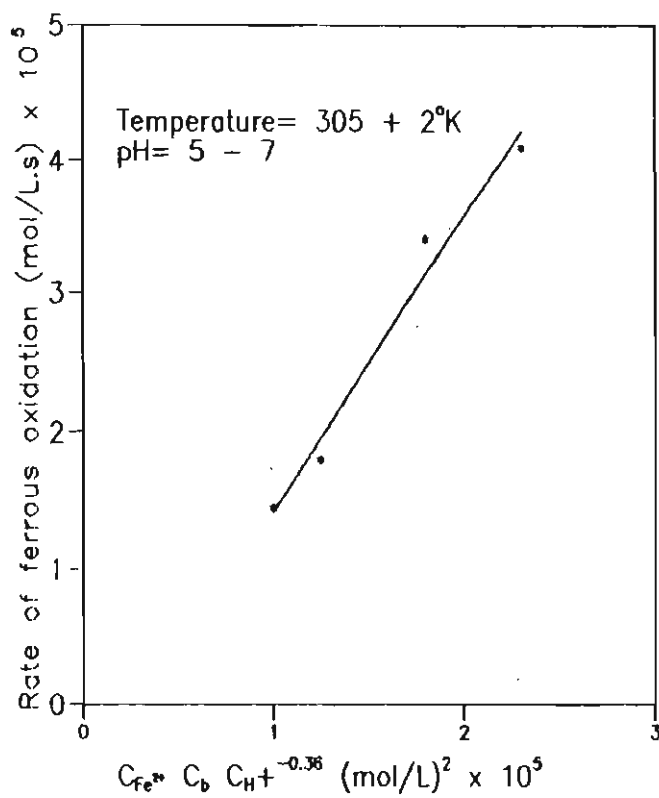
Fig.5.13. Linear plot of Fe^{2+} oxidation rate versus $C_{Fe^{2+}}C_bC_{H^+}^{-0.36}$

Conclusions

1. A steady state model for oxygen leaching process for iron removal in a mechanically agitated reactor has been proposed incorporating solid-liquid and gas-liquid mass transfer steps in series along with homogeneous phase oxidation of ferrous iron in the bulk liquid phase. The model has been validated for the initial linear phase of the overall process.

2. The rate of iron dissolution was insensitive to the loading of iron particles which is explained as being due to the solid particles acting as oxygen sinks inside an encapsulated shell around the bubble.

3. The rate parameters of ferrous oxidation reaction in the near neutral pH range have been estimated.

OXYGEN LEACHING PROCESS FOR IRON REMOVAL FROM A POROUS SOLID (REDUCED ILMENITE): MODELLING AND EXPERIMENTAL VALIDATION

This chapter describes a quantitative approach to predict the rate of iron removal due to oxygen leaching of a porous solid containing metallic iron. Reduced ilmenite obtained by high temperature reduction of ilmenite ore is used as the porous solid in this study. Besides, the iron removal from reduced ilmenite is a crucial unit process in the Becher process of synthetic rutile manufacture from ilmenite and has tremendous industrial significance. Taking into account the specific characteristics of reduced ilmenite, the model proposed in this chapter extends the earlier model proposed in Chapter V for a non-porous solid. Since the pore dimensions of reduced ilmenite ore is greater than the size of the precipitated iron oxide particles, the presence of an internal surface is likely to give rise to a much slower iron removal rate due to restricted oxygen diffusion into pores filled with iron oxide slurry than when the entire surface was external as in the non-porous solid.

6.1. Formulation of the Model

A model is developed for oxygen leaching process for iron removal from porous reduced ilmenite particles under non-isothermal conditions based on the following assumptions:

1   Liquid and gas phases are well mixed

2   The rate of electrochemical dissolution of iron is controlled by the oxyge mass transfer rate

3   The oxidation of ferrous irons is in the slow reaction regime

4   The rate of hydrolysis of Fe^{3+} ions is controlled by the rate of oxidation of Fe^{2+} ions in the bulk liquid phase

5   Ferrous ions neither hydrolyse nor precipitate

6   Fe^{2+}-NH_3 complex formation and dissociation reactions are instantaneous

7   The diffusion of Fe^{2+}-NH_3 complex from the reacting surface to the bulk liquid is very fast and is controlled by the diffusion of oxygen to the reactin surface

8   Heat loss through the walls of the reactor is negligible compared to the loss due to air sparging

Assumptions 1 to 5 are same as those employed in the earlier model (Chapter V) and have been already explained. The remaining assumptions are to be justified by the predictability of the model.

Temperature and humidity of the oxygen depleted air

From the measured wet bulb and dry bulb temperatures, the oxygen depleted air leaving the reacting slurry was found to be saturated and in thermal equilibrium with the slurry in the reactor.

103
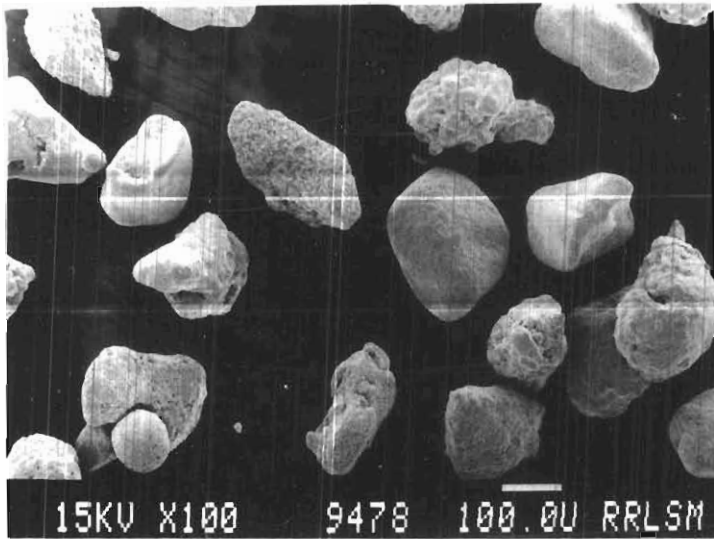
SEM photograph of reduced
ilmenite particles
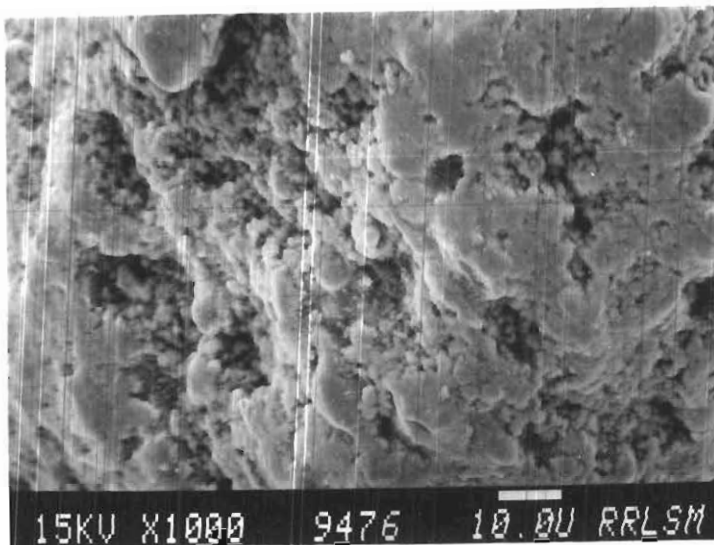
SEM photograph of the surface of
reduced ilmenite

Distribution of metallic iron in reduced ilmenite and the mode of dissolution

The metallic iron is dispersed on the external surface as well as in the pores of reduced ilemnite and constitutes only 23% of the total material. Since the electrochemical dissolution of iron is controlled by oxygen mass transfer rate, dissolution from the pores will occur after dissolution from the external surface. Orth and Liddel (1986) have reported increase in surface area during the initial period of acid leaching of ilmenite particles. As evident from the SEM photographs of reduced ilmenite particles, the surface is not at all smooth but contains projecting globules and inner lowered surfaces. During dissolution some of the occluded surface will be opened leading to increase in surface area. The measured surface area and pore volumes of reduced ilmenite before and after reaction (Table 6.1) is also in accordance with this fact.

Table 6.1. Specific surface area and pore volume of reduced ilmenite

Particle size, μm	Specific surface area, m²/gm		Pore volume, cm³/gm	
	Before reaction	After reaction	Before reaction	After reaction
+150 -180	1.1463	3.1012	$3x9x10^{-4}$	$1.5x10^{-3}$
+210 -250	0.6636	2.2981	$2.0x10^{-4}$	$1.3x10^{-3}$

Hence the dissolution of metallic iron from reduced ilmenite is suggested to be as follows:

(a) At time, $t = 0$, the active surface area is a fraction of the total external surface area

(b) As dissolution proceeds, more active sites are opened, i.e., a linear increase in active surface area occurs from a conversion $x = x_1$

(c) As dissolution proceeds further, the external deposit of iron gradually depletes, i.e., a linear decrease in active surface area occurs from a conversion $x = x_2$

(d) When the external deposit of iron gets exhausted, iron dissolution starts from the pores. When the conversion $x = x_3$, iron dissolution follows shrinking core model controlled by diffusion of oxygen through the pores filled by iron oxide-slurry

Material balance in the liquid phase

Taking oxygen balance over the bulk liquid volume,

$$V \cdot \frac{dC_b}{dt} = V \left[k_{gl} a_g \ (C_i - C_b) - k_{sl} a_s \ (C_b - C_s) - R_{O_{2,h}} \right] \qquad (6.1)$$

where $R_{O_{2,h}}$ is the rate of reaction of oxygen through the homogeneous phase Fe^{2+} oxidation reaction (Eq.5.3(b)). Rate of this reaction is given by,

$$R_{Fe^{2+}} = k C_{Fe^{2+}} C_b \ C_H^m \qquad (6.2)$$

where m varies from 0 to 1.

From the stoichiometry of reaction (5.3(b))

$$R_{O_{2,b}} = \frac{1}{4} R_{Fe^{2+}} \tag{6.3}$$

$$= \frac{1}{4} k \, C_{Fe^{2+}} \, C_b \, C_{H^+}^m$$

From Eqs.(6.1) and (6.3)

$$V . \frac{dC_b}{dt} = V \left[k_{gl} a_g \, (C_i - C_b) - k_{sl} a_s \, (C_b - C_s) - \frac{1}{4} k C_{Fe^{2+}} C_b C_{H^+}^m \right] \tag{6.4}$$

By Fe^{2+} ion balance over the bulk liquid volume V,

$$\frac{dC_{Fe^{2+}}}{dt} = V \left[2k_{sl} a_s \, (C_b - C_s) - k C_{Fe^{2+}} C_b . C_{H^+}^m \right] \tag{6.5}$$

Rate of transfer of OH ions to the bulk liquid by reaction (5.1(b))

$$= 4 k_{sl} a_s \, (C_b - C_s)$$

H^+ ions are produced by the hydrolysis of Fe^{3+} ions. It is assumed that hydrolysis reaction is very fast and hence it is controlled by the rate of Fe^{2+} oxidation reaction.

Therefore, rate of hydrolysis of Fe^{3+} ions = rate of Fe^{2+} oxidation

$$= k C_b C_{Fe^{2+}} C_{H^+}^m$$

According to the oxalation mechanism of hydrolysis (Blesa and Matijevic, 1989) each Fe^{3+} ion produces $3H^+$ ions.

Hence, rate of production of H^+ ions through hydrolysis reaction

$$= 3kC_b C_{Fe^{2+}} C_{H^+}^m$$

Rate of consumption of H^+ ions by the reaction (5.3(b)) $= kC_b C_{Fe^{2+}} C_{H^+}^m$

The ionic product, $C_{H^+} . C_{OH^-}$ of a dilute aqueous solution is always 10^{-14} (Vogel, 1989).

$$C_{H^+} . C_{OH^-} = 10^{-14} \tag{6.6}$$

Let r_{H_2O} be the rate of consumption of H^+ and OH^- ions for the formation of H_2O molecules. The rate of accumulation of H^+ and OH^- ions over the bulk liquid volume, V is given by,

$$\frac{dC_{OH^-}}{dt} = 4k_{sl}a_s (C_b - C_s) - r_{H_2O} \tag{6.7}$$

$$\frac{dC_{H^+}}{dt} = 3kC_b C_{Fe^{2+}} C_{H^+}^m - kC_b C_{Fe^{2+}} C_{H^+}^m - r_{H_2O} \tag{6.8}$$

Eqs.(6.7) and (6.8) are combined to give

$$\frac{dC_{H^+}}{dt} = \frac{dC_{OH^-}}{dt} + 2kC_{Fe^{2+}} C_b C_{H^+}^m - 4k_{sl}a_s (C_b - C_s) \tag{6.9}$$

Rate of iron dissolution

Since the electrochemical dissolution of iron is controlled by oxygen mass transfer rate to the surface, the rate of iron removal at any point of time is given by,

$$- V_{sl} \frac{dC_{Fe}}{dt} = 2 \times V \times k_{sl}a_s (C_b - C_s) \tag{6.10}$$

Rate of formation of iron oxide

The overall leaching and precipitation can be represented as

$$4Fe + 3O_2 \rightarrow 2Fe_2O_3 \tag{6.11}$$

Therefore the rate of formation of Fe_2O_3 is given by,

$$V_{sl} \frac{dC_{Fe_2O_3}}{dt} = \frac{2}{3} Vk_{sl}a_s (C_i - C_b) \tag{6.12}$$

Variations in mass transfer coefficients due to the presence of precipitated iron oxide

The influence of inert micro-particles on solid-liquid mass transfer to active particles has already been investigated and explained in detail in Chapter 3. The correlation (Eq.3.7) was employed to compute the reduced solid-liquid mass transfer coefficients at various amounts of precipitated iron oxide during the process.

Eq.4.6 as well as reported correlations (Table 2.2) were employed to compute the reduced volumetric gas-liquid mass transfer coefficient so that the suitable correlation could be selected by the predictability of the model.

Particle reaction model

At time $t = 0$, active surface area $a_s = a_{so}$ $\tag{6.13}$

When the conversion $x = x_1$, a_s increases according to

$$a_s = a_{so} (1 + a_1(x - x_1)]; \, x > x1 \tag{6.14}$$

where a_1 is an empirical constant.

108

When $x = x_2$, a_s decreases according to

$$a_s = a_{s1} [1 - a_2(x - x_2)] \tag{6.15}$$

where a_{s1} is the value of a_s at $x = x_2$ and a_2 is an empirical constant. Variation of surface area with conversion is depicted in Fig.6.1(a).

At $x = x_3$, external deposit of iron exhausts and porous diffusion and reaction start. The reaction follows shrinking core model with porous diffusion control. This leads to development of oxygen concentration at the particle surface as shown in Fig.6.1(b).

Reduced ilmenite particle undergoing shrinking core reaction is illustrated in Fig.6.2(a). It is assumed that reduced ilmenite particle contains pores of conical shape. Consider a single pore as shown in Fig.6.2(b).

Internal surface area of the cone
$$= \pi R \sqrt{R^2 + h^2}$$

$$= \pi R \sqrt{R^2 + \left(R \cos\frac{\theta}{2} \right)^2}$$

$$= b_1 . \pi R^2 \tag{6.16}$$

where b_1 is a constant.

Let n be the number of conical pores in a reduced ilmenite particle, then total internal surface area in the particle is $n . b_1 . \pi R^2$.

Therefore, the specific internal surface area $= b_2 . \pi R^2 \tag{6.17}$

109
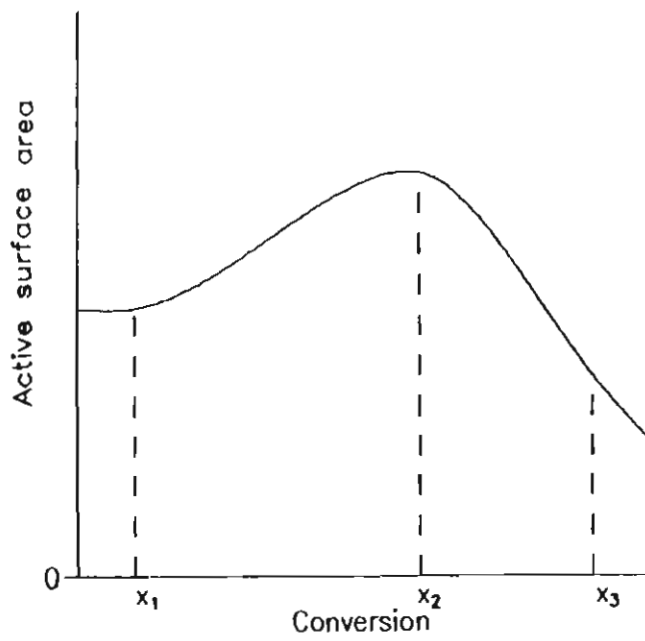
Fig.6.1.(a) Variation of active surface area of reduced ilmenite with conversion
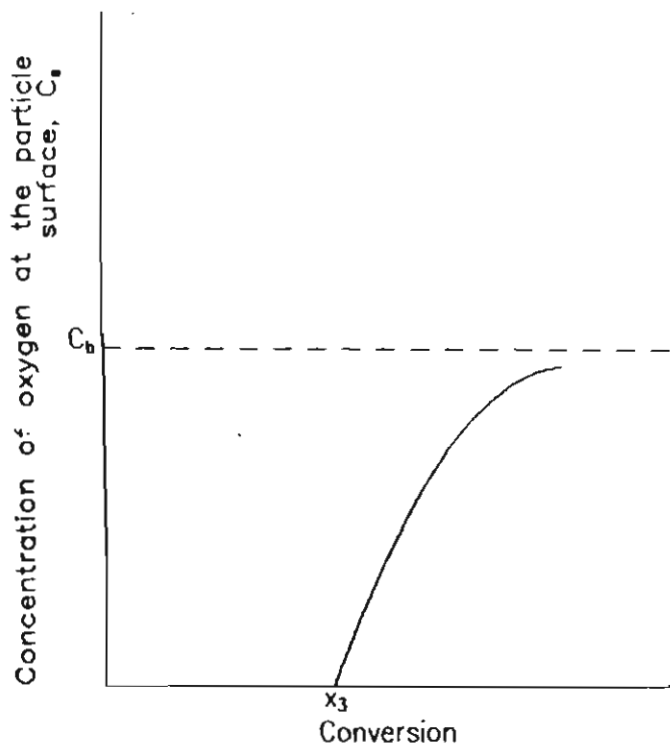
Fig.6.1 (b) Variation of concentration of oxygen at the external surface of reduced ilmenite particle with conversion.

110
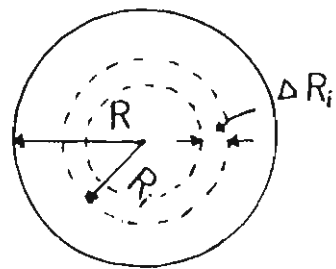
Fig.6.2(a) Illustration of shrinking core type reaction in porous
reduced ilmenite particle,
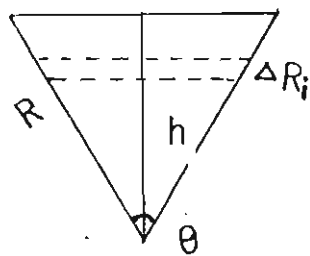
Fig.6.2(b) Illustration of a typical conical pore

where b_2 is a constant.

The constant b_2 can be evaluated by equating the measured specific internal surface area to $b_2 . \pi R^2$,

where $R = d_p/2.$ (6.18)

At any time t, the reacting surface area a_{si} is the surface area of the pores in the cone of thickness ΔR_i (Fig.6.2a). Then a_{si} is given by

$$a_{si} = b_2 . \pi [R_i^2 - (R_i - \Delta R_i)^2]$$ (6.19)

According to the shrinking core model,

$$X = \frac{\frac{4}{3}\pi R^3 - \frac{4}{3}\pi R_i^3}{\frac{4}{3}\pi R^3}$$ (6.20)

ie. $R_i = R(1 - x)^{1/3}$ (6.21)

Here the porous diffusion and hence the shrinking core type reaction starts from $x = x_3$. The normalized conversion X is given by

$$X = x - x_3.$$ (6.22)

Therefore, $R_i = R(1 - X)^{1/3}$ (6.23)

When porous diffusion starts, concentration of oxygen at the external surface of reduced ilmenite develops as shown in Fig.6.1(b).

112

Take oxygen balance at the surface of the particle,

$$\frac{dC_s}{dt} = k_{sl}a_s \ (C_b - C_s) - {}_{n_{si}}(C_s - O) \ \frac{D_{es}}{R - R_i} \qquad (6.24)$$

where D_{es} is the effective diffusivity of oxygen in the pores.

Heat Balance

Taking heat balance over the reactor volume,

$$\left[W_T \ (C_p)_{il} + V \ . \ d_w \ (C_p)_w \right] \frac{dT}{dt} = [\text{enthalpy of entering air - enthalpy}$$

of leaving air $+ \frac{dC_{Fe}}{dt} \ V \ \Delta H_r \ ] \qquad (6.25)$

Enthalpy of air in the range 30 to 70°C (Mcabe, 1976) is given by

$$H_p = 3.09 \times 10^{-7} e^{0.064T} \text{ kcal/kg.} \qquad (6.26)$$

Heat of reaction, ΔH_r for the formation of Fe_2O_3 from Fe is given by Becher *et al.* (1965) as 112 k.cal/mole. Specific heat of ilmenite is 0.15 k.cal/kg. °K (Touloukin and Byco, 1970).

Variation of solution properties with temperature

Solution viscosity, oxygen solubility and diffusivity of oxygen varies with temperature.

The solubility of oxygen or saturation concentration of oxygen in water C_i is given by the Henry's law,

$$C_i = HP_i \qquad (6.27)$$

where H is the Henry's law constant and P_i is the partial pressure of oxygen.

113

Variation of Henry law constant with temperature is reported by Harvery (1996) by the relationship,

$$\ln H = \ln P^s - 9.4/T* + 4.5(1-T*)^{0.355} / T* + 11.34 \exp(1-T*) (T*)^{-0.41}$$

$$(6.28)$$

where P^s is the vapour pressure, $T*$ is the reduced temperature T/Tc and Tc is the critical temperature 647.14 °K.

From the prediction of Anilkumar Patwardhan (1986), vapour pressure of 0.1 M NH_4Cl is same as that of pure water.

The correlation of Ping Han and David (1996) can be taken for the prediction of temperature dependence of oxygen diffusivity in water:

$$\log_{10} [D/cm^2 s^{-1}] = -4.410 + 773.8/T - (506.4/T)^2 \qquad (6.29)$$

The viscosity data of water in the range 30 to 70°C taken from Perry (1984) follows the following linear relationship,

$$\mu \, (Pa.S) = 8 \times 10^{-4} - (T - 303) \times 10^{-5} \qquad (6.30)$$

Variation of mass transfer coefficients with temperature

Variation of solid-liquid mass transfer coefficient k_{sl} and volumetric gas-liquid mass transfer coefficient $k_{gl}a_g$ results from the variations of liquid viscosity and oxygen diffusivity. These variations were accounted for in the correlations for respective mass transfer coefficients.

114

Variation of Fe²⁺ oxidation rate with temperature

The effect of temperature on Fe^{2+} oxidation rate is given by the Arhenius equation

$$k = k_o e^{-E/RT} \qquad (6.31)$$

The activation energy E for this reaction has been estimated by various investigators to be in the range 50 to 80 KJ/mol (Iwai *et al.* , 1979; Iwai and Hiroshi Majima, 1979).

6.2. Experimental

The experimental set up used was the same as described in Section 5.2. The reduced ilmenite was prepared from raw ilmenite taken from Chavara beach sands by roasting with coal at 1050°C in a rotary kiln.

The ranges of process parameters studied are given in Table 6.2.

Table 6.2. Ranges of process variables

Parameter	Unit	Range
Power dissipation, e	kW/m³	12
Gas flow rate, qg	m³/g	1x10⁻⁴
Weight percentage of reduced ilmenite, W	-	-
Particle size, d_p	μm	+100-150, +150-+180, +200-250
Partial pressure of oxygen, P_{O_2}	Pa	
Temperature, T	K	303-325

Characteristics of Reduced ilmenite

Particle size: The reduced ilmenite prepared in the laboratory contained particles in the size range 60 to 300 μm. The three size ranges employed for carrying out the experimental investigations are +100 -150 μm, +15 0 -180 μm and +210 - 250 μm.

Iron content: Chemical analysis showed the total iron content of the reduced ilmenite as 28.5% and metallic iron content as 23%.

Specific surface area: Specific surface area measurements were done in BET apparatus. The reduced ilmenite samples were degassed at 200°C for 4 hr prior to the measurement. Specific surface area and pore volumes for different particle sizes were obtained (Table 6.1).

The agitator speeds for suspension of reduced ilmenite particles under various solid loadings and air flow rates were determined using the Zwictering criterion (the particles remain at the tank bottom for less than 1 sec). The suspension speeds thus determined are given in Table 6.3. During experimentation on the kinetics of the process, agitator speed was kept at 12 rev/s which is above the suspension speeds for all the experimental conditions. Reduced ilmenite samples were drawn at one hour intervals during the process. The drawn samples were repeatedly washed with water to remove iron oxide particles, washed with acetone and dried. pH, temperature and oxidation reduction potential were measured using the on-line measurement set up described in Section 5.2. The

Table 6.3. Minimum agitator speeds for suspension of reduced ilmenite particles (+210 - 250 mm), N_c

Weight percentage of reduced ilmenite	Air flow rate (m³/s)					
	Six-bladed disc turbine			Downward pumping axial flo turbine		
	0	1×10^{-4}	2×10^{-4}	0	1×10^{-4}	2×10^{-4}
10	5.83	6.67	6.80	6.67	6.67	7.50
20	5.83	6.67	7.5	6.67	7.5	8.33
30	6.67	8.33	9.17	7.5	9.16	10.00
40	7.92	9.17	10.00	8.33	10.00	11.67

chemical analysis for determining the total iron content of the reduced ilmenite samples was carried out as follows:

0.5 gm of the reduced ilmenite sample was fused with 10 gm potassium bisulphate in a silica crucible at 900°C for half an hour. The fused concentrate was cooled and dissolved in 20% sulphuric acid solution by boiling. The solution was cooled and made up to 250 ml. 20 ml was pipetted out and heated to 60°C with 5 ml concentrated HCl. $SnCl_2$ was added to this hot solution drop by drop till the yellow colour disappears in order to reduce the ferric ion content to ferrous state. The solution was cooled. 15 ml saturated mercuric chloride, 15 ml acid mixture and 15 ml Zimmerman solution were added and titrated against standard potassium dichromate solution using sodium diphenylamine indicator. From the titre value, the total iron content of the sample was calculated.

6.3. Experimental Results and Model Validation

Conversion versus time plots for various particle sizes and solid loadings, both under isothermal and non-isothermal conditions are given in Figs. 6.3 to 6.6. A linear relationship between the conversion (% removal of iron) and time is observed throughout the 7 hours operation for 30% solid loading, whereas for the solid loadings for 20% and 10%, the slope decreases towards the end. During adiabatic operation, temperature rises from the beginning and attains a maximum value within 3 hours and then remains steady or slowly decreases (Figs.6.7 and 6.8). As shown in Fig.6.9, there is an increase in pH at the beginning and then decreases till the end of the process. Oxidation in reduction potential is negative for most of the time and exhibit a tendency to fluctuate (Fig.6.10).

The developed model equations are first order linear differential equations and were solved numerically using fourth order Runge Kutta method with adaptive step size control. Inputs to the model are energy dissipation rate, air flow rate, solid loading, average particle size of reduced ilmenite and partial pressure of oxygen. Predicted conversion, temperature and pH for various solid loadings and particle sizes are compared with experimental values in Figs.6.3 to 6.9 and are in reasonable agreement.

Estimation of empirical constants in Eqs.6.13 to 6.15

Prediction of the initial rate for various conditions showed close agreement with experimental values when the active surface area forms 0.25 fraction of the

118
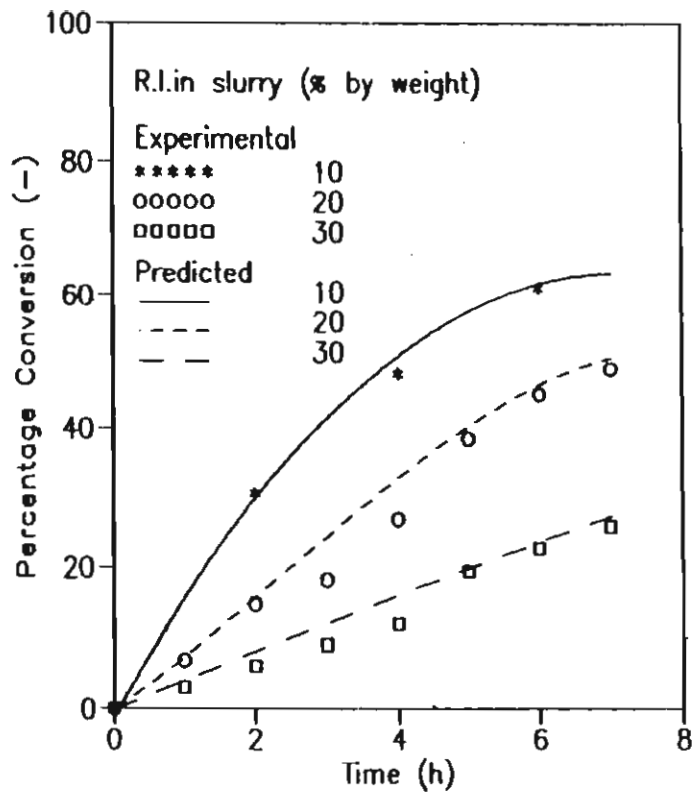
Fig.6.3. Conversion versus time plots for various loadings of reduced ilmenite— model validation. Non isothermal operation. Particle size = +210–250 μm, Air flow rate= 1x10^{-4} m^3/s Electrolyte concentration= 0.1M NH$_4$Cl

119
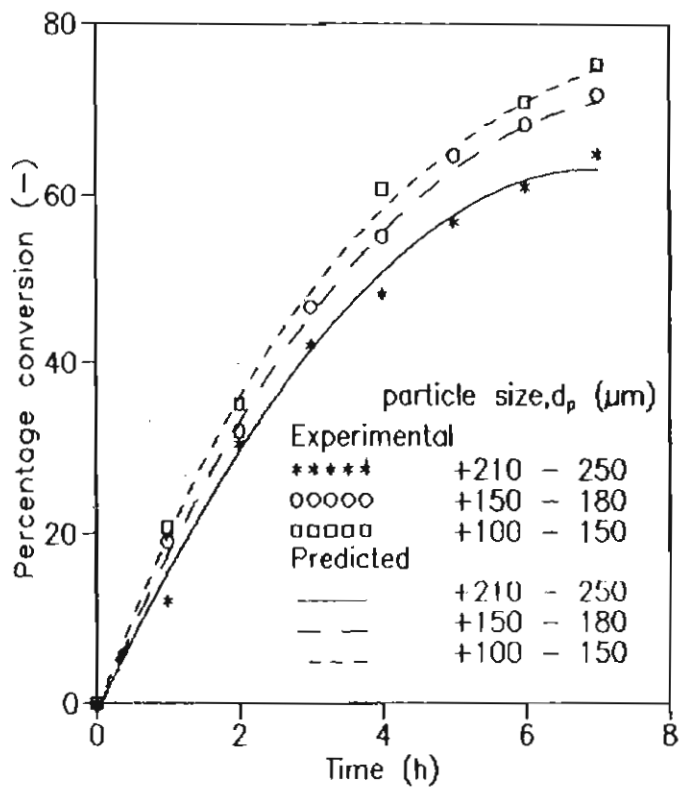
Fig.6.4. Conversion versus time plots for various particle sizes —
model validation. Non isothermal operation. Reduced ilmenite
in slurry= 10% by weight, air flow rate= 1 X 10^{-4} m^3/s
electrolyte concentration= 0.1M NH_4Cl
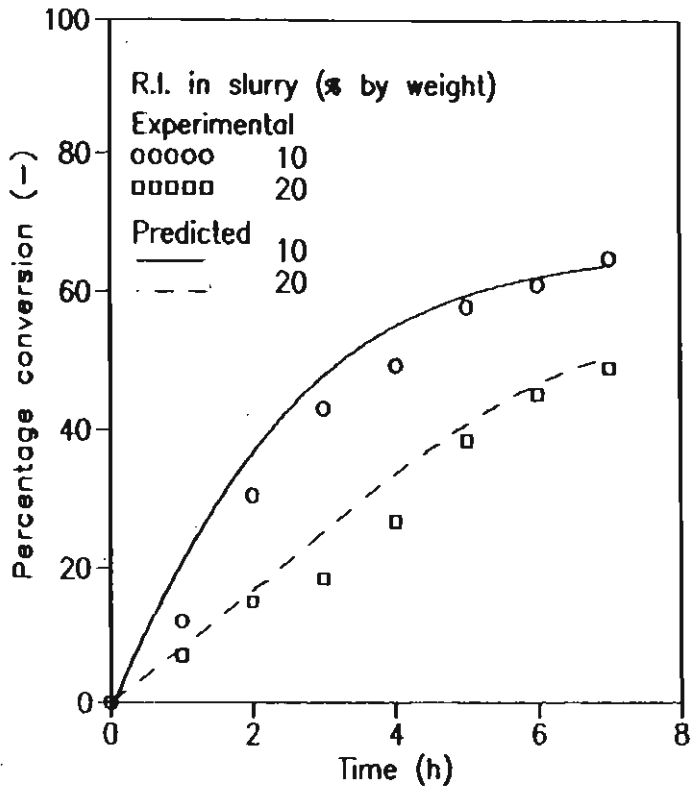
Fig.6.5. Experimental and predicted conversions during isothermal operation at 30°C. Particle size= +210 – 250 um. Air flow rate= 1x10^{-4} m^3/s. Electctrolyte concentration= 0.1M NH$_4$Cl
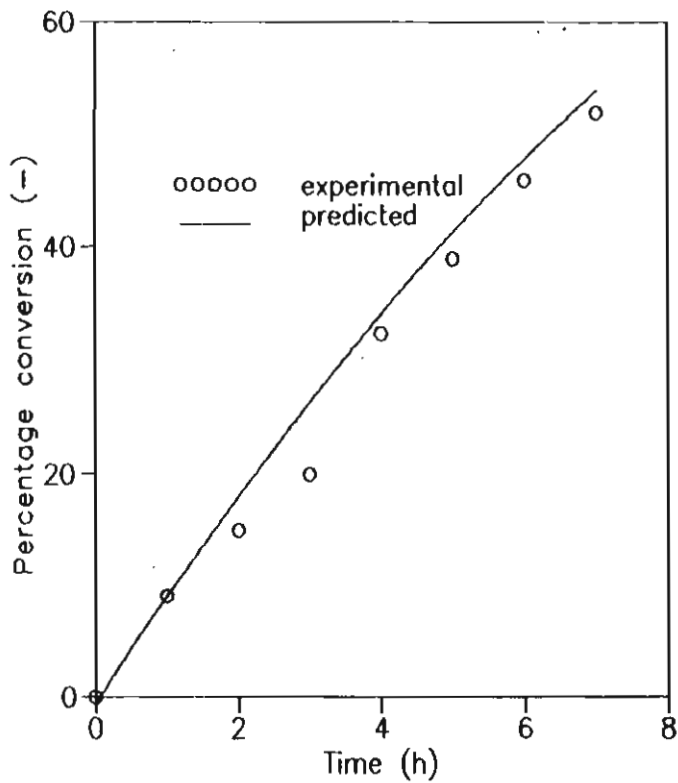
Fig.6.6. Experimental and predicted conversions during iso-
thermal operation at 50°C. R.I. in slurry= 20 % by weight
Particle size= +150–180 μm. Air flow rate= 1x10^{-4} m^3/s
Electrolyte concentration= 0.1M NH$_4$Cl

122
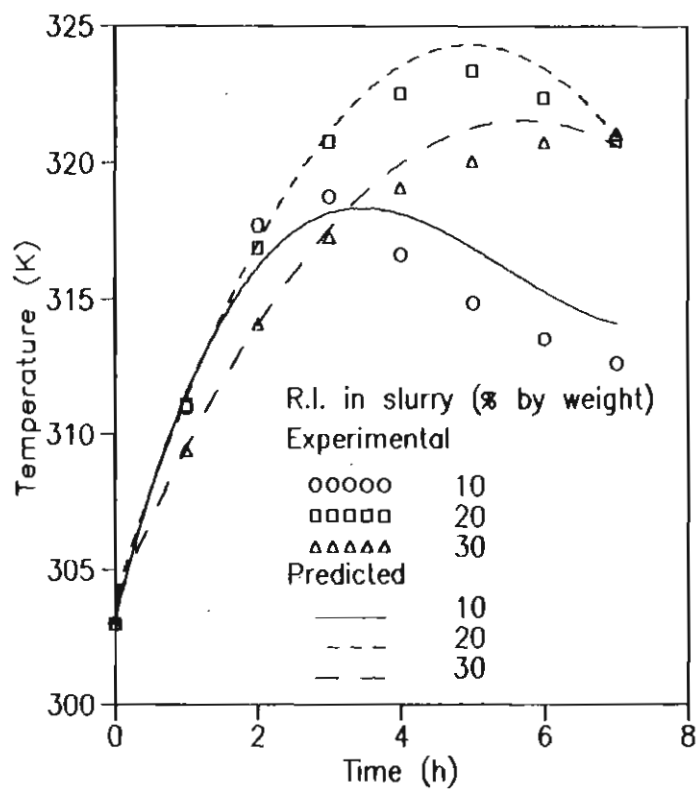
Fig.6.7. Observed and predicted variations in temperature during non-isothermal operation for various solid loadings. Particle size= +210−250 μm. Air flow rate= 1x10^{-4} m^3/s Electrolyte concentration= 0.1M NH$_4$Cl
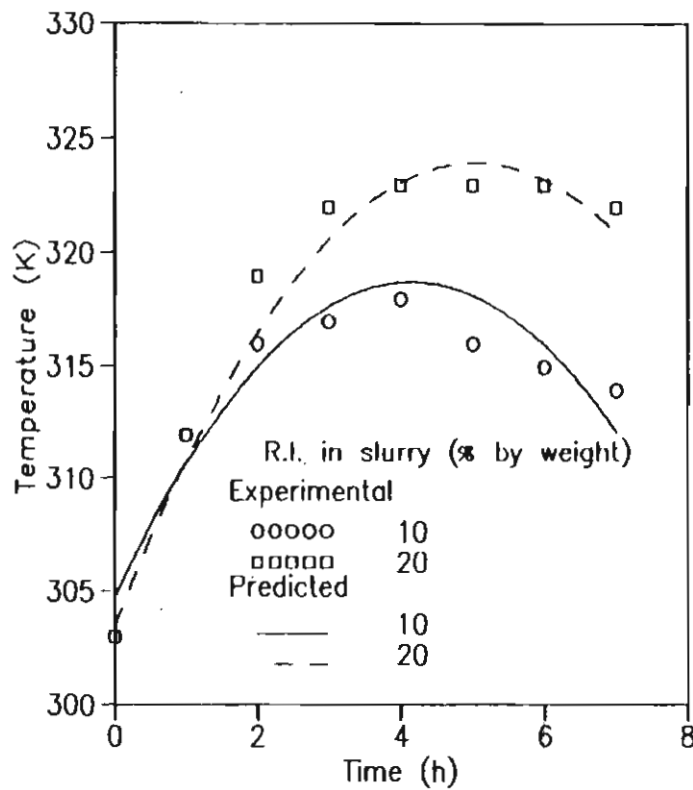
Fig.6.8. Observed and predicted variations in temperature during non-isothermal operation for various solid loadings. Particle size= +150-180 μm. Air flow rate= 1x10^{-4}m^3/s Electrolyte concentration= 0.1M NH$_4$Cl

124
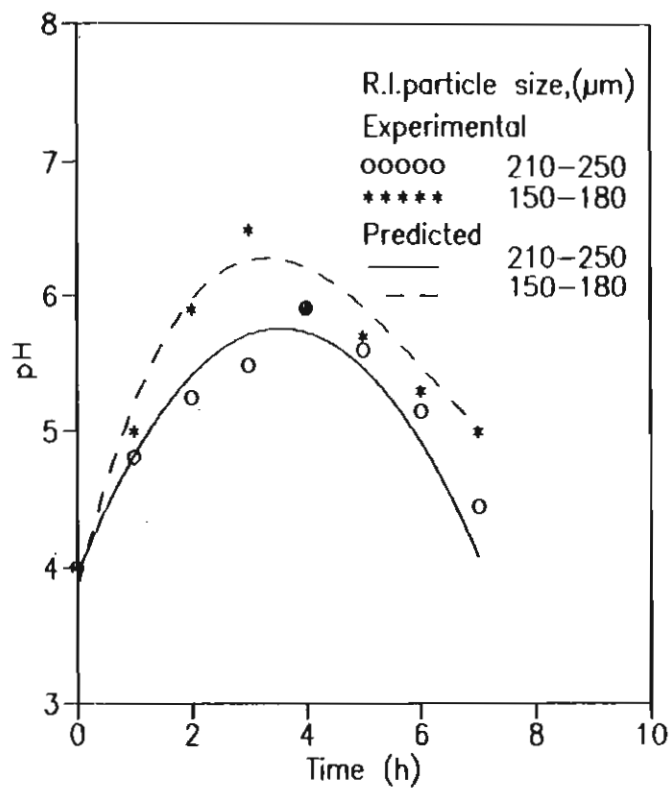
Fig.6.9. Observed and predicted variations in pH during non-isothermal operation, R.I.in slurry= 10 % by weight. Air flow rate= 1 x 10^{-4} m^3/s. Electrolyte concentration=0.1M NH$_4$Cl
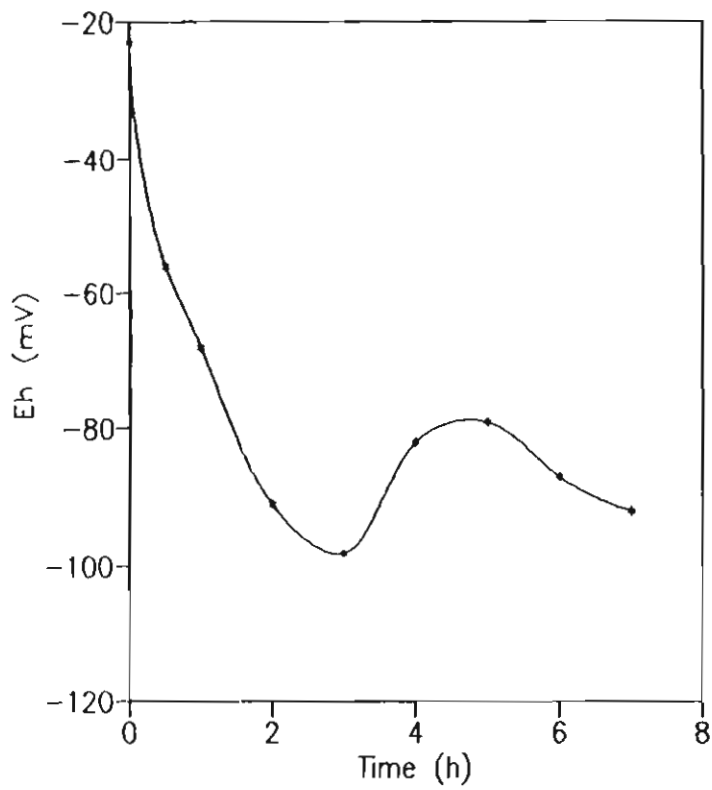
Fig.6.10. Variation of oxidation reduction potential.Non−isothermal operation. Air flow rate=$1 \times 10^{-4} m^3/s$. R.I.in slurry=20% by weight Particle size=+210−250μm. Electrolyte concentration=0.1M NH_4Cl.

126

total external surface area. This finding is reasonable since metallic iron constitutes only around 25% of the reduced ilmenite by weight.

Variation in iron dissolution rate as a result of variation in mass transfer coefficients or surface area induces changes in liquid phase concentrations of Fe^{2+} ions, H^+ ions and OH^- ions, resulting in the variation of pH. Hence constants a_1 and a_2 in eqs.6.14 and 6.15 were estimated such that the predicted pH and conversion closely matches with experimental values for various conditions. The conversion levels x_1 and x_2 were also determined in the same manner. The estimated values of parameters and conversion levels are

$$a_1 = 5 \times 10^{-4} \qquad a_2 = 3 \times 10^{-3}$$

$$x_1 = 0.13 \qquad x_2 = 0.29$$

Estimation of conversion x_3

According to the assumption of mass transfer controlled electrochemical dissolution of iron, iron dissolves from the pores only after the complete dissolution of external deposite of iron. The observed decrease in iron removal rate starts from the point which corresponds to the onset of porous diffusion and reaction. In a typical plot of conversion versus time slope of the cu ‿‿eases drastically from this point. From the various experimental plots versus time, this conversion was obtained as 0.4.

127

Influence of the precipitated fine iron oxide particles on mass transfer rates

One important aspect which is not considered in other multiphase leaching models but encountered in the present model is the influence of the precipitated fine solid phase on mass transfer rates.

Influence on solid-liquid mass transfer

Earlier work reported in Chapter III clearly brought out the fact that inert microparticles reduce the solid-liquid mass transfer rate to coarse active particles in a mechanically agitated contactor. The expression obtained from this study (Eq.3.7) was employed to compute the reduction in solid-liquid mass transfer rate caused by precipitated fine iron oxide particles during the iron removal process. However, since the process was controlled by gas-liquid mass transfer under the conditions studied (solid loading > 10% by weight of reduced ilmenite), reduction in solid-liquid mass transfer coefficient due to inert micro-particles hardly induced any change in the predicted conversion.

Influence on gas-liquid mass transfer

Influence of inert micro-particles on gas-liquid mass transfer has also been studied (Chapter IV). Eq.4.6 was employed to compte the reduced volumetric gas-liquid mass transfer coefficient. However, upto a conversion of 0.4, from where the porous diffusion starts, the amount of iron oxide formed is so small (less than 2% by weight) that there is not any considerable retardation effect.

6.4. Effect of added iron oxide on the rate of iron removal

Additional experiments were carried out to investigate the effect of fine iron oxide particles on the overall rate of iron removal by adding various amounts of iron oxide to the system. The iron oxide used for this study was collected from earlier experiments carried out on iron removal process. The collected iron oxide was washed for a number of time to get free of reduced ilmenite particles, and then dried. The characteristics of the iron oxide thus prepared were

(a) Characteristics of iron oxide

Mean particle size   =   1.69 μm

Specific surfaced area =   7.4109 m²/cc

Density   =   5240 kg/m³

The process carried out with a mixture of reduced ilmenite and iron oxide in a small agitated reactor set up, the details of which are given in Section 3.2. Experimental parameters investigated are listed in Table 6.4. The process was

Table 6.4. Range of process variables studied during the kinetic slurry in the presence of added iron oxide

Parameter	Unit	Range
Power dissipation, ε	kW/m³	22
Air flow rate, q_g	m³/S	3×10^{-5}
Weight percentage of reduced ilmenite, W	-	5
Range of particle size of reduced ilmenite, d_{mp}	μm	+210 -250
Weight percentage of iron oxide	-	1,3,6 and 10
Average particle size of iron oxide, d_{mp}	μm	1.06
Temperature, T	K	303±2

carried out for 2 hours and the rates were followed by drawing reduced ilmenite samples at definite intervals and carrying out the total iron analysis as explained in Section 6.2.

Enhancement in iron removal rate in the presence of added iron oxide

Conversion versus time plots for various amounts of added iron oxide are depicted in Fig.6.11. An enhancement in iron removal rate, to a maximum of 1.5 times that obtained in normal iron removal process is clearly evident.

The observed phenomena is in accordance with the reported fact (Speller, 1951) that iron oxide particles could enhance corrosion rates by getting reduced at the cathodic sites through the mechanism

$$Fe^{3+} + e^- \rightarrow Fe^{2+}$$
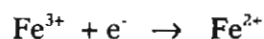
This reduced iron oxide particles will again get oxidised in the presence of oxygen. Hence, during the iron removal process, iron oxide particles get reduced at the cathodic sites on the reduced ilmenite particles, go to the bubble surface and get oxidised, then again go back to the particle surface. The observed enhancement in iron removal rate can be attributed to this shuttling mechanism of iron oxide-particles.

However, the iron oxide particles can enhance the iron removal rate as long as the dissolution takes place from the external surface of the reduced ilmenite particles. The amount of iron oxide formed during this period is so small
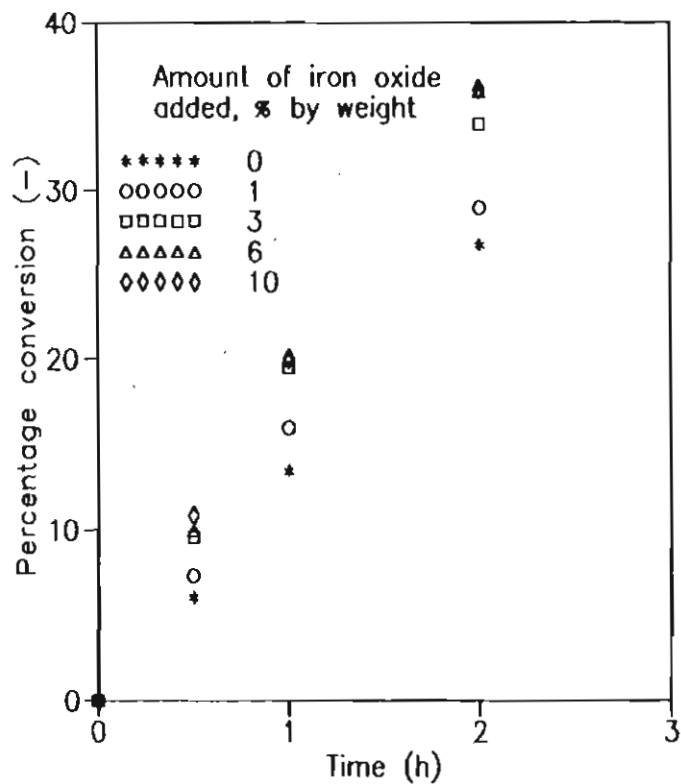
Fig.6.11. Conversion versus time plots showing enhancement in iron removal rate inthe presence of added iron oxide. Non isothermal operation. R.I.in slurry= 10 % by weight. Air flow rate= 3×10^{-5} m^3/s. Electrolyte concentration=0.1M NH$_4$Cl

(less than 2% by weight) that there is not any considerable enhancement due to the shuttling mechanism.

6.5. The active-passive transition

It is evident from Fig.6.3 that conversion decreases with solid loading, according to model predictions as well as experimental investigation. However, when the oxygen leaching process was carried out with 5% by weight of reduced ilmenite, it was observed that the conversion is even less than that obtained with 10% by weight. This phenomena could be explained as due to the active-passive transition of electro-chemical reaction as follows:

When the potential of a metal exceeds that corresponding to equilibrium between the metal and one of its oxides $(E_M/E_{M_2O_3})$, the appropriate oxide or hydroxide should form on the metal surface. It is because such a film frequently tends to confer protection and slow down dissolution to aquo-ions that a metal in this condition is said to be passive. Depending on the pH of the solution the onset of passivation on iron metal occurs at potentials in the range 0 to 0.3 V (Shreir, 1994). The anodic potential during electrochemical corrosion can be computed from Eq.(2.17) if the corrosion current $i_a = i_c$ is known. Since the electrochemical dissolution of iron during the oxygen leaching process is controlled by diffusion of oxygen, the corrosion current can be computed from the rate of diffusion of oxygen to the particle surface. The computed anodic potentials for various loadings of reduced ilmenite are listed in Table 6.5, which shows that the potential tends to be positive as the solid loading becomes less than 10% by weight, thus

132

leading to passivation. Similarly, higher partial pressures of oxygen also lead to passivation (Table 6.6).

Table 6.5. Computed anodic potentials at various loadings of reduced ilmenite in volts d_p = +210 -250 μm, q_g = 1x10^{-4} m^3/S)

Reduced ilmenite in slurry (% by weight)	Symmetry factor α_a = 0.5	Symmetry factor α_a = 0.97
5	-0.410	0.06
10	-0.44	0.04
20	-0.428	-0.01
30	-0.429	-1.15

Table 6.6. Computed anodic potentials at various partial pressures of oxygen (volts) d_p = +210 -250 μm, q_g = 1x10^{-4} m^3/S, W = 10% by weight

Partial pressure of oxygen (Pa x 10^5)	Symmetry factor α_a = 0.5	Symmetry factor α_a = 0.97
2.44	-0.426	0.06
4.06	-0.39	0.10
7.31	-0.385	0.12
13.80	-0.383	0.13
20.30	-0.382	0.14

6.6. Conclusions

1. Steady state model proposed for the non-porous iron particles has been extended to predict the rate, temperature and pH during the unsteady state and non-isothermal leaching of porous reduced ilmenite particles.

2. The model considers dissolution of iron from the external surface and from the pores of reduced as two series steps, i.e., iron dissolution starts from the pores only after the complete dissolution from the pores.

3. The sluggish kinetics towards the end of the process is due to the high resistance to the diffusion of oxygen through the pores.

INVESTIGATIONS ON PROCESS INTENSIFICATION BY ENHANCEMENT IN OXYGEN MASS TRANSFER RATES

Since the iron removal by oxygen leaching process is controlled by oxygen mass transfer, especially by the gas liquid mass transfer at higher solid loading, improved iron removal rate can be obtained only through an enhancement in gas-liquid mass transfer rate. However, it has been shown in Section 6.5 that higher oxygen mass transfer rate to the solid surface will lead to higher anodic potentials resulting in passivation and 'in situ rusting'. Hence the optimum strategy to obtain improved iron removal rate can only be the enhancement in gas-liquid mass transfer and at the same time, providing an alternate route for the cathodic reduction step not involving oxygen. This has been achieved by carrying out the process in $FeCl_2$ solutions in concentration ranging from 0.05 N to 0.25 N. Experimental investigations on the rate enhancement process and interpretation of the results based on the classical theory of gas-liquid reactions form the theme of this Chapter.

7.1. Experimental

Experimental equipment and process parameters studied were the same as described in Section 6.2. Various electrolyte concentrations used were:

135

0.1 M NH_4Cl and 0.25 M $FeCl_2$

0.1 M NH_4Cl and 0.2 M $FeCl_2$

0.1 M NH_4Cl and 0.1 M $FeCl_2$

0.1 M NH_4Cl and 0.05 M $FeCl_2$

0.1 M $FeCl_2$

0.25 M FeCl

0.1 M NH_4Cl and 0.5 M HCl

During the 7 hours operation reduced ilmenite samples were drawn at one hour intervals and total iron analysis was carried out as explained in Section 6.2. pH, temperature and oxidation reduction potential of the reacting slurry were monitered. Slurry samples were also withdrawn for determining Fe^{2+} ion concentration. The slurry was filtered and Fe^{2+} ion concentration of the filtered solution was determined by titration against potassium dichromate solution.

7.2. Results

Conversion versus time plots given in Fig.7.1 clearly show that the presence of $FeCl_2$ in the solution produces enhancement in iron removal rate. When the concentration of $FeCl_2$ is above 0.1 M, enhancement is almost same. Fig.7.2 shows the conversion versus time plots for various concentrations of electrolyte concentrations. It is evident that when $FeCl_2$ concentration is above 0.1 M, iron removal rate is independent of the presence of NH_4Cl. Fig.7.3 depicts the variation of iron removal rate with particle size in 0.25 M $FeCl_2$ solution. A

136
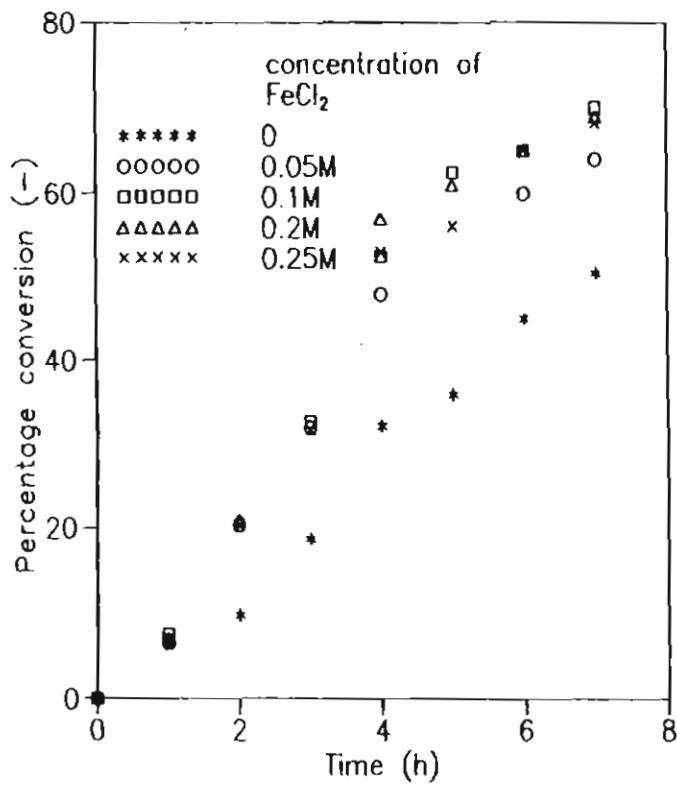
Fig.7.1. Conversion versus time plots showing enhancement in iron removal rate in the presence of $FeCl_2$. Non–isothermal operation. R.I. in slurry= 20% by weight, air flow rate= $1 \times 10^{-4} m^3/s$. Particle size=+210–250μm.Electrolyte concentration= 0.1M NH4Cl and $FeCl_2$

137
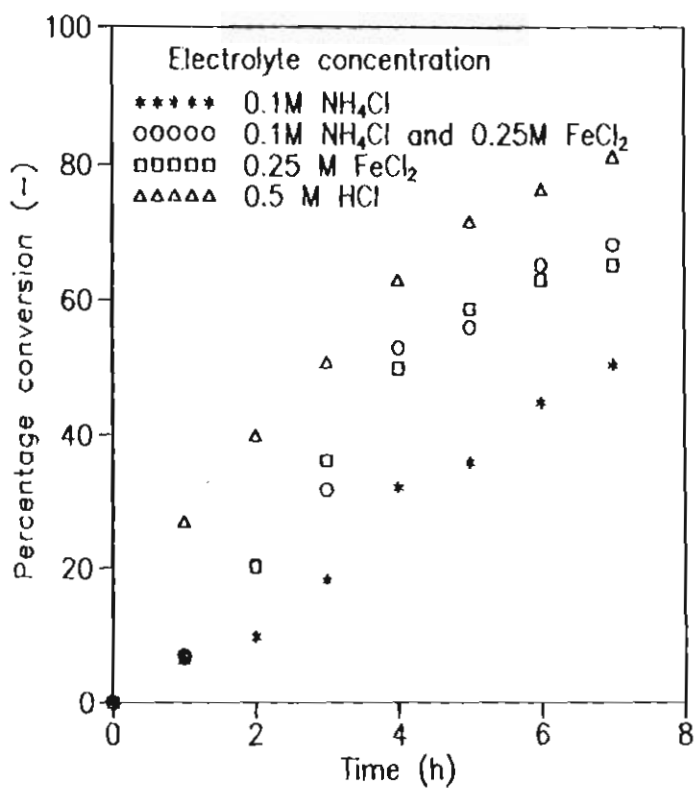
Fig.7.2. Conversion versus time plots for various combinations of electrolyte concentrations. Non-isothermal operation. Particle size= +210-250μm. R.I.in slurry=20% by weight.Air flow rate=1x10^{-4}m^{3}/s
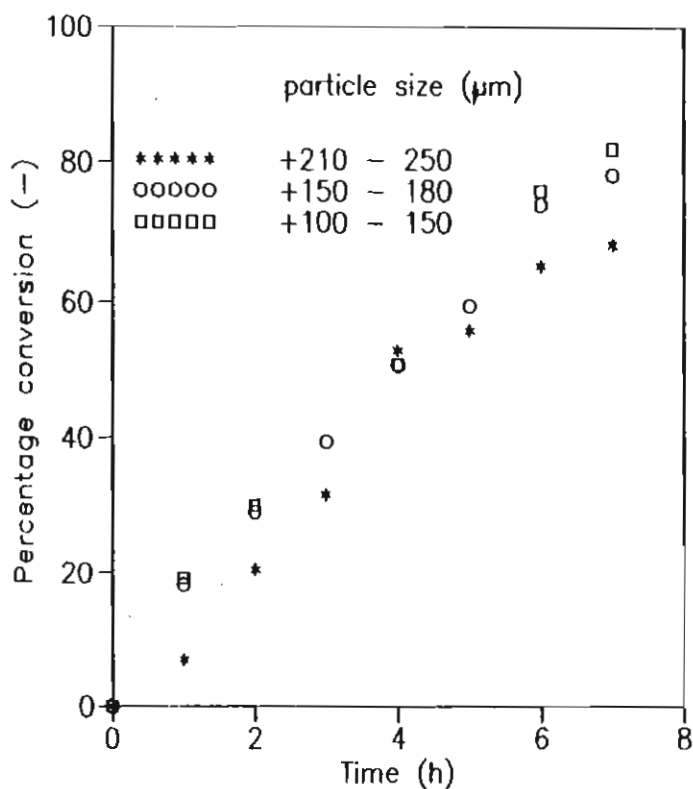
Fig.7.3. Variation of conversion with particle size in $FeCl_2$ solution. Non—isothermal operation. R.I. in slurry = 20% by weight. Airflow rate= $1 \times 10^{-4} m^3/s$. Electrolyte concentraion= 0.1M NH_4Cl and 0.25M $FeCl_2$

139

peak conversion of 85% was obtained within 7 hours for the particles in the size range -150 + 100 μm. Towards the end of the process, where the reaction is controlled by porous diffusion, conversion increases with decrease in particle size.

Variation of solution properties

During this improved iron removal process, the temperature profile was same as in the normal iron removal process. The pH of the solution remained acidic throughout the process, starting from a pH around 3 and stabilizing near a pH 6, as shown in Fig.7.4. Throughout the process, Fe^{2+} concentration remained close to the starting value, as shown in Table 7.1. In contrast to ammoniacal oxygen leaching, the oxidation reduction potential always remained positive.

Table 7.1. Measured Fe^{2+} ion concentration during iron removal process carried out using $FeCl_2$ solution (moles/L)

R.I. in slurry (% by weight)	Particle size of R.I. (μm)	Initial concentration of $FeCl_2$ in the solution (moles/L)			
		0.05	0.1	0.2	0.25
10	-180 +150				0.18 to 0.16
	-250 +210				0.18 to 0.15
20	-150 +100				0.23 to 0.21
	-180 +150		0.08 to 0.06		0.23 to 0.2
	-250 +210	0.05 to 0.04	0.08 to 0.06	0.2 to 0.16	0.2 to 0.18
30	-250 +210				0.18 to 0.14
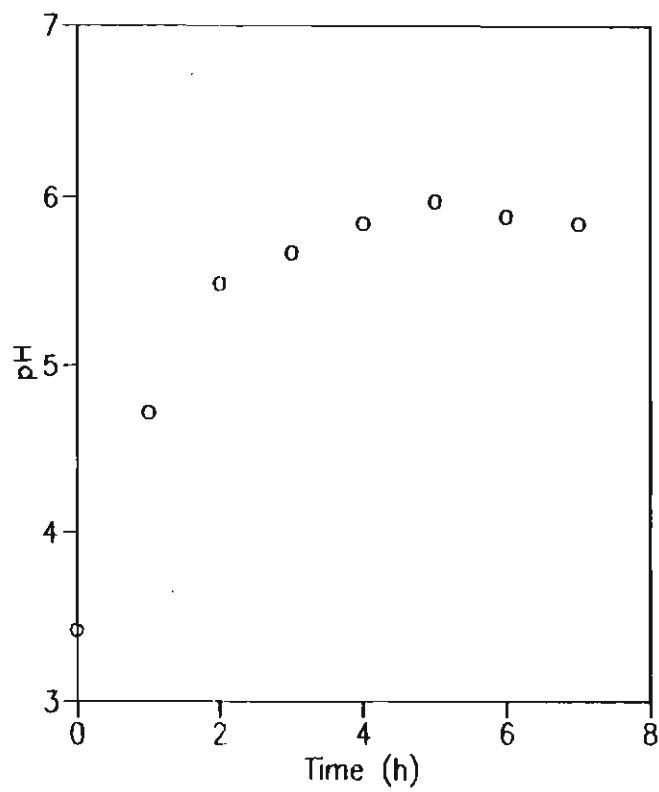
Fig.7.4. Atypical plot showing variation of pH during the iron removal process in 0.25M FeCl$_2$ solution

7.3. Interpretation of Enhancement in Iron removal rate

Enhancement in gas-liquid mass transfer rate as a result of higher concentrationn of Fe^{2+} ions in the solution is attributed to the observed increase in iron removal rate. Gas-liquid mass transfer enhancement occurs when the homogeneous phase reaction is in the fast reaction regime and hence the reaction takes place in the gas-liquid film (Charpentier, 1981). Criteria for the reaction regime is given by the Hatta number, Ha

$$Ha = (D_A k C_{Bo})^{1/2} / k_{gl} \qquad (7.1)$$

where D_A is the diffusivity of the diffusing gas and C_{Bo} is the concentration of the liquid phase reactant.

The criteria are,

$0.02 < Ha < 0.3,$ slow reaction regime

$0.3 < Ha < 3,$ moderately fast reaction regime

The reaction takes place in the bulk liquid phase when it is in the slow reaction regime. When the reaction is in the fast reaction regime, part of the reaction takes place in the gas-liquid film and hence induces an enhancement in gas transfer across the gas-liquid boundary. The enhancement factor, E is defined as

$$R_{gl} = E k_{gl} C_{Ai} \qquad (7.2)$$

where R_g is the rate of gas transfer

142

Enhancement factor E is given by Charpentier (1981) as

$$E = \frac{Ha \, [(E_i - E) / (E_i - 1)]^{1/2}}{\tan h \left\{ Ha \, [(E_i - E) / (E_i - 1)]^{1/2} \right\}} \tag{7.3}$$

where $E = 1 + (D_B/zD_A) (C_{Bo}/C_{Ai})$ (7.4)

From the above discussion, it follows that depending on the Fe^{2+} concentration in the liquid phase, Fe^{2+} oxidation reaction can be in the slow or fast reaction regime. Hatta number and enhancement factors computed for various Fe^{2+} concentrations are listed in Table 7.2. Hatta numbers for Fe^{2+} concentrations

Table 7.2. Computed values of Hatta number and enhancement factors
corresponding to various Fe^{2+} concentrations

Concentration of Fe^{2+} $C_{Fe}2+$ (moles/L)	Hatta number Ha	Enhancement factor E
1×10^{-3}	0.09	-
5×10^{-2}	0.6	1.17
0.10	0.9	1.25
0.20	1.27	1.48
0.25	1.42	1.7

of 0.05 M and above corresponds to fast reaction regime. This means that all the experimentally investigated $FeCl_2$ concentrations correspond to fast reaction regime of Fe^{2+} oxidation reaction. 1×10^{-3} M Fe^{2+} concentration corresponds to a

typical case where the solution contains NH_4Cl as the only electrolyte. Hatta number corresponding to this concentration is in the slow reaction regime.

Alternate cathodic reaction mechanism

When the Fe^{2+} oxidation reaction is in the fast reaction regime, the liquid phase concentration of oxygen will be almost zero and hence only negligible amount of oxygen will be transferred to the surface of reduced ilmenite particles. In this case, reduction of oxygen (Eq.5.1b) cannot be the only cathodic reaction. A possible mechanism in higher concentrations of Fe^{3+} ions is reduction of Fe^{3+} ions, viz.

$$Fe^{3+} + e^- \quad \rightarrow \quad Fe^{2+} \tag{7.5}$$

The Fe^{2+} ions will again be oxidised in the gas-liquid film. Whatever be the independent mechanism, the overall iron removal reaction is represented by Eq.(6.11), and hence the rate of iron removal is proportional to the total amount of oxygen transferred to the liquid phase. Consequently the net result of enhancement in gas-liquid mass transfer is an enhancement in iron removal rate.

Comparison of predicted and observed iron removal rates

In the conventional ordinary iron removal process carried out in 0.1 M NH_4Cl solution, the liquid phase concentration of oxygen is almost zero at high solid loading (say 30% by weight). Then gas-liquid mass transfer rate is given by

$$R_g = k_{gl}C_i \tag{7.6}$$

144

Therefore, according to the definition of enhancement factor, (E.7.2), the enhanced gas-liquid mass transfer rate in $FeCl_2$ solutions can be obtained by multiplying the gas-liquid mass transfer rate in NH_4Cl solution with the calculated enhancement factor E. Hence, the iron removal rate for 30% by weight of reduced ilmenite in 0.25 M $FeCl_2$ solution can be obtained, by multiplying the gas-liquid mass transfer rate with the corresponding enhancement factor E. The observed and predicted conversions are in reasonable agreement (Fig.7.5).

7.4. Influence of added iron oxide on the rate of iron removal in $FeCl_2$ leaching

Experiments were carried out to investigate the effect of iron oxide particles on the kinetics of oxygen leaching in $FeCl_2$ solution, using the same materials and experimental procedure as described in Section 6.4. In contrast to the finding of enhancement of iron removal rate in conventional oxygen leaching, added iron oxide did not produce considerable change in the iron removal kinetics in $FeCl_2$ leaching (Fig.7.6). This could be due to the absence of cathodic oxygen reduction at the particle surface in $FeCl_2$ leaching, in which case iron oxide cannot have the role of 'shutling agent' as described in Section 6.4.

7.5. Conclusions

Enhancement in iron removal rate to a maximum of 150% was realized through the addition of $FeCl_2$ to the reacting solution. The role of $FeCl_2$ has been interpreted as to produce enhancement in gas-liquid mass transfer rate by shifting the ferrous oxidation reaction from a slow reaction regime to fast reaction regime.

145
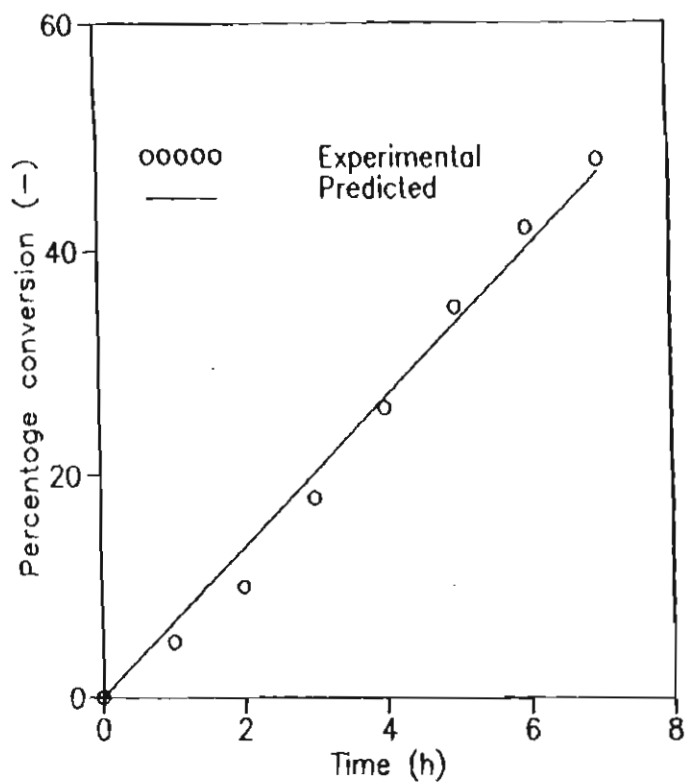
Fig.7.5. Experimental and predicted conversions in $FeCl_2$ solution at o solid loading of 30% by weight. Non-isothermal operation. Particle size=+210-250 μm. Air flow rate= 1×10^{-4} m^3/s Electrolyte concentration= 0.1M NH_4Cl and 0.25M $FeCl_2$

146
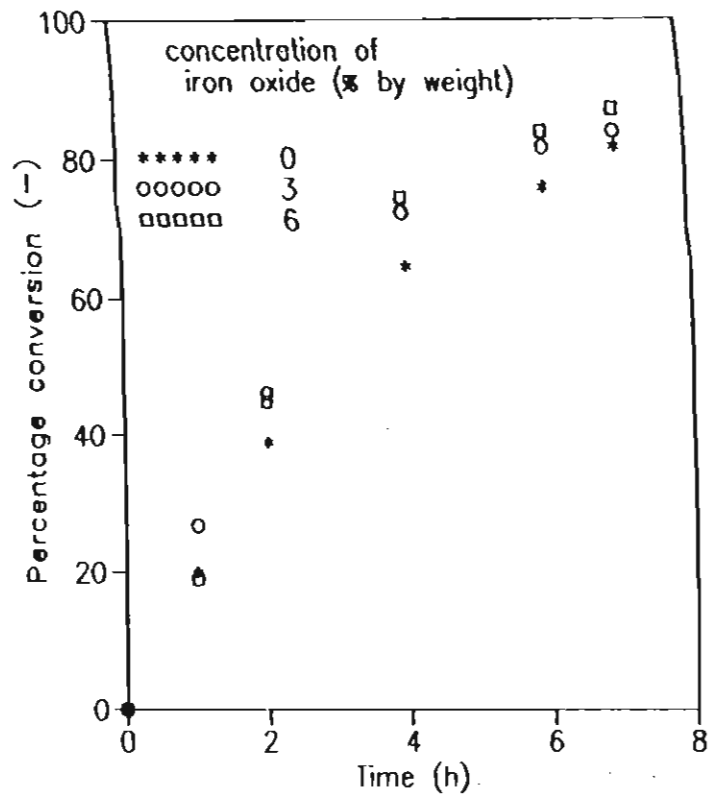
Fig.7.6. Conversion versus time plots showing the influence of added iron oxide in $FeCl_2$ leaching. Non-isothermal operation. R.I. in slurry= 10% by weight. Airflow rate= 1×10^{-4} m^2/s Electrolyte concentration= 0.25M $FeCl_2$

147

Chapter VIII

CONCLUSIONS

The oxygen leaching process for iron removal in a mechanically agitated reactor, being characterised by a multiphase system, is identified to involve the following constituent steps or sub-processes:

1) Gas-liquid oxygen mass transfer

2) Solid-liquid mass transfer

3) Electrochemical dissolution of iron at the solid surface (heterogeneous phase reaction)

4) Ferrous oxidation in the bulk liquid phase (homogeneous phase reaction)

5) Hydrolysis of ferrous irons and subsequent precipitation as iron oxides

From a literature review on the above sub-processes, it become evident that for the development of a process model for the oxygen leaching process relevant to industrial conditions, experimental investigations and interpretations have to be carried out on the following aspects.

- influence of inert micro-particles (precipitated iron oxide) on solid-liquid mass transfer to coarse active particles (ilmenite particles)

- gas-liquid mass transfer in the presence of two solid phases, namely, coarse (ilmenite) and fine (iron oxide) particles

- kinetics of ferrous oxidation reaction at near neutral pH conditions

The influence of inert micro-particles on solid-liquid mass transfer rate was studied separately under simulated conditions employing a system involving iron particles as coarse active particles and inert micro-particles of various sizes and densities. Solid-liquid mass transfer rate measurements were carried out using a novel technique, namely, the cementation reaction technique under controlled conditions. The presence of inert micro-particles induced significant reduction in solid-liquid mass transfer rate depending on the size, density and volume fraction. The results were interpreted in terms of mass transfer fouling in analogy with heat transfer fouling. Separate correlations were developed for mass transfer attenuation due to inert particles belonging to micron ($d_{mp} > 1$ μm) and sub-micron ($d_{mp} < 1$ μm) size ranges.

Gas-liquid mass transfer rate measurement were also carried out under simulated conditions. Gas-liquid mass transfer attenuation due to iron oxide and ilmenite particles were correlated in terms of volume fractions.

Experimental investigations on the kinetics of oxygen leaching process for iron removal from non-porous iron particles for an initial period of two hours at 30°C showed that it was a constant rate phase and the rate was controlled by oxygen mass transfer rate. As the solid loading increases, the controlling step shifts progressively from solid-liquid mass transfer to gas-liquid mass transfer. The results further indicate that the type of impeller does not make any perceptible difference to the overall kinetics, if the energy dissipation is constant. The developed steady state model having energy dissipation rate, air flow rate, particle

size and solid loading as input variables was validated by the experimental data. The rate of iron dissolution was insensitive to the loading of iron particles, which is explained as being due to the solid particles acting as oxygen sinks inside an encapsulated shell around the gas bubble. The observed variations in pH, oxidation reduction potential and Fe^{2+} ion concentration are consistent with the overall reaction mechanism proposed in this work.

The steady state model for non-porous iron particles was extended to predict the unsteady state kinetics of porous reduced ilmenite particles under non-isothermal conditions. The model considers iron dissolution from external surface and pores as two series steps: first iron dissolves from the external surface and then on completion dissolution starts from inside the pores. Conversion, temperature and pH predicted by the model is in reasonable agreement with the experimentally obtained values. The sluggish kinetics towards the end of the process is shown to be the result of high resistance due to oxygen diffusion through the pores filled with iron oxide slurry. Influence of iron oxide on the initial kinetics of overall process was found to be an enhancement in iron removal rate, which is explained as being due to a 'shuttling mechanism' of iron oxide particles.

Improved iron removal rate by about 150% was realized through the addition of $FeCl_2$ to the reacting solution, which produces enhancement in gas-liquid mass transfer rate by shifting the ferrous oxidation reaction from a slow reaction regime to fast reaction regime. The experimental data are quantitatively interpreted using the classical theory of mass transfer with chemical reaction.

150

Thus, in keeping with the objectives proposed in this work, a quantitative process model relevant to industrial process conditions for the iron removal step in the Becher process has been proposed and validated. More importantly, the model identifies the controlling step as the oxygen mass transfer step and using this as a novel way towards process intensification, has been demonstrated and quantitatively interpreted from classical theory of mass transfer enhancement in fast reaction regime.

REFERENCES

Agarwal, R.D., Journal of Mines, Metals and Fuels (1988) 138-143.

Agarwal, R.D., Mehta, M.L. and Kapoor, M.C., Indian Journal of Technology, 18 (1980) 317-324.

Anil Kumar and Patwardhan, V.S., Can. J. Chem. Engg., 64 (1986), 831-838.

Armanate P.M. and Donald J. Kirwan, Chem. Engg. Sci., 44 (1989) 2781-2796.

Asai S., Yasuhiro Konishi and Gakiyaru Sasaki, World Congress III of Chem. Engg. Tokyo (1986) 428-431.

Asai, S., Konishi, Y. and Kajiwara, T., J. Chem. Eng. Japan, 22 (1989) 96.

Bailey, A.D. and Hansfold, G.S., Minerals, Engg., 7 (1994) 293-303.

Baldwin S.A., Demopoulos G.P. and Papangelakis, V.G., Metallurgical and Materials Trans. B, 26B (1995) 1035-1047.

Beenackers, A.A.C.M. and Van Swaji, W.P.M., Chem. Engg. Sci., 48 (1993) 3109-3139.

Becher, R.G., Canning, R.G., Goodheart, B.A. and Uusna, S., Proc. Aust. Inst. Min., 21 (1965); Metal. 21-44.

Bhattacharya, I.N. and Chaudhary, G.R., Scand. J. Metallurgy, 19 (1990) 265-268.

Blesa, M.A. and Matijevic, E., Advances in Colloid and Interface Scinece, 29 (1989) 173-221.

Boon-Long, S., Laguenic, L. and Couderc, J.P., Chem. Eng. Sci. 33 (1978) 813.

Bracanin, B.F., Clements, R.J. and Davey, J.M., Proc. Aust. Inst. Min. Metall., 275 (1980) 33-42.

Briens, C-L., Del Pozo, M. and Chiu, K., Chem. Engg. Soc., 48 (1993) No.5, 973-979.

Calderbank, P.H. and Jones, S.J.R., Trans. Inst. Chem. Eng., 39 (1961) 363.

Chapman, C.M., Nienow, A.W., Cooke, M. and Middlestone, J.C., Chem. Engg. Res. Des., (1983) 61- 71.

Charpentier, T.C., Advances in Chem. Engg., 11 (1981) 1-33.

Ciminelli and Osseo-Asare, K., Met. Materials Trans. B, 26B (1995) 209-218.

Ciminelli and Osseo-Asare, K., Met. Materials Trans. B, 26B (1995) 677-685.

Dixon, D.G. and Hendrix, J.L., Metall.Trans. B, 24 (1993) 157-169.

Doraiswamy, L.K. and Sharma, M.M. (Eds.) Heterogenous Reactions, Vol.2, New York (1984).

Dreisinger, D.B. and Peterns, E., Hydrometallurgy, 22 (1989) 101-119.

153

Dutrizac, J.E. and Monhemius, A.J.(Eds), Iron Control in Hydrometallurgy, Ellis Horwood, Chichester, U.K. (1986).

Epstein, N., In: Melo, F., Bott, T.R. and Bernado, C.A. (Eds), Fouling Science and Technology, London (1988) 143.

Farrow, J.B., Ritchie, I.M. and Mangano, P.P., Hydrometallurgy, 18 (1987) 21.

Fisher, Watter, W., Hydrometallurgy, 11 (1988) 55-67.

Finch, J.A. and Dobby, G.S. (Eds), Column Floatation, Oxford (1990) 39.

Felice, R.D.I. and Foscolo, P.U.,Chem. Engg. Sci., 46 (1991) 1873-1877.

Foggler, H. S. (Ed), Elements of Chemical Reaction Engg., Prentice-Hall, Englewood Clifts, New Jersey (1986) 596-610.

Fortuin, J.M.H. and Klijin, P.J., Chem. Eng. Sci., 37 (1982) 611.

Geetha, K.S. and Surender, G.D., Hydrometallurgy, 36 (1994) 231-246.

Gibilaro, L.G. and Rapagna, S., Chem. Eng. Sci., 46 (1991) 1873-1877.

Harvey, H. A., A.I.Ch.E. Journal, 42 (1996) 1491-1494.

Iwai M. and Hiroshi Majima, Denki Kakaku, 47 (1979) 717-722.

Iwai M., Hiroshi Majima and Toshio Izaki, Denki Kakaku, 41 (1979) 409-414.

Iwai, M., Hiroshi Majima and Yasuhiro Awakura, Met. Trans.B, 13B (1982) 311-318.

154

Javancicevic, G. and Bockris, J.O.M., J.Electrochem. Soc. Electrochem. Sci. Technol., 133, No.9 (1986) 1797-1806.

Jayasekera, S., Avraamides, J.,S.I. Bailey and Shaw, L. 6th AUSIMM Extractive Metall. Conf. (1994) 123-126.

Jayasekera, Marinovich, Y., Avraamides and Bailey, S.I., Hydrometallurgy (1995) 183-199.

Joosten, G.E.H., Schilder, J.G.M. and Janseen,J.J., Chem. Engg. Sci., 32 (1977) 563-566.

Joshi, J.B., Utgikar, V.P., Sharma, M.M. and Jurekar, V.A., Reviews in Chem. Engg., 3 (1985) 281-405.

Kamlesh B. Kushalkar and Pangarkar, V.G., Ind. Eng. Chem. Res., 33 (1994) 1817-1820.

Kargi, F. and Moo-Young, M., In: Moo Young, M., Cooney, C.L. and Humphrey A.E. (Eds.), Comprehensive Biotechnology, Vol.2, New York (1985) 6-54.

Kojima H. Uchida, Y., Oshawa, T. and Iguchi, A., J.Chem. Engg. Japan, 20 (1987) 104.

Lee, E.C., Lawsen, F. and K.N. Han, Hydrometallurgy, 3 (1978) 7-21.

Lee, J.C., Ali, S.S. and P. Tasakorn, Fourth European Conference on Mixing,The Netherlands, April 27-29 (1982) 399-415.

Leighton D. and Acrivos, A., J. Fluid Mech., 181 (1987) 415-439.

Lin, H.K. and sohn, H.Y., Proc. Met. Soc. Annual Meeting, new Orleans, Louisiana (1986) 169-186.

Linek, V., Vacek, V. and Beens, P., Chem. Eng. J., 34 (1987) 11-34.

Mackay, R.A. and Jexter (Eds), Colloids and Dispersions, VCH Publishers, Inc., New York (1992) 179-194.

Melo, L.F. and Pinheiro, J.D., Can. J. Chem. Eng., 66 (1988) 36.

Muller-Steinhogen, H., Reif, F., Epstein, N. and Watkinson, A.P., Can. J. Chem. Eng., 66 (1988) 42.

Nagata, S. (Ed.), Mixing Kodansha, Tokyo (1975) 252-253.

Nienow, A.W. and Wisdom, D.J., Chem. Engg. Sci., 29 (1974) 1994.

Oguz, H., Brehm, A. and Deckwer, W.D., Chem. Engg. Sci., 42 (1987) 1815-1822.

Old Shue, J.Y.(Ed.), Fluid Mixing Technology (1983) New York.

Orth, R.J. and Liddel, K.C., Proc. Met. Soc. Annual Meeting, New Orleans, Louisiana March (1986) 23-47.

Pangarkar, V.G. and Jadhav, S.V., Ind. Eng. Chem. Res., 30 (1991) 2496-2503.

Papangelakis, V.G. and Demopoulos,G.P., Metal. Trans. B, 23 (1992) 847-877.

Papangelakis, V.G., Berk, D. and Demopoulos, G.P., Proc. Met. Soc., New Orleans, Louisiana, March (1986) 209-225.

Papavergos, P.G. and Hedley, A.B., Chem. Eng. Res. Des., 62 (1984) 275.

Perry, R.H. (Ed), Chemical Engineers' Handbook, McGraw-Hill (1984).

Ping han and Bartels, J. Phys. Chem., 100 (1996) 5597-5602.

Power, G.P. and Ritchie, I.M., Electrochimica Acta, 26 (1981) 1073-1078.

Pritzker D. M. Metallurgical and Materials Trans. B, 26B (1995) 901-910.

Pritzker D. M., Chem. Engg. Sci., 51 (1996) 3631-3645.

Pyrare lal, Satendra Kumar, Siddh N. Upadyay and Yogendra D. Upadya, Ind. Eng. Chem. Res., 27 (1988) 1246-1259.

Rampall, l. and Leighton, D.T., Int. J. Multiphase Flow, 20 (1994) 631.

Rehm, H.J. and Reed, G.(Eds.), Biotechnology 2, Weinheim (1985) 160-170.

Retait, P.H. and Genin, J.M.R., Corrosion Science, 31 (1993) 797-819.

Ruchi, G., Dunn, I.J., Bourne, J.R. and Von Stokar, U.V., Chem. Eng. J. 30 (1985) 29.

Sada, E., Kumazava, H. and Cho, H.M., Can. J.Chem. Engg., 68 (1990) 622-626.

Sami Selim, M., Al-Naafa, M.A. and Jones, M.C., A.l.Ch.E., 39 (1993) 3.

Sano, Y., Yamoguchi, N.and Adachi, T., J.Chem. Engg. Japan, 7 (1974) 255-261.

Schlutter, V. and Deckver, W.D., Chem.Engg. Sci., 47 (1992) 2357-2362.

Schulze, H.J., Int. Conf.Colloid and Surface Science (July, 1994) 1-22.

Shah, Y.T., Gas-Liquid-Solid reactor design, McGraw-Hill, New York (1979).

Shreir, L.L., Jarman, R.A. and Burstein, G.T. (Eds.), Corrosion, Britain (1994).

Speller, F. N. (Ed), Corrosion, New York and London (1950) 206.

Turner W. Carl, Chem. Engg. Sci., 48 (1993) No.12, 2199-2193.

Toulokian, Y.S.and Buyco, E.H., Thermophysical properties of matter, The TPRC Data Series, Vol.5, IFI/Plenum, New York (1970) 1455.

Vogel (Ed), Text book of quantitative inorganic analysis, London (1989).

Vuillemin, C.J., Bellefon, C.de and Delmas, H., Chem. Eng. Sci., 51 (1996) 2149-2158.

Ward, C.B., Muir, D.M. and Ritchie, I.M., Extraction Metallurgy'89 Conference, London (1989) 1019-1040.

West, J.M. (Ed.), Electrodepositon and Corrosion processes, London (1965).

Yehya, A., Tavvil, E.I., Metal Kunde, 79 (1988) 544-546.

Yagi Hideharu, Toshitumi Motouchi and Haruo Hikita, Ind. Eng. Chem. Process, Des.Dev., 23 (1984) 145-150.

Yagi Hideharu and Fumitake Yoshida, Ind.Eng. Chem. Process Des Dev., 14 (1975) 488-493.

Youngku and Chi-Hua, Chem. Ind. Eng.Che. Res., 31 (1992) 1111-1115.

Zwietering, Th.N., Chem. Eng. Sci., 8 (1958) 244-253.